Title

Charge And Joule Heat Transport In Carbonaceous Materials And Activation Of Biochar

Permalink

https://escholarship.org/uc/item/3xk5z82d

Author

Munoz Hernandez, Andres

Publication Date

2018

Peer reviewed|Thesis/dissertation

UNIVERSITY OF CALIFORNIA, MERCED

CHARGE AND JOULE HEAT TRANSPORT IN CARBONACEOUS MATERIALS AND ACTIVATION OF BIOCHAR

A Dissertation submitted in partial satisfaction of the requirements
for the degree Doctor of Philosophy

in

Mechanical Engineering

by

Andres Munoz Hernandez

Committee in charge:

    Professor Gerardo Diaz, Advisor
    Professor Venkattraman Ayyaswamy
    Professor Williams R. Calderón Muñoz
    Professor YangQuan Chen

The Dissertation of Andres Munoz Hernandez is approved, and is acceptable in quality and form for publication on microfilm and electronically:

_____

Professor Gerardo Diaz, Advisor   Date

_____

Professor Venkattraman Ayyaswamy   Date

_____

Professor Williams R. Calderón Muñoz   Date

_____

Professor YangQuan Chen   Date

University of California, Merced

©2018 Andres Munoz Hernandez

To my soulmate, *mi media naranja,* my wife Eva, and to my lovely and beautiful daughter Gabriela.

To my parents, family, and friends.

To the dreamers,

To the believers,

To the doers,

To the outliers.

ACKNOWLEDGEMENTS

"While we spend much of our time looking for trends, sometimes outliers are much more significant." - unknown.

"Giving up is not an option." - unknown.

¡Querer es poder! ¡Y si se pudo!

God: I would first like to thank God for this life, for my parents, for my wife & daughter, for my family, and for my friends.

My wife: I am very grateful to have met and married my beautiful soulmate, Eva F. Aguayo-Perez, (aka Eva F. Muñoz) during the PhD program. Eva has given me tremendous support by being not only my wife, but my best friend. I am greatly thankful for all her understanding, advice, motivation, support, and for believing in me.

My parents: I would really like to thank my parents Efren Muñoz-Romo and Virginia Hernández-Murillo for being such caring and loving parents, for giving me the opportunity to pursue a higher education, for believing in me, and for all their support. Thanks to my dad for having brought my mom, my siblings, and me to this country in pursuit of the American Dream. I am indebted with my parents for all their financial and moral support. I am further indebted with my mom for all her great cooking and for always worrying about my well-being.

My siblings and family: I am very thankful to my siblings and their families: Monica, Maricela, Jaime, Jesus, Vicente, and Rafael, and to all my extended family for their support and encouragement.

My Advisor Prof. Gerardo Diaz: I want to express my gratitude to my advisor for giving me the opportunity to pursue the doctoral degree, for his guidance, and especially for going the extra mile to secure funding for his students and research projects. Thank you!

Committee members: Profs: Venkattraman Ayyaswamy, Williams R. Calderón-Muñoz, and YangQuan Chen. Thank you for all your help and support.

Collaborators: Very thankful to Sina D. and Prof. Y. Chen for collaboration work on the biochar activation project, and to Prof. W. R. Calderón-Muñoz for collaboration on the simulation projects. Also, very thankful to Prof. Edbertho Leal-Quiros for his help, support, advice, and encouragement during the PhD program.

Undergraduate interns: Andrew J. De Los Santos, Jose Rubalcaba Cruz, Genesis Higueros, Alexis Avila, Adam Martin, Alejandro Perez Tovar, and Azucena Robles. Thank you for all your help.

Professionals at different institutions: I really want to thank and am indebted with the following individuals who really encouraged and supported me while at their

CURRICULUM VITÆ

Andres Munoz Hernandez
December 2018

EDUCATION

Ph.D. Mechanical Engineering, University of California, Merced, December 2018. **Dissertation:** "Charge and Joule heat transport in carbonaceous materials and activation of biochar."

M.S. Mechanical Engineering (Thermofluids) "Distinguished," California State University, Northridge, December 2013. **Thesis:** "Dynamics of droplets inside an air flow channel of a PEM fuel cell under different conditions of flow, gravity, and surface wettability."

B.S. Mechanical Engineering, University of California, Santa Barbara, June 2011.

A.A. Engineering (Honors), Evergreen Valley College, May 2008.

ENGINEERING/RESEARCH EXPERIENCE

- Graduate Research Assistant, University of California, Merced, Fall 2013 – Fall 2018

- Teaching Assistant, University of California, Merced, Fall 2014 – Fall 2015

- Graduate Research Assistant, California State University, Northridge, Fall 2011 – Fall 2013

- Mechanical Engineering Senior Capstone Project, UC Santa Barbara, Fall 2010 – Spring 2011

- Undergraduate Research Internship (URI), UC Santa Barbara Materials Department, Spring 2009 – Spring 2011

- URI, Leibniz Institute for New Materials, Saarbrücken, Germany, Summer 2010

PUBLICATIONS

Journal Articles

1. **A. Muñoz-Hernández** and G. Diaz, Modeling of thermal runaway of carbonaceous materials: Graphite, biochar, and wood. *AIP Advances* 8, 095312 (2018).

2. **A. Muñoz-Hernández**, G. Diaz, W. R. Calderón-Muñoz, and E. Leal-Quiros, Thermal-electric modeling of graphite: Analysis of charge carrier densities and Joule heating of intrinsic graphite rods. *Journal of Applied Physics* 122, 245107 (2017).

3. G. Diaz, N. Sharma, E. Leal-Quiros, and **A. Muñoz-Hernández**, Enhanced hydrogen production using steam plasma processing of biomass: Experimental apparatus and procedure. *International Journal of Hydrogen Energy* 40, 2091 (2015).

4. P. Born, **A. Muñoz**, C. Cavelius, and T. Kraus, Crystallization mechanisms in convective particle assembly. *Langmuir* 28, 8300 (2012).

5. P. Born, S. Blum, **A. Muñoz**, and T. Kraus*, Role of the meniscus shape in large-area convective particle assembly. *Langmuir* 27, 8621 (2011).

Conference Proceedings

1. **A. Muñoz-Hernández**, S. Dehghan, and G. Diaz, Physical (steam) activation of post-gasification biochar derived from peach pits. *Proc. of ASME Int. Mech. Engr. Congress and Exposition, 9-15 November 2018, Pittsburgh, PA, USA.*

2. **A. Muñoz-Hernández** and G. Diaz, Heat transfer analysis of graphite rods subject to Joule heating using a modified semiconductor formulation. *Proc. of 2nd Thermal and Fluid Engr. Conf, and 4th Int. Workshop on Heat Transfer, 2-5 April 2017, Las Vegas, NV, USA.*

3. N. Sharma, **A. Muñoz-Hernández**, G. Diaz, and E. Leal-Quiros, Contact glow discharge electrolysis in the presence of organic waste. *Journal of Physics: Conference Series Vol. 591, p. 012056 (IOP Publishing, 2015).*

4. **A. Muñoz-Hernández** and G. Diaz, Dielectric breakdown process for biomass gasification. *Proc. of ASME Int. Mech. Engr. Congress and Exposition, 14-20 November 2014, Montreal, Canada.*

5. **A. Muñoz-Hernández**, N. Sharma, and G. Diaz, Temperature distribution profiles inside biomass under dielectric breakdown conditions. *Proc. of 10th Int. Conf. on Heat Transfer, Fluid Mechanics, and Thermodynamics, 14-16 July 2014, Orlando, FL, USA.*

6. **A. Muñoz** and A. Mukherjee, Effect of gravity on droplet growth and detachment inside a simulated PEM fuel cell air flow channel with hydrophobic walls. *Proc. of ASME 7th Int. Conf. on Energy Sustainability, and 11th Fuel Cell Science, Engr. and Technol. Conf., 14-19 July 2013, Minneapolis, MN, USA.*

Invited Talk

1. **A. Muñoz-Hernández** and G. Diaz, Physical and plasma activated carbon, *Biosolids & Renewable Energy Innovation Technology Seminar,* 15 November 2017, University of California, Irvine, CA, USA.

Posters

1. **A. Muñoz-Hernández**, S. Dehghan, V. Plotnikov, G. Diaz, and Y. Chen, Exploring plasma activation of biochar for enhanced properties, *Biochar Conf.*, 22-25 August 2016, Corvallis, OR, USA.

2. **A. Muñoz** and A. Mukherjee, *ASME 10th Fuel Cell Science, Engr. and Technol. Conf.,* 23-26 July 2012, San Diego, CA, USA.

HONORS AND AWARDS

- Graduate Research Assistantship, UC Merced, Fall 2013 – Summer 2014, Spring 2016 – Fall 2018

- UC Merced Mechanical Engineering Summer Bobcat Fellowship, 2014 – 2018

- Hispanic Scholarship Fund Scholarship, Sponsored by Wells Fargo & Company, 2017

- UC Merced Mechanical Engineering Bobcat Travel Fellowship, Spring 2014, 2017

- HENAAC Scholarship, Sponsored by Edison International, 2016

- UC Merced Outstanding Graduate Student Award Finalist, April 2016

- Teaching Assistantship, UC Merced, Fall 2014 – Fall 2015

- Fellow of the "NSF CSU-LSAMP Bridge to the Doctorate at California State University Northridge" Fall 2011 – Spring 2013

- Motivational Award, Society of Hispanic Professional Engineers CSUN Chapter, May 2013

- Deans Honors List, UC Santa Barbara, Winter quarter 2011

- Math Engineering Science Achievement (MESA) Scholarship, Sponsored by Chevron, May 2010

- Evergreen Valley College Honors Program, Fall 2004 – Spring 2008

- Evergreen Valley College Commencement Speaker, May 2008

- NASA Scholarship, May 2008

ACTIVITIES AND AFFILIATIONS

- Society of Hispanic Professional Engineers (SHPE)

- Society for Advancement of Chicanos/Hispanics and Native Americans in Science (SACNAS)

- American Society of Thermal Fluids Engineers

- American Society of Mechanical Engineers

- GRAD-EXCEL Peer Mentor Program - Mentor, UC Merced, Fall 2017 – Spring 2018, Fall 2018

- SHPE Graduate Student Representative, Region 1, Fall 2016 – Summer 2017

- UC Merced Leadership Conference, September 2015

- President of EVC SACNAS Chapter, Fall 2007 – Spring 2008

ABSTRACT

CHARGE AND JOULE HEAT TRANSPORT IN CARBONACEOUS MATERIALS AND ACTIVATION OF BIOCHAR

Andres Munoz Hernandez

Doctor of Philosophy

in

Mechanical Engineering

University of California, Merced

2018

Professor Gerardo Diaz, Advisor

The combination of recent drought conditions, closing of biomass processing plants, increased open-burning permit costs, and current practices of agriculture and forest management have created an abundant amount of biomass that is causing increased green house gas (GHG) emissions and potential for catastrophic wild fires. This has motivated the search for innovative solutions for the usage of biomass and its byproducts.

Activated carbons are highly valuable products with endless applications in the food and pharmaceutical industries, among others. While the conventional (physical) activation process involves exposing biochar to superheated steam, the addition of electric fields is being analyzed as an innovative alternative to the energy-intensive physical activation process. The application of an electric field creates a plasma discharge in the gases and induces Joule heating in the carbonaceous material. The main objective of this dissertation is to investigate the dynamics of charge/Joule heat transport and thermal runaway. The purpose is to induce thermal breakdown (high temperatures) in biomass, biochar, and graphite with low energy input and in short amounts of time. This concept was explored through numerical simulation using an electric-thermal model and two variations of a hydrodynamic model, which were developed as part of this work. Results show that Joule heating indeed produces high temperatures in the order of seconds for wood, and in fractions of a second for biochar and graphite – with low energy input.

A second objective is to produce and assess activated carbons derived from agricultural residues and forest woody biomass. In this work, physical activation of peach pit biochar was explored. BET surface areas up to nearly 600 m^2/g were obtained. Though these values are significant, they are still lower than those of commercial activated carbons (>1000 m^2/g). However, these are promising results, especially, because these materials have the potential to be used in industrial filtering applications, not only in soils, as is mainly the case for raw biochar. Moreover, in addition to providing a new market for biomass utilization, biochar and activated carbon provide a stable method for capturing and sequestering carbon.

TABLE OF CONTENTS

LIST OF FIGURES

LIST OF TABLES

NOMENCLATURE

A	nondimensional coefficient
A_c	cross sectional area (m^2)
B	nondimensional coefficient
Bi	Biot number
c_p	specific heat (J/(kg K))
c_0	twice the graphene layer spacing (m)
$C_{L,v}$	volumetric heat capacity (J/(m^3 K))
C_1	constant
D	diameter (m)
e	elementary charge (1.6022×10^{-19} C)
E	electric field (V/m)
E_0	nominal/average electric field (V/m)
$\mathcal{E}_{bo}$	band overlap energy (eV)
Fo	Fourier number for heat transfer
Fo$_2$	Fourier number for charge transfer
G	generation rate (m^{-3}s^{-1})
G_{net}	net generation rate (m^{-3}s^{-1})
h	heat transfer coefficient (W/(m^2 K))
h_P	Planck constant (6.6262×10^{-34} J s)
J	current density (A/m^2)
J_0	current density evaluated at reference temperature (A/m^2)
k	thermal conductivity (W/(m K))
k_B	Boltzmann constant (1.3807×10^{-23} J/K)
l	half of length L (m)
l_{e-e}	electron mean free path (m)
L	length (m)
L_c	characteristic length (m)
m_r	ratio of electron to hole mass density
$m^\star$	effective carrier mass (kg)
m_0	free electron mass (9.1095×10^{-31} kg)
M_1	nondimensional parameter
M_2	nondimensional parameter
n	number density (m^{-3})
$\tilde{n}_{th}$	thermal density computed with Eq. (3.13) (m^{-3})
N_0	characteristic number density (m^{-3})
q	heat rate (W)

p	perimeter (m)
P	power (W)
R	recombination rate (m^{-3}s^{-1})
Re	Reynolds number
R^2	coefficient of determination
t	time (s)
T	temperature (°C, K)
T_0	characteristic temperature (K)
u	velocity (m/s)
u	characteristic velocity (m/s)
V	electric potential/voltage (V)
V_0	characteristic voltage (V)
x	position parameter (m)

Greek Letters

α	thermal diffusivity (m^2/s)
β	nondimensional parameter
γ	nondimensional parameter
δ	tolerance
ε	emissivity
ϵ_r	relative permittivity/ dielectric constant
ϵ_0	permittivity of free space (8.8542×10^{-12} F/m)
ζ	nondimensional parameter
μ	mobility (m^2/(V s))
ν	nondimensional parameter
ξ	limiting value for maximum difference of holes minus electrons (m^{-3})
ρ	charge density (C/m^3)
ρ_m	mass density (kg/m^3)
σ	electrical conductivity ((Ω m)$^{-1}$)
σ_{SB}	Stefan-Boltzmann constant (5.6704×10^{-8} W/(m^2 K^4))
τ	relaxation time (s)
ψ_0	nondimensional parameter
ψ_1	nondimensional parameter

Superscripts

n	index indicating time step or iteration
$'$	denotes quantity per unit length
$*$	denotes nondimensional parameter

Subscripts

app	applied
ave	average
b	breakdown

bi	built-in
c	carrier
$conv$	convection
$c+r$	convection plus radiation
d	dielectric
$Diff$	diffusion
$Drift$	drift
e	electron
ec	end contact
E	energy
h	hole
Jh	Joule heating
h	hole
k	index indicating grid location
max	maximum value
M	momentum
new	new value
old	old value
rad	radiation
ref	reference value at ambient temperature
sur	surrounding
Tot	total
th	thermal
∞	ambient

Chapter 1

INTRODUCTION

1.1 Breakdown Of Solid Materials

Breakdown is an important mechanism that affects all materials, from gases to liquids to solids. In dielectric solids in particular, when a sufficiently high electric field is applied to the material, it loses its insulating properties temporarily or permanently, and this process is known as breakdown. While the mechanism of breakdown of gases had been studied and understood to some extent in the late 1800s [1], there was little or no information of the breakdown mechanism of liquids and solids.

During the early 1900s, the mechanism of dielectric breakdown was divided into two categories: thermal breakdown or 'non-thermal breakdown,' mainly due to insufficient knowledge of the distinct breakdown mechanisms. A few decades later, between the 1930s and the 1950s, the non-thermal breakdown mechanism received a great deal of interest from the research community, and through intensive data gathering from experimental work and theoretical developments the non-thermal breakdown process was beginning to be understood from a more fundamental standpoint. During those years of intensive research the non-thermal type of breakdown was found to be electronic in nature and became known as 'electrical breakdown.'

In 1934, a theory to explain electrical breakdown in solid dielectrics was proposed by Zener [2]. He proposed that electrical breakdown occurs due to the excitation of electrons from one energy band to the next under the presence of an electric field; and when this field is large enough, it leads to a large flux of electrons which are the cause of breakdown. Subsequently, Whitehead and Nethercot [3] performed some experimental work on solid dielectrics under high voltages to study the development of breakdown following the theory of ionization coefficients from gases, but they found that the ionization potentials do not have the same physical meaning as those of gases. Two years later, Fröhlich [4] published the theory of electrical breakdown in ionic crystals. This theory was based on the mechanism as proposed by Von Hippel et al. [5] that electrical breakdown occurred when free electrons, those that had been excited to the conduction band, gained sufficient energy to ionize the

lattice ions causing an abrupt increase of electrons which then leads to breakdown. Fröhlich found that the field strength increased with temperature up to a characteristic temperature, above which, thermal breakdown is the leading mechanism. Moreover, Fröhlich determined that the field strength also increases with the addition of foreign ions as well as for samples of thicknesses of about 10^{-6} cm. These results had somewhat fair agreement with experimental results.

A key individual who significantly advanced the understanding of electrical breakdown in solid dielectrics through intensive and detailed experimental work was Von Hippel. Von Hippel [6] was the first researcher to point out that Paschen's Law [1] failed to predict the breakdown strength of solids, and differentiated the breakdown mechanism of solid dielectrics from the breakdown mechanism of gases. Through experimental work on alkali halide crystals he determined that under the presence of an electric field, electrons collide with the atoms and transfer some of their energy exciting lattice vibrational states, which in time create a positive charge distribution, distorting the electric field, and leading to weakening and breakdown of the structure. He also determined that in these crystals breakdown occurs in preferential directions, a mechanism which is absent in glasses because of their amorphous structure. Moreover, he also determined that slow electrons transfer all the surplus energy to lattice vibrations and become attached.

In a later paper, Von Hippel [7] studied electronic conduction in insulating crystals under very high electric field strengths. He obtained current-voltage characteristic curves that showed that breakdown was electrical in nature, and thermal breakdown was not present even at such high field strengths as other researches had reported. In addition, he measured very low currents even at breakdown field strengths. Von Hippel also determined that the conduction process is not only due to electrons being excited to the conduction band, but also by electrons being excited to other locally bound states with lower energy than the conduction band. Moreover, he determined that the electric current was composed of the migration of both electrons and holes under the effect of the electric field.

Buehl and Von Hippel [8], in contrast to other authors, showed that the field strength of ionic crystals is temperature-dependent. They measured the field strength of KBr as a function of temperature and found that it was constant for temperatures up to about 200 K, it increased steeply to a maximum just above room temperature, and decreased steeply thereafter. Von Hippel and Maurer [9] carried out more experimental work to further investigate the temperature dependency of electrical breakdown on disordered and ordered structures by using glassy and crystalline materials. They found that the breakdown strength of glass is relatively high at low temperatures, it decreases slowly up to about room temperature, then decreases steeply. In contrast, the breakdown strength of crystals had a lower value than glasses and increased monotonically and steadily with temperature. In the case of Silica, it was shown that the breakdown strength of the glass phase was surpassed by that of the crystalline phase above 30 °C. Moreover, Von Hippel and Maurer determined that at low temperatures electrical breakdown of glasses occurred due

to an abrupt increase in current, while at higher temperatures thermal breakdown occurred due to the continuous increase of the current. In a subsequent paper, Von Hippel and Lee [10] analyzed the electrical breakdown strength of mixed NaCl and AgCl crystals. They determined that the increase of breakdown strength from low temperatures to near room temperature was due to the scattering and capture of electrons, while the decrease of breakdown strength at higher temperatures was due to the release of the electrons. They also found that the addition of AgCl up to a certain concentration increased the breakdown strength of NaCl in the lower temperature range and decreased its strength in the higher temperature range.

Von Hippel [11] gave a recount of the most relevant research work on electrical breakdown that accumulated over the past several years. In that paper he gives an overview of the experimental achievements towards understanding the breakdown mechanisms in solid dielectrics as well as an assessment of the relevant theories. He concluded that existing theories were only adequate to describe a subset of the results, and further improvements were necessary. Shorty after, Fröhlich [12] revisited his existing theory of electrical breakdown [4] and obtained results that had better agreement with experimental data. In a later paper, Von Hippel and Alger [13] performed more experiments to further investigate electrical breakdown of ionic crystals. They used transient voltages, evaporated metal electrodes, and various forms of irradiation to study the influence of field emission and space charges on the breakdown strength. They reported that preferred breakdown paths seemed to be related to the Brillouin zones as a result of electron diffraction or electron collisions with lattice vibrations.

In 1951 in a monograph, Whitehead [14] compiled the developments on electrical breakdown that had accumulated over the past two decades, as well as the pre-existing knowledge of thermal breakdown. In addition, he gave an overview of breakdown caused by discharges, electrochemical deterioration, and breakdown from a practical standpoint. He also summarized that the breakdown strength of most insulators was in the order of 10^6 V/cm.

Another important player in the investigation of dielectric breakdown in solids was O'Dwyer, who, in 1958, wrote a short review discussing the advances in the field [15]. A few years later, based on Fröhlich's theory of electrical breakdown [12], O'Dwyer [16] analyzed the current-voltage characteristics of dielectric films assuming different mechanisms: space charge limited with constant electron mobility, tunnel emission from cathode with no space charge, and Schottky emission from cathode with no space charge. He found that the characteristic current-voltage curves were not Ohmic and that they depended on the dielectric thickness and temperature. A year later, Sze [17] investigated current transport and maximum dielectric strength of silicon nitride films. He determined that the current-voltage characterisics are bulk controlled and behaved differently under the following conditions: (1) at high temperatures and high fields, the current is mainly due to field-enhanced thermal excitation of trapped electrons into the conduction band and is independent of the

substrate material, film thickness, and polarity of the electrodes; (2) at low temperatures and high fields, the current is mainly due to field ionization of trapped electrons into the conduction band; and (3) at low fields and moderate temperatures, the current is due to the hopping of thermally excited electrons from one isolated state (trap) to another. Moreover, he reported field strengths in the order of 10^7 V/cm. In that same year, O'Dwyer [18] proposed a new theory of avalanche breakdown assuming continuation of electronic current given by the cathode by field emission. He estimated the collision ionization rate as well as the electron mobility by fitting the theory to experimental data for NaCl and Al_2O_3. Two years later, O'Dwyer [19] published a short review with particular interest in the theories of thermal breakdown and avalanche breakdown. Around the same time, Klein [20] reviewed the thermal and electrical breakdown mechanisms in electronic thin films. In addition, Klein [21] published a comprehensive review of breakdown in solids, including semiconductors and insulators. In 1973, O'Dwyer [22] wrote a book covering the topics of electrical conduction and breakdown in solid dielectrics, where he summarized the most relevant work to date.

Budenstein [23], based on experimental work, reported that under high field strengths, the steep increase in the conductivity of the dielectric materials is due to the formation of highly conductive channels in the material rather than loss of insulating properties in the bulk as a whole, and began development of a new theory to explain this phenomenon.

The analysis of breakdown of polymer insulators attracted great interest in Japan around the mid 1970s. Hikita et al. [24] analyzed the breakdown strength of thin films of poly(vinylidene-fluoride) using various voltage rising rates above room temperature. They determined the breakdown strength to be in the order of 10^6 V/cm, and that it decreased with temperature and was independent of thickness. Above 50 °C, they determined suitable to apply the theory of impulse breakdown mechanism to explain the results, and fitted the data to obtain the values of the relevant parameters. In a subsequent paper, Hikita et al. [25] solved the heat equation for impulse breakdown numerically, and by using the properties of the same material they showed that the breakdown strength is greatly affected by the ability of the sample to dissipate heat through the electrodes. In other works, Hikita et al. studied the breakdown of plasma polymerized styrene films. In one paper [26], they carried out experiments to determine the field strength of the films. They found that the field strength was nearly constant for the temperature range between -196 and 200 °C, and that it was strongly dependent on the rise rate of the applied field. On a second paper [27], they proposed a model for impulse breakdown coupled with current controlled by Fowler-Nordheim cathode emission, disregarding charge accumulation. They compared the model to their experimental data and obtained satisfactory results, which confirmed a low charge accumulation in the bulk of the material. In a subsequent paper, Hikita et al. [28] performed a numerical analysis of steady-state thermal breakdown of relatively thick poly(ethylene-terephtalate) films. They determined that the degree of distortion of the field in the bulk of the material

depends on the field and temperature dependencies of the conductivity, and that thermal breakdown is indeed a possible mechanism of breakdown. In another study, Hikita et al. [29] analyzed high field conduction and breakdown of polyethylene films at high temperatures. They determined that even at high temperatures, breakdown was electronic in nature. Nagao et al. [30] analyzed the effect of local Joule heating on electrical breakdown of polyethylene films. They pointed out that local hot spots appeared at relatively high electric fields, and that the current flowed around these hot spots. They also reported that the current increased with time and that breakdown occurred at these hot spots. In the mid 1980s, Mizutani and Ieda [31] published a review of the most recent advances in several topics related to electrical conduction and breakdown of polymer insulators: pre-breakdown currents, interfacial phenomena, effects of polymer structures and impurities, and behavior of ions at electrodes.

1.1.1 Thermal breakdown

Thus far, the discussion of dielectric breakdown has been general. In this section, the discussion is focused on the particular mechanism of thermal breakdown. When a sufficiently strong electric field is applied to a dielectric at relatively high temperatures, the leading breakdown mechanism tends to be thermal breakdown. Under a high electric field, the current density rises rapidly creating large amounts of Joule heating. Uncontrolled Joule heating causes thermal instabilities that can lead to thermal breakdown, which occurs when the heat generated inside the device is greater than the heat dissipated to the environment. Breakdown of a device happens when the material reaches its glass or melting temperature, which leads to irreversible changes in the material properties and device failure. The electrical conductivity is a key property that can help enhance or prevent the thermal instabilities leading to thermal breakdown. When the electrical conductivity depends positively on the temperature, an increase in temperature leads to an increase in electrical conductivity, and if not controlled, this process leads to an almost instantaneous breakdown [22, 32]. The mechanisms leading to breakdown of dielectric materials have been investigated ever since the early 1900s [14] and have thus lead to the well known theory of thermal breakdown in solids [14, 21, 22].

In the mid 1970s and 1980s, the study of thermal breakdown of polymer insulators attracted great attention [24–28, 30], and the understading of such mechanism on polymers was greatly advanced [31]. In earlier theories of breakdown it was common to assume no charge accumulation in the bulk, which also meant no time dependency. And as reported by several authors, the assumption yielded satisfactory results when compared with experiments. Nevertheless, a comprehensive set of equations to describe thermal breakdown would need to be composed of Maxwell's equations, coupled with the current continuity and the energy equations, as suggested by Budenstein [23]. Nearly a couple of decades later, Noskov et al. [32] used a model composed of all three coupled equations to analyze thermal instabilities of a thin polymer film with an exponential temperature dependence of the electrical

conductivity. In addition to reporting charge and temperature distributions in the bulk, they found that the temperature began increasing exponentially reaching values of over 1000 °C in just over 50 microseconds. These characteristic times were comparable to the times reported, nearly a decade later, by Neff et al. [33] for their analysis on crystalline polymer insulators using impulse thermal breakdown. Neff et al. also reported the thermal breakdown strength to be in the order of magnitude of 10^6 V/cm, which falls in the range of values reported by other authors. During the same year, Yothi et al. [34] analyzed temperature distributions in a newer type of insulator, i.e., resin impregnated paper, a material that is used in transformer bushings. Under an alternating voltage, they calculated temperature distributions with a maximum value under 380 K, and estimated the thermal breakdown voltage to be 750 kV; a lower value than most other insulators.

Thermal breakdown analyses are performed not only in thin/bulk insulators (or other solids), but also on systems. For instance, Brandao et al. [35] analyzed various characteristics of the thermal stability and runaway in microbolometers. In addition to determining the stability conditions, they also reported that steady-state was achieved in the order of milliseconds under current biased conditions, and within seconds under voltage biased conditions. Steady-state temperatures near 2000 and 4000 °C were reached in two cases when thermal runaway occurred. The magnitude of the bias currents was in the order of μA to mA, and that of the bias voltages under 10 V.

In yet another study, Yune et al. [36] carried out numerical simulations to analyze the behavior of thermal instabilities in graphite brushes. They reported steady-state temperatures in the range of 37 to over 3000 °C for corresponding current densities of 0.32×10^6 to 4.06×10^6 A/m^2, produced with applied voltages of 0.25 to 3.14 V. It is worth noting that solid dielectrics have been used in most of the studies thus far, in contrast, graphite is not a dielectric. In fact, it is a great conductor, and because of its high electrical conductivity, at low applied voltages the current densities obtained are really high. Let us bear this in mind as a major portion of the theoretical/modeling work in this dissertation is based on graphite.

The simultaneous advancement of technology and the development of micro/nanodevices and new micro/nanomaterials, such as graphene and carbon nanotubes, over the past two decades has led to ever increasing power (current) densities that require high heat dissipation rates. For example, carbon nanotubes and graphene nanoribbons have been reported to sutain current densities in the order of 10^9 A/cm^2 and 10^8 A/cm^2, respectively [37, 38]. Pop et al. [37] investigated Joule heating and breakdown of carbon nanotubes numerically and experimentally. They determined a nearly linear dependence of the breakdown voltage with length. They also found that the current tends to saturate at higher voltages due to Joule heating; a similar trend was found by Kuroda et al. [39]. Durkan et al. [38] analyzed breakdown of graphene devices due to Joule heating under current stressing conditions. In addition to measuring the current-voltage characteristics, they estimated resistivity

values for the devices. Graphene transistors have also been subject to studies analyzing Joule heating. Several studies have determined the appearance of hot spots under different biased conditions. It has been determined that hot spots appear at locations with minimum carrier densities, which also correspond to large gradients in electric field [40–42]. Modeling of these devices has also enabled the estimation of carrier densities, temperature, field, and electrical resistance. Other studies have also shown the impact of Joule heating in organic semiconductors [43], where transient simulations using a drift-diffusion model coupled with the heat equation have been used to analyze the dynamic and steady-state behavior of the temperature, current and capacitance.

Thermal breakdown has been and will continue to play a significant role in the design and development of electronic and semiconductor devices, especially as the device size decreases. Simulations will continue to aid in the understanding of charge transport and Joule heat generation/dissipation, which in turn will help reduce the risk of thermal breakdown.

From a different perspective, by having a better understanding of these mechanisms, they can be exploited for a different purpose. For instance, based on the studies mentioned heretofore, thermal breakdown (high temperatures) can be reached in fractions of a second. These mechanisms may be used in applications where high temperatures are desired, such as in gasification systems. This concept is a driving motivation for some of the studies in this dissertation and will be discussed in further detail in future chapters.

1.2   Hydrodynamic Modeling Of Semiconductors

As discussed in the previous section, thermal breakdown affects all solids: from dielectrics to conductors. Over the past few decades the size of semiconductor devices has decreased from the micrometer size to the nanometer size. Charge and Joule heat transport in microscale devices had been analyzed successfully using thermally-coupled drift-diffusion models [44–46]. However, as the devices reached and surpassed the submicrometer scale, hydrodynamic models needed to be employed to capture these dynamics [47–51]. It is the purpose of this section to introduce hydrodynamic modeling of semiconductor devices.

Semiconductor materials have been crucial components in the advancement of technology – computers in particular. As such, semiconductors have been under intensive investigation from theoretical analyses and numerical simulations to experiments [44–46,51–53]. The performance of semiconductor devices, such as field effect transistors (FETs), relies on the effectiveness of these devices to transport charge and (Joule) heat. These phenomena have been analyzed comprehensively through experiments, which have yielded vast amounts of data on semiconductor characteristics and properties [54].

In order to further understand these phenomena beyond experiments, fine tune the devices, and extend the range of applications, numerical simulations are often used. The simplest and probably the most common numerical technique to analyze

semiconductor devices is the well-known drift-diffusion model [45, 46]. However, this model was developed to capture steady-state processes under thermal equilibrium conditions. In addition, it is only applicable to devices for which the characteristic length is much larger than the mean free path of electron-phonon collisions. Yet, with the current advancement of technology, devices have been decreasing in size beyond the submicrometer scale, and faster response times of the devices are desired. Thus, more adequate models which can capture the physical phenomena for submicrometer devices have been under development.

To numerically analyze submicrometer semiconductor devices the Monte Carlo method [52] and hydrodynamic models are generally used [51, 52]. Hydrodynamic models are composed of a set of coupled nonlinear partial differential equations that are similar to those of Navier-Stokes used in Fluid Dynamics, in addition to being coupled to Maxwell's equations [48, 51, 52, 55–57]. The collisionless terms of these equations are derived from the general Boltzmann transport equation (BTE) [56, 58], and assume that electrons/holes behave like a fluid substance. Their applicability to a given device is also limited by a lower characteristic size, in this case it has to be larger than the mean-free-path of electron-electron collisions [57]. While the majority of the terms making up the hydrodynamic model are obtained directly from the moments of the BTE, the collision terms need to be derived independently. Bløtekjær performed this job based on strong theoretical developments [55]. Bløtekjær derived the collision terms using relaxation time approximations which yielded a hydrodynamic model with all explicit terms. His approach has been widely used thereafter [48, 49, 51, 52, 59]. These models, however, are quite complex to solve and are numerically expensive, requiring advanced numerical schemes [50–52, 56, 59–62]. Further details about the derivation of the hydrodynamic model utilized in this dissertation are presented in Chapter 2 and Appendix A.

1.3   Activated Carbon

Preamble. Though there is a change in topics between the previous sections and this section, the link between these works will be discussed next –and in the 'Motivation and Objectives' section below. The idea linking previous topics related to Joule heating/dielectric breakdown and activated carbon is the following. The process of carbon activation – and biomass gasification – is typically carried out at high temperatures. Based on our global and scientific interests, two concepts *motivated* the work in this dissertation: (1) the concept of using Joule heating-induced thermal breakdown of carbonaceous materials to achieve high temperatures in a short amount of time, and (2) the utilization of dielectric breakdown of carbonaceous materials to change their surface properties. While the former concept was analyzed in great extent through modeling work in this dissertation, the latter concept is *not* part of this dissertation. Nonetheless, the latter concept refers to using plasma discharges at atmospheric pressure where carbonaceous materials are part of the circuit, see Fig. 1.1. Moreover, plasma discharges are being explored – in other works in our research group – as a novel technique to activate biochar. However, before

being able to analyze the extent of plasma activation of biochar, a benchmark using conventional activation procedures needed to be developed. As a consequence, the work done in this dissertation focuses on the development of the benchmark carbon (biochar) activation process using the standard physical activation method. The results and comparison of plasma-enhanced carbon activation and physical activation will be published elsewhere.

Activated carbons are highly porous materials that are produced from coals or biomass – coconut shells in particular – using different methods [63–65]. Commercial grade activated carbon, which is commonly produced in kilns under a steam atmosphere, has BET surface areas larger than 1000 m^2/g. In addition to high porosity, activated carbon has various chemical surface characteristics. For example, surface functional groups enhance the chemical reactivity of activated carbons and improve their adsorption capabilities. In laboratory investigations, conventional activation processes usually consist of physical or chemical activation. Physical activation is usually carried out in the neighborhood of 800 °C under the presence of steam or carbon dioxide. To reach these temperatures in laboratory scale units, furnaces that require power in the range of kiloWatts and reach maximum temperatures between 1000 and 1200 °C have been used [66–68]. On the other hand, the chemical activation process is usually performed at temperatures around 400-500 °C. The material is washed with a strong acid or base such as phosphoric acid or potassium hydroxide [66]. The process is usually performed at laboratory scales yielding surface areas larger than physical activation, however, scaling up this method is neither economical nor environmental friendly. A review on the usage of agricultural residues as precursors for activated carbons is given by Ioannidou and Zabaniotou [64].

1.4   Motivation And Objectives
1.4.1   Global motivation
In the past few decades there has been increasing interest on using renewable energy sources and reducing the usage of fossil fuels. There has also been increased interest in finding other non-energy-related applications for these renewable resources. Biomass, for example, has been commonly used in the production of energy by direct combustion and by gasification. In addition, the effect of biochar as an additive for soil enrichment has been undergoing heavy investigations. Moreover, by activating the *post-gasification* biochar, its BET surface area can be increased, and its applications expanded, as in filter media for water treatment or for air pollution control, for example. To date, gasification of biomass at the industrial scale has been achieved, as well as the production of both biochar and biomass-derived activated carbons. Much of the commercially activated carbons, however, are made from coal or coconut shells. While coal-derived activated carbons are produced in the United States, coal is a non-renewable source. On the other hand, coconut shell activated

carbons are typically imported from Asia. The United States exports about $384 million and imports about $192 million worth of activated carbon per year[1].

The Central Valley in California, is a major agricultural hub which produces abundant amounts of byproduct biomass. While some of the agricultural byproduct biomass has several markets, excess biomass tends to be incinerated or ends up in the landfills. In addition to the agricultural byproduct biomass, the drought over the last years brought a disease that killed over 100 million trees in the Sierra Nevada [69]. The State of California is currently looking for viable solutions for the removal and usage of the dead trees in order to prevent the spread of forest fires. The overall goal of this work is to look for viable solutions to these problems. More specifically, our goal is to investigate alternate and efficient methods of biomass gasification and activation of biomass-derived biochar. Our approach will have four expected benefits: (1) added value to excess biomass, (2) expansion to new markets, (3) reduced waste in landfills, and (4) reduced emissions due to open incineration of the excess biomass.

1.4.2 Scientific motivation
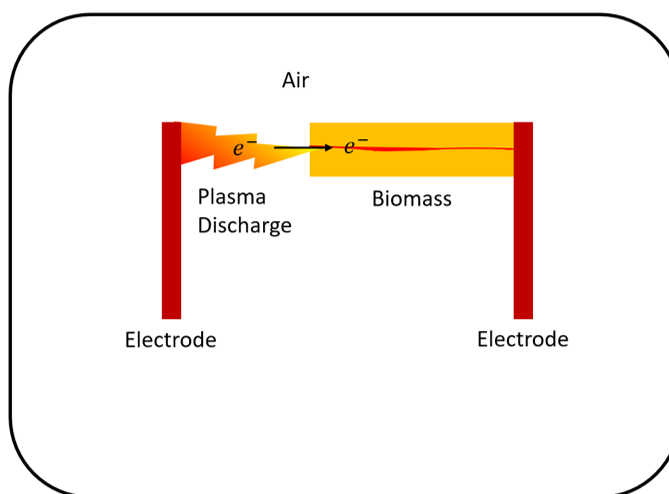
Figure 1.1: Schematic representation of plasma discharge through air and biomass.

The work performed in this dissertation is motivated by the potential applications that would affect the society at large, as discussed in the previous subsection. Nonetheless, there are several scientific questions of interest behind these applications, which are also motivating the work behind this dissertation.

Though in this dissertation two distinct topics are being addressed, namely, (1) modeling of charge and Joule heat transport in carbonaceous materials, and (2) biochar activation, they were both motivated by our initial scientific questions and potential applications. The following research questions were posed (Fig. 1.1 depicts these questions):

- What happens to electrons as they flow from a plasma discharge to a solid? Our particular interest is in a plasma discharge in air at atmospheric pressure, and the solids being wood and biochar.

- How do electrons move through the solid? That is, what are their densities, velocities, and energies? Other relevant dynamics? Thus, the use of the hydrodynamic models and the use of graphite.

- What properties of the solid change temporarily or permanently? For example, electrical conductivity, surface chemistry, porosity of the material – this is related to activated carbon.

- Can thermal breakdown of the air plus the biomass/biochar be used as a gasification/activation technique? Thus, the study of Joule heating and thermal runaway, as well as, carbon activation.

The work in this dissertation was motivated by these questions. However, the work found herein, only answers part of these questions. The remaining work serves as motivation for future research.

1.4.3 Objectives

The main objective of this work is to investigate Joule heating as a potential method to heat biomass up to pyrolysis temperatures. There have been extensive studies on solid dielectrics analyzing how thermal instabilities arise due to Joule heating, which when uncontrolled lead to the thermal breakdown of the materials. While in past studies the main purpose was to prevent breakdown, our purpose is to induce breakdown, and use it as a sustainable method for biomass pyrolysis or gasification. During thermal breakdown, the energy (current) input from the power supply is directly released inside the biomass as Joule heating. Such conditions can make this system more efficient than a conventional plasma assisted gasifier, in which a plasma torch is used to gasify biomass, where a significant fraction of the plasma energy is lost to the environment before it reaches the biomass. Moreover, as opposed to non-plasma gasifiers, where a fraction of the gases produced is used to dry and heat the biomass by combusting it, using thermal breakdown reduces the need for combusting part of the biomass for heat production since part of the heat can be provided by Joule heating.

The second objective is to develop the experimental setup and procedure for physical activation of biochar with superheated steam. Though, as opposed to most lab experiments, most of the raw biochar that is used in our experiments is the byproduct of a commercial gasification power plant – Phoenix Energy™. The purpose of the study is to determine whether post-gasification biochar from agricultural residues and Ponderosa pine, available in the Sierra Nevada, can be successfully activated, i.e., to approximate properties of coconut shell- and coal-based activated carbons. If proven successful, this could open a new market for agricultural residues and Ponderosa pine dead trees. In addition, the activated biochar that is

obtained with physical activation will serve as the benchmark for plasma activated biochar – a novel approach currently being explored by our research group, which will be published elsewhere.

1.5   Dissertation Structure

The structure of the dissertation is presented as follows. Chapter 2 gives a detailed description of the two models used in the dissertation: (I) conventional electric-thermal modeling that has been used mostly in the analysis of thermal break-down of solid dielectric materials, and (II) hydrodynamic models, used mostly in the study of charge and energy transport in conventional semiconductors. Chapter 2 also presents more details of the electrical conductivity of biochar, and the electronic properties of pyrolytic graphite, and the fact that graphite is considered a zero-gap semiconductor or a semimetal. Because graphite is virtually a pure carbon material and single-crystal-capable, it will provide the link between carbonaceous materials – which tend to be non-crystalline – and semiconductor materials – which are virtually single crystal materials. In Chapter 3, the steady-state one-dimensional version of the hydrodynamic model, better known as a drift-diffusion model, is used to investigate the dynamics of carrier transport under the effects of Joule heating. In Chapter 4, a transient one-dimensional version of the hydrodynamic model is developed along with a suitable numerical scheme. In addition, because hydrodynamic models are composed of highly coupled nonlinear partial differential equations, and they have been typically applied to semiconductors only, the stability and range of applicability of this model when using graphite properties is analyzed. The work from this chapter will serve as the basis for future work to actually solve the hydrodynamic model using properties of graphite (and perhaps multilayer graphene). In Chapter 5, the conventional electric-thermal model, which, historically, has been used in the analysis of thermal breakdown assuming no charge accumulation [22], is used to analyze thermal runaway of graphite, biochar, and biomass. In Chapter 6, activation of biochar from agricultural residues from California's Central Valley and Ponderosa pine – a material available at the Sierra Nevada – is explored through physical activation with superheated steam. Physical activation is a mature industrial process. The results will be used as a benchmark to compare to activated biochar samples obtained with a *novel* technique using *plasma* in the form of *dielectric barrier discharge*, along with other types of discharges. Though, the work pertaining to this dissertation is only that of the physical activation. The plasma activation and the comparison of the activated carbons obtained with the two different processes will be presented elsewhere.

Chapter 2

BACKGROUND: MODELING AND CARBONACEOUS MATERIAL PROPERTIES

2.1 Introduction

In this Chapter, a simple conventional electric-thermal model and a hydrodynamic model to analyze the dynamics of charge and heat transport in carbonaceous materials will be introduced. In addition, the strong effect of the treatment temperature on the electrical conductivity of heat-treated biomass will be briefly discussed, and it will be shown that at higher treatment temperatures, the electrical conductivity is about three to four orders of magnitude lower than that of graphites. Moreover, the electronic properties of pyrolytic graphite will be discussed, and graphite's similitude with semiconductor materials will be pointed out.

The main objective of this dissertation is to analyze the dynamics of Joule heating towards achieving high temperatures in carbon materials using two types of modeling techniques: (1) electric-thermal modeling and (2) hydrodynamic modeling. The electric-thermal model can be easily applied to crystalline and non-crystalline materials. On the other hand, because the hydrodynamic model was developed based on single crystals (semiconductor materials), it would be a great challenge, or perhaps not viable, to extend it to analyze non-crystalline materials. Because biomass and biochar are virtually non-crystalline, it is ideal to use another material that is both crystalline and carbonaceous, and that is called *pyrolytic graphite.* Thus, graphite is a carbon material that will help link the two worlds: (low to no crystallinity) carbon materials and (inorganic) single crystal materials, Fig. 2.1 depicts this statement. Moreover, using properties of graphite, the results obtained with the conventional electric-thermal model will be compared to the results obtained with the hydrodynamic model. In summary, the two models complement each other, and the more suitable model can be used when analyzing different problems depending on the information of the thermophysical properties available for each material, and on the parameters of interest to the user.
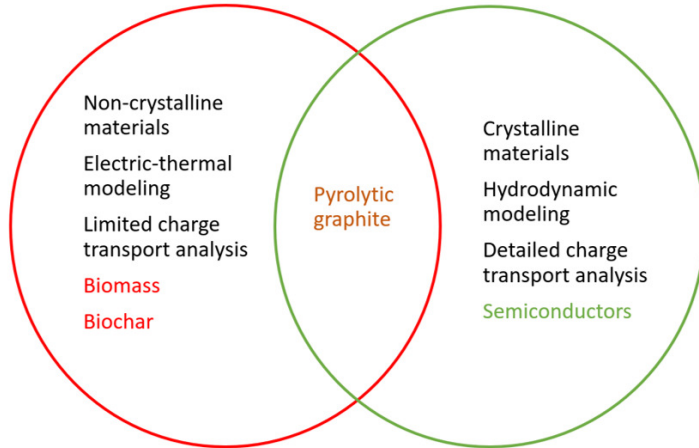
Figure 2.1: Pyrolytic graphite provides the link between non-crystalline carbonaceous materials and single crystal, inorganic semiconductor materials.

2.2 Conventional Electric-Thermal Modeling

As discussed in the introduction, historically, the study of thermal breakdown has been focused primarily in the analysis of solid dielectrics, such as alkali halides (KBr, NaCl, etc.), silicon oxides, in both glass and crystal forms, and polymers. In most of those cases, it was common and fair to assume that no charges accumulated in the bulk of the sample [22]. The set of equations used to analyze thermal breakdown typically consisted of the energy equation coupled with the equation for total current continuity, with the assumption of no charge accumulation ($\partial \rho / \partial t = 0$), where ρ is the electric charge density, as follows:

$$0 = \nabla \cdot (\sigma \nabla V), \tag{2.1a}$$

$$C_{L,v} \frac{\partial T_L}{\partial t} = \nabla \cdot (k_L \nabla T_L) + \sigma |\nabla V|^2, \tag{2.1b}$$

where V is the electrostatic potential, T_L is the lattice temperature, $C_{L,v}$ is the volumetric specific heat, k_L is the thermal conductivity, and t is the time. Integrating Eq. (2.2b), the total current density can be readily obtained $\boldsymbol{J} = \sigma \boldsymbol{E}$, where the electrical conductivity, $\sigma(\boldsymbol{E}, T_L)$, may be dependent on both electric field, $\boldsymbol{E} = -\nabla V$, and lattice temperature, T_L, where the bolded parameters denote vector quantities.

Nonetheless, a more complete set of equations to analyze thermal breakdown, including Gauss' Law (which allows quantification of charge accumulation), can be obtained by using a subset of Maxwell's equations coupled with the energy equation for the lattice. Such a model is described by the following equations which consists of Gauss' Law, Eq. (2.2a), current continuity, Eq. (2.2b), and the energy equation

14

for the lattice, Eq. (2.2c), after Noskov et al. [32]:

$$\nabla^2 V = -\frac{\rho}{\epsilon_r \epsilon_0}, \tag{2.2a}$$

$$\frac{\partial \rho}{\partial t} = \nabla \cdot (\sigma \nabla V), \tag{2.2b}$$

$$C_{L,v}\frac{\partial T_L}{\partial t} = \nabla \cdot (k_L \nabla T_L) + \sigma |\nabla V|^2 - q_{c+r}, \tag{2.2c}$$

where ϵ_r is the relative permittivity, ϵ_0 is the permittivity of free space, $C_{L,v}$ is the volumetric heat capacity, k_L is the thermal conductivity, t is the time, and T_∞ is the ambient temperature. Although in the research of dielectric materials thin films of the order of μm have been used, we are interested in analyzing problems with length scales in the order of mm to cm. Thus, heat losses by convection and radiation may become more important. Therefore, the term representing such heat losses, q_{c+r}, has been added to the energy equation, (2.2c). In certain cases, especially in microelectronics, the material or device in question is placed on top of a solid substrate, therefore, heat losses by conduction should be included in the overall heat losses term.

These equations are very useful because they are relatively simple, and they can be solved using inexpensive, conventional numerical techniques. In addition, the application of these equations can be extended to non-crystalline materials due to the fact that they are based on macroscale thermophysical properties, i.e., σ, k_L, and $C_{L,v}$. These properties can be measured experimenally for all materials regardless of their structure. In the case of single crystals, these properties can also be deduced from their more fundamental definitions, e.g., $\sigma = e(\mu_e n_e + \mu_h n_h)$, where e is the elementary charge, μ_e (μ_h) is the electron (hole) mobility, and n_e (n_h) is the electron (hole) density.

The applicability of this model, which is sometimes referred to as a type of drift-diffusion model, in solid crystalline materials will be limited to devices with length scales that are larger than the mean free path of electron-phonon collisions [57]. In addition, to electron-electron and electron-phonon collisions in single crystals, in poly-crystalline and amorphous materials, the mean free path of the electrons will be affected by the presence of foreign atoms, and defects due to domain boundaries, vacancies, etc; the extent of the effect will depend on their concentration. It is important to note that this model assumes thermal equilibrium between the lattice and charge carriers. Moreover, it only allows the calculation of a limited number of variables, i.e., total current density, charge density (and possibly the charge carrier densities), voltage, and lattice temperature. To obtain information related to the charge carriers, such as velocities, and temperatures, a hydrodynamic model or a simplified version of it must be used.

In this work, variations of this model will be used to analyze charge and heat transport in biomass, biochar, and graphite.

2.3 Hydrodynamic Modeling

The conservation equations for hydrodynamic models are analogous to those of Navier-Stokes used in fluid dynamics [48, 51, 52, 55–57]. Hydrodynamic models are used to analyze charge and energy transport in semiconductor devices [46, 52, 55, 59, 61, 70], as well as, in plasma discharges [71–73]. Their applicability to such problems in semiconductor devices is justified when the characteristic size of the device is greater than the average mean free path of electron-electron and electron-phonon interactions [57]. The collisionless terms of the conservation equations for the hydrodynamic models are derived by taking the first three momments of the general Boltzmann transport equation (BTE) [56, 58, 74].

The general BTE is written as follows [74, 75]:

$$\frac{\partial f}{\partial t} + \boldsymbol{v} \cdot \nabla_{\boldsymbol{v}} f + \frac{\boldsymbol{F}}{m} \cdot \nabla_{\boldsymbol{r}} f = \left(\frac{\partial f}{\partial t}\right)_c \tag{2.3}$$

where $f(\boldsymbol{r}, \boldsymbol{v}, t)$ is the distribution function of particles in six-dimensional space, or *phase space*, t is the time, $\boldsymbol{v}$ is the particle velocity, $\boldsymbol{F}$ represents external forces, m is the particle mass, and $\boldsymbol{r}$ is the spacial coordinate. The term on the right-hand-side represents the particle collisions, which is usually approximated using relaxation times [48, 55, 76].

The equations for the hydrodynamic model to analyze charge and heat transport in semiconductor devices can include one [49,52,55,57,74] or more [47,50,56,58, 60,77,78] charge carriers and their momentum and energy. Often times the velocity and temperature values are more useful than the momentum and energy quantities, and are therefore utilized. Moreover, some models contain conservation equations for specific phonon (acoustic, optical, etc.) energies while others contain an energy equation for the lattice only. The choice of the equations depends on the application, available material and system properties, and the desired outcome.

It is our interest to use the hydrodynamic model to analyze charge and heat transport in a graphite device. Because intrinsic (not doped) graphite containes two-charge carriers, i.e., electrons and holes [79, 80], our analyses will be based on a two-charge carrier hydrodynamic model. This model includes the carrier velocities and temperatures, as well as, the lattice temperature.

The following general set of equations may be referred to as a *three-temperature, two-carrier* hydrodynamic model because it has three different energy (temperature) equations and contains two charge carriers. This model is similar to other models found in the literature [48,50,59]. The model is composed of Gauss's law in Eq. (2.4a), charge conservation equations for electrons and holes in Eqs. (2.4b) and (2.4c), momentum conservation equations for electrons and holes in Eqs. (2.4d) and (2.4e), the changes of kinetic energy of electrons and holes due to their interactions with the lattice in Eqs. (2.4f) and (2.4g), and the lattice thermal energy in Eq. (2.4h). The set of equations is

$$\nabla^2 V = -\frac{e}{\epsilon_r \epsilon_0} \left(n_h - n_e \right), \tag{2.4a}$$

$$\frac{\partial n_e}{\partial t} + \nabla \cdot (\boldsymbol{u_e} n_e) = G_e - R_e, \tag{2.4b}$$

$$\frac{\partial n_h}{\partial t} + \nabla \cdot (\boldsymbol{u_h} n_h) = G_h - R_h, \tag{2.4c}$$

$$\frac{\partial \boldsymbol{u_e}}{\partial t} + \boldsymbol{u_e} \cdot \nabla \boldsymbol{u_e} = \frac{e}{m_e^\star} \nabla V - \frac{k_B}{m_e^\star n_e} \nabla (n_e T_e) - \frac{\boldsymbol{u_e}}{\tau_{M,e}}, \tag{2.4d}$$

$$\frac{\partial \boldsymbol{u_h}}{\partial t} + \boldsymbol{u_h} \cdot \nabla \boldsymbol{u_h} = -\frac{e}{m_h^\star} \nabla V - \frac{k_B}{m_h^\star n_h} \nabla (n_h T_h) - \frac{\boldsymbol{u_h}}{\tau_{M,h}}, \tag{2.4e}$$

$$\frac{\partial T_e}{\partial t} + \boldsymbol{u_e} \cdot \nabla T_e = -\frac{2}{3} T_e \nabla \cdot \boldsymbol{u_e} + \frac{2}{3 n_e k_B} \nabla \cdot (k_e \nabla T_e) - \frac{T_e - T_L}{\tau_{E,e}}$$
$$+ \frac{2 m_e^\star |\boldsymbol{u_e}|^2}{3 k_B \tau_{M,e}} \left(1 - \frac{\tau_{M,e}}{2 \tau_{E,e}} \right), \tag{2.4f}$$

$$\frac{\partial T_h}{\partial t} + \boldsymbol{u_h} \cdot \nabla T_h = -\frac{2}{3} T_h \nabla \cdot \boldsymbol{u_h} + \frac{2}{3 n_h k_B} \nabla \cdot (k_h \nabla T_h) - \frac{T_h - T_L}{\tau_{E,h}}$$
$$+ \frac{2 m_h^\star |\boldsymbol{u_h}|^2}{3 k_B \tau_{M,h}} \left(1 - \frac{\tau_{M,h}}{2 \tau_{E,h}} \right), \tag{2.4g}$$

$$C_{L,v} \frac{\partial T_L}{\partial t} = \nabla \cdot (k_L \nabla T_L) + \frac{3 n_e k_B}{2} \left(\frac{T_e - T_L}{\tau_{E,e}} \right)$$
$$+ \frac{3 n_h k_B}{2} \left(\frac{T_h - T_L}{\tau_{E,h}} \right) + q_l''', \tag{2.4h}$$

where V is the electrostatic potential, n_e is the electron density, n_h is the hole density, $\boldsymbol{u_e}$ is the electron velocity, $\boldsymbol{u_h}$ is the hole velocity, T_L is the lattice temperature, T_e is the electron temperature, T_h is the hole temperature, G_e is the generation rate of electrons, G_h it the generation rate of holes, R_e is the recombination rate of electrons, R_h it the recombination rate of holes, q_l''' represents the heat losses, which may include radiation, convection, and/or conduction, and t is the time.

The physical parameters are the elementary charge, e, the permittivity of free space, ϵ_0, the relative permittivity of the material, ϵ_r, the effective electron mass, $m_e^\star$, the effective hole mass, $m_h^\star$, Boltzmann's constant, k_B, the momentum relaxation time for electrons, $\tau_{M,e}$, the momentum relaxation time for holes, $\tau_{M,h}$, the energy relaxation time for electrons, $\tau_{E,e}$, the energy relaxation time for holes, $\tau_{E,h}$, the thermal conductivity of electrons, k_e, the thermal conductivity of holes, k_h, the thermal conductivity of the lattice, k_L, and the volumetric heat capacity of the lattice $C_{L,v}$.

In this work, simplified versions of this hydrodynamic model are used to analyze charge and heat transport in graphite rods in Chapters 3 and 4. The simplified versions of the hydrodynamic model were obtained based on specific criteria; the detailed step-by-step process is given in Appendix A.

2.4 Electrical Conductivity Of Heat-Treated Biomass And Biomass-Based Products

Biomass materials are insulators by nature. Their conductivity is affected by many factors, but specially moisture content and temperature [81–84]. For instance, the electrical conductivity of raw dry wood is in the order of 10^{-14} to 10^{-16} (Ω m)$^{-1}$, while that of saturated wood is in the order of 10^{-3} to 10^{-4} (Ω m)$^{-1}$ [83], a tremendous increase in conductivity!

In addition to moisture, heat-treating the biomass to (carbonization) temperatures, approximately above 500 to 600 °C, significantly increases the electrical conductivity of the material. However, this increase comes at the expense of mass losses, mostly due to the volatile matter, and in the process, the biomass becomes charcoal, also known as *biochar*. The effect of the carbonization temperature on the electrical conductivity of various wood and wood-based materials has been analyzed by several authors [85–87]. Their results show that the electrical conductivity increases by several orders of magnitude with carbonization temperature, as shown in Fig. 2.2 [86]. For example, the conductivity of solid wood carbonized at 600 °C was nearly 10^{-3} (Ω m)$^{-1}$, while the conductivity increased to about 10^2 (Ω m)$^{-1}$ after carbonization at 1100 °C. This is an increase of about five orders of magnitude. In comparison, the conductivity for pyrolytic graphite is about 10^6 (Ω m)$^{-1}$ while that of POCO® graphites [88] is in the order of 10^5 (Ω m)$^{-1}$. Thus, at a carbonization temperature of 600 °C the conductivity of heat-treated wood (biochar) is already more than 11 orders of magnitude larger than raw dry wood! Moreover, the electrical conductivity of carbon-based materials tends to increase even more with higher carbonization temperatures. This trend is seen in graphite, whose electrical conductivity tends to increase with (graphitization) temperature due to the development of larger single crystal domains [79, 80, 88].

2.5 Pyrolytic Graphite

Graphite and graphite-derived materials, such as graphene, play a key role in many engineering applications. The electronic properties of graphite have been studied experimentally and theoretically to a great extent. For example, Wallace [89] applied the band theory of solids to analyze the physical properties of graphite, including its electrical and thermal conductivities. He also noted the high anisotropy of electrical conductivity along the parallel and perpendicular directions to the layer planes. In addition, Wallace found graphite to have a zero gap between the conduction and valence bands. As a consequence, graphite is sometimes referred to as a zero-gap semiconductor.

Kinchin [90] performed pioneering work in analyzing the electronic properties of polycrystalline and single crystal graphite at high temperatures. He found the number of free electrons to be about 6×10^{24} m^{-3} at room temperature. He also estimated the ratio of the mobilities of holes to electrons to be about 0.80. In addition, Kinchin calculated the resistivity, the thermal mean free path and the product of the effective mass times the velocity of free electrons as a function of
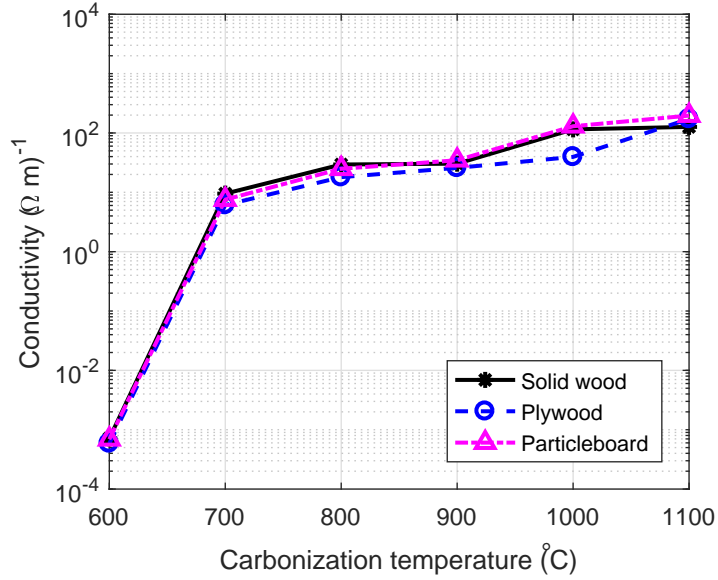
Figure 2.2: Conductivity of biochars at different carbonization temperatures [86].

temperature. Kinchin's findings served a key role in later investigations, and his findings were found to agree fairly well with later results of other researchers.

McClure [91,92] performed more work related to the band structure of graphite, where he estimated the band overlap of graphite to be about 0.03 eV [91]. In later investigations, McClure [93] and Soule [94, 95] performed additional studies which included quantification of the electron/hole densities, carrier mobilities, and carrier effective masses at low and room temperatures. McClure [93] found the electron/hole densities to be about 7×10^{24} m^{-3}, and the mobility to be about 1 V/(m^2 s) at room temperature. Soule [94] further determined that the magnitude of the electron/hole density varied from 5×10^{24} to 2×10^{24} m^{-3}, and the ratio of the electron/hole mobility to vary from 1.1-0.79, for temperatures in the range between 298 K and 4.2 K. In addition, Soule [94, 95] calculated the effective masses for electrons and holes to be about $0.03m_e$ and $0.06m_e$, respectively, along the layer planes at a temperature of 4.2 K.

Further work on the electronic properties of graphite was carried out by Klein [79, 80]. Klein described graphite as a semimetal, and he proposed a model which assumes parabolic bands, known as the Simple Two Band (STB) Model to describe the Fermi energy/carrier densities of graphite at high temperatures. This model is based on a carrier effective mass, an average carrier mobility, and an overlap energy. The different parameter values measured/calculated by Klein agree well with previous publications. Yet Klein provided simple expressions to determine the values of different parameters and their variation with temperature. For instance, he provided an expression to calculate the value of the intrinsic density of graphite and its variation with temperature. Klein also noted that the electron and hole densities are roughy equal [80]. This information motivated us to investigate the extent of the

19

equality/inequality among the electron, hole, and intrinsic densities.

Based on the fact that graphite is considered a zero-gap (crystalline) semiconductor, it will be used to bridge the gap between non-crystalline carbon materials and crystalline semiconductor materials. That is, the properties of graphite will be used in the two models introduced earlier in the chapter. This will allow us to analyze charge and heat transport of carbon materials using both models. Though the properties of graphite, biochar, and biomass are very different, it will allow us to have a representative case when using the hydrodynamic model.

Chapter 3

STEADY-STATE ONE-DIMENSIONAL
ELECTRIC-THERMAL DRIFT-DIFFUSION MODEL

3.1   Introduction

In this chapter, a steady-state one-dimensional version of the hydrodynamic model, Eqs. (2.4), is used for two purposes in mind: (1) to numerically quantify the difference between the electron, hole, and thermal densities; and (2) to analyze charge transport and Joule heating in intrinsic pyrolytic graphite rods. This model is referred to as a drift-diffusion steady-state one-dimensional electric-thermal model. The derivation of the drift-diffusion model starting from Eqs. (2.4) is given in detail in Appendix A.

It is noted here that this model used temperature-dependent material properties, something not done very commonly in the literature. It is important for us to use temperature-dependent properties because we are interested in reaching very high temperatures with this model.

The chapter is organized as follows: Sec. 3.2 presents the problem definition, and Sec. 3.3 presents the governing equations. The thermophysical properties of graphite are given in Sec. 3.4, and the results are given and discussed in Sec.3.5. A discussion about applying Joule heating to enhance the gasification process is given in Sec. 3.5.9, and lastly, the chapter is wrapped up with the conclusion in Sec. 3.6.

The main results from this chapter have been published as Ref. [96].

3.2 Description Of The Problem
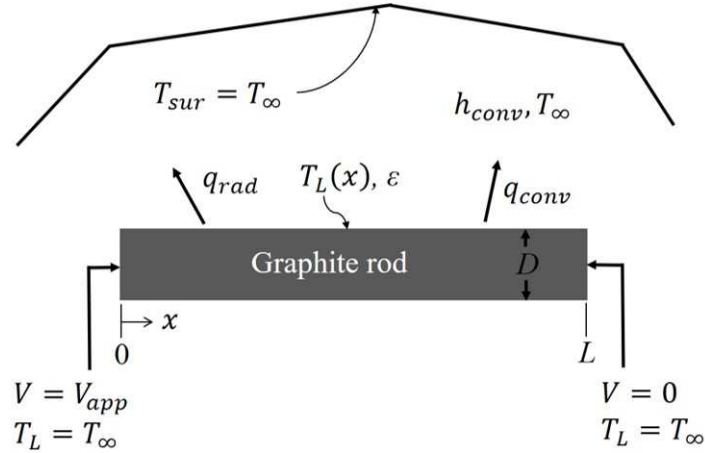
Figure 3.1: Schematic: Graphite rod under an applied voltage exposed to cooling by free convection and radiation.

In this work, a drift-diffusion steady-state one-dimensional mathematical model is developed to describe the charge carrier transport and lattice temperature distribution in a graphite rod of length L and diameter D, with $L \geq D$. Voltage drop, temperature changes, and transport of electrons and holes vary only along the x-direction, as shown in Fig. 3.1. A DC voltage, V_{app}, is applied on the left end of the rod while the right end is grounded. Due to the electric field, charge carriers, i.e., electrons and holes, move across the rod producing a total current density J, which generates Joule heating in the rod. Consequently, due to Joule heating, the lattice temperature rises and results in thermal generation of electrons and holes. Both ends of the rod have a fixed temperature equal to T_∞. The rod is exposed to heat losses by natural convection to the surrounding air and radiation exchange with the surrounding surfaces; the surfaces and the air are at the same temperature T_∞.

3.3 Governing Equations

This model is a subset of Eqs. (2.4), and it resembles the form of a drift-diffusion model, which has been used extensively in the analysis of charge transport in conventional semiconductors [44–46, 59], and more recently, in graphene devices [40, 42]. However, in this model there are no diffusion terms. This model has been derived in detail in Appendix A.

The set of equations is composed of the following: the potential distribution described by Gauss' Law in Eq. (3.1a), the continuity equations for electrons and

holes, Eqs. (3.1b) and (3.1c), the momentum equations for electrons and holes in Eqs. (3.1d) and (3.1e), and the equation for the lattice temperature (3.1f)

$$\frac{d^2V(x)}{dx^2} = -\frac{e}{\epsilon_r \epsilon_0}(n_h(x) - n_e(x)), \tag{3.1a}$$

$$\frac{d\left(-en_e(x)u_e(x)\right)}{dx} = -eG_{e,net}(x), \tag{3.1b}$$

$$\frac{d\left(en_h(x)u_h(x)\right)}{dx} = eG_{h,net}(x), \tag{3.1c}$$

$$u_e(x) = \mu_e(T_L)\frac{dV(x)}{dx} - \frac{\mu_e(T_L)k_B T_c}{e}\frac{1}{n_e(x)}\frac{dn_e(x)}{dx}, \tag{3.1d}$$

$$u_h(x) = -\mu_h(T_L)\frac{dV(x)}{dx} - \frac{\mu_h(T_L)k_B T_c}{e}\frac{1}{n_h(x)}\frac{dn_h(x)}{dx}, \tag{3.1e}$$

$$0 = \frac{d}{dx}\left(k_L(T_L)\frac{dT_L(x)}{dx}\right) - \frac{4h_{Tot}}{D}\left(T_L(x) - T_\infty\right)$$
$$- e\left(-n_e(x)u_e(x) + n_h(x)u_h(x)\right)\frac{dV(x)}{dx}, \tag{3.1f}$$

where $V(x)$ is the electrostatic potential, $n_e(x)$ is the electron density, $n_h(x)$ is the hole density, $u_e(x)$ is the electron velocity, $u_h(x)$ is the hole velocity, $T_L(x)$ is the lattice temperature, T_∞ is the ambient temperature, and $G_{e,net}(x)$ and $G_{h,net}(x)$ are the net generation rates of electrons and holes, respectively. Lattice temperature changes only occur along the x-direction. This approximation is valid because the Biot number is lower than 0.1 [97]. It is also assumed that the electrons and holes are in thermal equilibrium [59, 98], for which the temperature will be referred to as the carrier temperature, T_c. It is further assumed that T_c is constant throughout the rod, but it can be set to different values. Further details regarding these assumptions are provided in Appendix A. Having a carrier temperature different from the lattice temperature allows the analysis of non-equilibrium transport. It will be shown, however, that under the assumptions and operating conditions relevant to this study, the value of T_c does not have a significant effect on the results.

The physical parameters are the elementary charge, e, the permittivity of free space, ϵ_0, the relative permittivity (dielectric constant) of graphite, ϵ_r, Boltzmann constant, k_B, the mobility of electrons, $\mu_e(T_L)$, the mobility of holes, $\mu_h(T_L)$, and the thermal conductivity of graphite, $k_L(T_L)$, where the carrier mobilities and the thermal conductivity depend on the lattice temperature. The total heat transfer coefficient is defined as $h_{Tot} = h_{conv} + h_{rad}$, where h_{conv} is the convection coefficient and $h_{rad} = \varepsilon\sigma_{SB}(T_{L,ave} + T_\infty)(T_{L,ave}^2 + T_\infty^2)$ is the linearized radiation coefficient; ε is the emissivity of graphite and σ_{SB} is the Stefan-Boltzmann constant [97].

The current densities for electrons, $J_e(x)$, holes, $J_h(x)$, and the total current

density, J, are defined as follows:

$$J_e(x) = -en_e(x)u_e(x), \tag{3.2a}$$
$$J_h(x) = en_h(x)u_h(x), \tag{3.2b}$$
$$J = J_e(x) + J_h(x). \tag{3.2c}$$

Global current continuity requires the total current density to be constant, thus the following relationship holds

$$\frac{dJ}{dx} = \frac{d(J_e(x) + J_h(x))}{dx} = 0. \tag{3.3}$$

In addition, the electric field is related to the potential as

$$E(x) = -\frac{dV(x)}{dx}. \tag{3.4}$$

The net generation rate of electrons is equal to the net generation rate of holes, [99] that is

$$G_{e,net}(x) = G_{h,net}(x) = G_{net}(x). \tag{3.5}$$

This means that when an electron gains sufficient energy to jump from the valence band to the conduction band, a hole is created and left behind in the valence band.

Because we do not know the net generation rates explicitly, we take a different approach in solving the continuity equations for the electron and hole densities. Substituting Eqs. (3.1d) and (3.1e) into Eqs. (3.2), and rearranging, we get

$$J = -e\left(n_e(x)\mu_e(T_L) + n_h(x)\mu_h(T_L)\right)\frac{dV(x)}{dx}$$
$$+ k_B T_c \left(\mu_e(T_L)\frac{dn_e(x)}{dx} - \mu_h(T_L)\frac{dn_h(x)}{dx}\right). \tag{3.6}$$

Since intrinsic graphite is being used, the electron and hole mobilities are replaced with an average carrier mobility, $\mu_{ave}(T_L)$, hereafter called mobility. Thus,

$$J = 2e\mu_{ave}(T_L)n_{th}(T_L)E(x) - k_B T_c \mu_{ave}(T_L)\frac{d}{dx}\left(n_h(x) - n_e(x)\right), \tag{3.7}$$

where we have used the expression $2\mu_{ave}(T_L)n_{th}(T_L)$ in place of $n_e(x)\mu_e(T_L)+n_h(x)\mu_h(T_L)$; $n_{th}(T_L)$ is the thermal or intrinsic density. Thermal density and intrinsic density refer to the same parameter, and will be used interchangeably in this dissertation.

Graphite is sometimes referred to as a zero-gap semiconductor [89] or as a semimetal [79] because it does not have a band gap. Instead grahite has a small overlap between the valence band and the conduction band [79,80,91]. The presence of a band overlap indicates that the electron and hole densities are nearly equal to each other (and to the thermal density) [79, 80]. Based on the two-band model, the thermal density can be approximated as [80]

$$n_{th}(T_L) = \frac{16\pi m_c^\star}{h_P^2 c_0} k_B T_L \ln\left[1 + \exp\left(\frac{\mathcal{E}_{bo}}{2k_B T_L}\right)\right], \tag{3.8}$$

24

where $m_c^\star$ is the effective carrier mass, c_0 is twice the layer spacing, h_P is Planck's constant, and $\mathcal{E}_{bo}$ is the band overlap energy.

The first term on the right hand side of Eq. (3.7) is the drift current density, J_{Drift}, and the second term is the diffusion current density, J_{Diff}. Under the conditions used here, and using graphite properties, the drift current density becomes much larger than the diffusion current density for all physically meaningful values of the carrier temperature T_c. Thus, the diffusion term can be safely neglected, and the total current density is fully determined by the drift current density

$$J \approx 2e\mu_{ave}(T_L)n_{th}(T_L)E(x). \tag{3.9}$$

The group of parameters multiplying the electric field in Eq. (3.9) is defined as the electrical conductivity, $\sigma = 2e\mu_{ave}n_{th}$, and the well-known expression for current density may be obtained, $J = \sigma E$.

Making use of subsequent expressions, Eqs. (3.1) can be simplified and recast as follows:

$$J = 2e\mu_{ave}(T_L)n_{th}(T_L)E(x), \tag{3.10a}$$

$$0 = \frac{d}{dx}\left(k_L(T_L)\frac{dT_L(x)}{dx}\right) - \frac{4h_{Tot}}{D}\left(T_L(x) - T_\infty\right) + JE(x), \tag{3.10b}$$

$$E(x) = -\frac{dV(x)}{dx}, \tag{3.10c}$$

$$\frac{d^2V(x)}{dx^2} = -\frac{e}{\epsilon_r\epsilon_0}(n_h(x) - n_e(x)). \tag{3.10d}$$

The boundary conditions are as follows: $V = V_{app}$ at $x = 0$, $V = 0$ at $x = L$, and $T_L = T_\infty$ at $x = 0, L$, as shown in Fig. 3.1.

Experimental data suggests that the electron, hole, and thermal densities are nearly equal to each other [80], which may lead us to assume that they are exactly equal. However, in Sec. 3.5, it will be shown that for the biased intrinsic graphite rods, all three carrier densities are nearly equal to each other, but not exactly equal. Moreover, assuming their equality does not lead to a consistent solution. In addition, we will show that the maximum absolute difference among the carrier densities is several orders of magnitude smaller than the thermal density.

In the absence of a gate voltage, the small differences among the electron, hole, and thermal densities in intrinsic graphite are important because, though small, they give rise to non-constant electric fields. On the contrary, in graphene transistors, for example, the gate voltage gives rise to large differences among the electron, hole, and thermal densities, which results in very large variations in the electric field [40–42]. Therefore, the small differences in carrier densities of the intrinsic material become insignificant.

3.4 Thermophysical Properties Of Pyrolytic Graphite

The properties of pyrolytic graphite are presented in Table 3.1. The experimental data for the temperature-dependent mobility [80], from room temperature to

1000 K, was fitted with the following function, with an R^2 value of 0.9954, in order to use it in the simulations

$$\mu_{ave}(T_L) = 7211.2 T_L^{-1.555}. \tag{3.11}$$

Similarly, the experimental data for the temperature-dependent thermal conductivity [100, 101], was fitted with the following function, with an R^2 value of 0.9988,

$$k_L(T_L) = 839269.0 T_L^{-1.068}. \tag{3.12}$$

A value for the dielectric constant of graphite for a constant (DC) voltage was not found, but values were found for exfoliated graphite for frequencies as low as 50 Hz [102]. The values for washed and unwashed exfoliated graphite samples at 50 Hz were 38 and 364, respectively [102]. Nonetheless, there is an uncertainty as to how the dielectric constant changes at lower frequencies and for a DC voltage. On the other hand, dielectric constant values for conventional semiconductors are well known. For example, the values for Si and GaAs are 11.9 and 12.9, respectively [45]. Based on this information, a dielectric constant of 13 will be used for graphite throughout this dissertation. The effect of the dielectric constant will be analyzed and discussed in Sec. 3.5.

Table 3.1: Properties of pyrolytic graphite [80, 88, 100, 101].

Property	Symbol	Value
Twice the graphene layer spacing	c_0	0.672×10^{-9} m
Band overlap energy	$\mathcal{E}_{bo}$	0.01 eV
Emissivity	ε	0.8
Relative permittivity	ϵ_r	13.0
Free electron mass	m_0	9.109×10^{-31} kg
Effective carrier mass	$m_c^\star/m_0$	0.0125
Thermal conductivity at $T_L = 298$ K	$k_{L,ref}$	1911 W/(m K)
Ave. carrier mobility at $T_L = 298$ K	$\mu_{ave,ref}$	1.02 m^2/(V s)

Unless otherwise stated, the system parameter values used for cases $I.A,B$, and for some of the other cases, are listed in Table 3.2.

Table 3.2: System parameter values.

Parameter	Symbol	Value
Rod length	L	10^{-2} m
Rod diameter	D	10^{-3} m
Convection heat transfer coefficient	h_{conv}	10 W/(m^2 K)
Ambient temperature	T_∞	298 K

3.5 Results And Discussion

In the published literature, several approximations for the intrinsic density of pyrolytic graphite have been proposed based on available experimental data. A popular expression to calculate the intrinsic density of pyrolytic graphite, Eq. (3.8), has been developed by Klein [80] according to his two-band theory. The fact that there is a band overlap rather than a band gap means that there are nearly equal numbers of electron and holes. As a result, it has been generally assumed that the electron and hole densities are exactly equal. In this section, several cases are solved to demonstrate that although the electron and hole densities are nearly equal to each other and to the thermal density, there exists a small difference among them. In addition, the difference is also bounded to a maximum value dictated by material properties, geometry and operating conditions. The order of magnitude of the maximum absolute difference between holes and electrons is here quantified with the aid of Gauss' law in the form of the Poisson equation.

3.5.1 Exploring the equality of the electron, hole, and thermal densities

In this subsection, the consistency in the solution of the governing equations is analyzed based on the assumption of equality of the electron, hole, and thermal densities. From Eq. (3.3) we deduce that the total current density, J, is constant. Also, in Eqs. (3.10a) and (3.10b), the thermal density $n_{th}(T_L)$ and carrier mobility $\mu_{ave}(T_L)$ are dependent on the lattice temperature $T_L(x)$, and the electric field $E(x)$ is a function of position. In order to solve the system of equations, Eqs. (3.10) were discretized using a second order finite difference numerical scheme with a mesh of 101 nodes. Convergence was achieved when the maximum absolute relative error for temperature falls below a tolerance of $\delta = 10^{-5}$, i.e, $\max|T_{L,new} - T_{L,old}|/T_{L,new} \leq \delta$. The appropriate grid size and tolerance value were chosen based on a grid independence analysis.

Case I.A: $D = 10^{-3}$ m, $L = 10^{-2}$ m, and $V_{app} = 1.0$ V; assume $n_e(x) = n_h(x) \approx n_{th}(T_L)$. When $n_e(x) = n_h(x)$, the right side of Poisson's equation, Eq. (3.10d), becomes equal to zero, and Poisson's equation reduces to Laplace's equation, $d^2V/dx^2 = 0$. Solution of the Laplace equation leads to a linear voltage distribution, and consequently to a constant electric field $E(x) = E_0 = V_{app}/L$. The thermal density can be obtained from two expressions, i.e., directly from Eq. (3.8), or by rewriting Eq. (3.10a) in the form:

$$\tilde{n}_{th}(x) = \frac{J}{2e\mu_{ave}(T_L)E_0},\qquad(3.13)$$

where it has been labeled as $\tilde{n}_{th}$ to differentiate from the value of n_{th} obtained from Eq. (3.8).

The results obtained for this case are shown in Fig. 3.2, where the current density was obtained iteratively by evaluating the thermal density and the mobility at the average lattice temperature, and using a constant electric field, i.e., $J = 2e \mu_{ave}(T_{L,ave})n_{th}(T_{L,ave})E_0$. As expected, Fig. 3.2(a) shows a constant electric field and

27

a linear variation of the voltage due to the assumption of $n_e(x) = n_h(x)$. However, Fig. 3.2(b) shows that the values of n_{th} and $\tilde{n}_{th}$ are not equal, except in a couple of locations where the curves intersect each other, and thus, under this assumption, the system of equations is inconsistent. This solution suggests that the electric field should not be constant; and therefore the electron, hole, and thermal densities should be approximately equal but not exactly equal. Under these assumptions, the
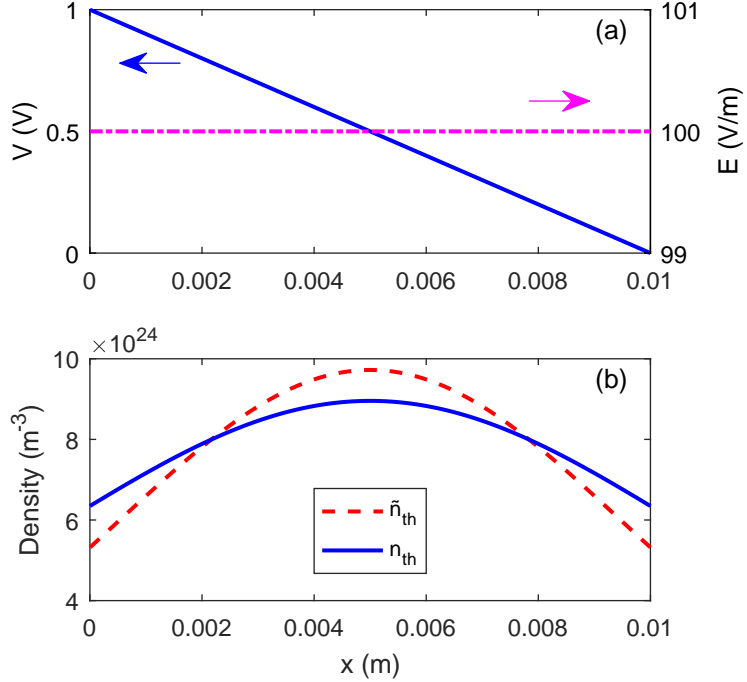
Figure 3.2: Results for *Case I.A*: $n_e(x) = n_h(x)$. Parameter values: $D = 10^{-3}$ m, $L = 10^{-2}$ m, $V_{app} = 1.0$ V.

only possibility for the electric field to be constant would be if $n_{th}(T_L)$ and $\mu_{ave}(T_L)$ had an exactly inversely proportional dependence on the lattice temperature $T_L(x)$. However this is not the case. The thermal density increases with temperature in a nearly linear fashion, while the mobility decreases much faster with temperature, following a power law.

Now that it has been determined that the electron, hole, and thermal densities are slightly different, the maximum absolute difference between electron and hole densities will be quantified in Subsection 3.5.2.

3.5.2 Quantification of the maximum absolute difference between hole and electron densities

The results shown in Subsection 3.5.1 suggest that while the hole and electron densities are nearly equal to each other and to the thermal density, i.e., $n_e(x) \approx$

$n_h(x) \approx n_{th}(T_L)$, there is a small difference between the hole and electron densities $|n_h(x) - n_e(x)| \ll n_{th}(T_L)$. On of the main objectives in this chapter is to numerically quantify the difference between hole and electron densities $n_h(x) - n_e(x)$, which may change along the rod. The first step is to quantify the maximum absolute difference, $\max|n_h(x) - n_e(x)|$, which may occur anywhere along the rod.

To simplify the analysis, the electric potential and the position parameter x will be nondimensionalized as follows: $V^* = V/V_{app}$, and $x^* = x/L$. Thus, Poisson's equation (3.10d) becomes

$$\frac{d^2V^*(x^*)}{dx^{*2}} = -\frac{eL^2}{\epsilon_r\epsilon_0 V_{app}}\max|n_h(x^*) - n_e(x^*)| \tag{3.14}$$

In order to quantify the maximum difference between hole and electron densities, only the magnitude of this value is considered, which is independent of position. Integrating Eq. (3.14) analytically from 0 to 1 yields the equation for a parabola

$$V^*(x^*) = \frac{eL}{2\epsilon_r\epsilon_0 E_0}\max|n_h(x^*) - n_e(x^*)|\left[x^* - x^{*2}\right] + \left[1 - x^*\right], \tag{3.15}$$

where $E_0 = V_{app}/L$.

Typical values for this problem are taken as length $L = 10^{-2}$ m and electric field of 100 V/m, where the dielectric constant used for graphite is 13.0. Substituting and simplifying, the following expression is obtained:

$$V^*(x^*) = (6.96 \times 10^{-14} \text{ m}^3)\max|n_h(x^*) - n_e(x^*)|\left[x^* - x^{*2}\right] + \left[1 - x^*\right]. \tag{3.16}$$

Because the units of the electron/hole densities are in m^{-3}, the units will cancel out upon multiplication. Although integration of the Poisson equation yields a parabolic equation, a nearly linear voltage distribution is expected. This means that the coefficient multiplying the quadratic term should be of order 1, nearly equal to the linear term. In order for this coefficient to have such magnitude, the maximum absolute difference between holes and electrons, $\max|n_h(x) - n_e(x)|$, must be of the order of 10^{14} m^{-3} or lower. The potential distribution using Eq. (3.16) was plotted for various values of $\max|n_h(x) - n_e(x)|$ in Fig. 3.3(a). It can be seen that as $\max|n_h(x) - n_e(x)|$ increases, the voltage distribution becomes more parabolic than linear, and the peak voltage is higher than the applied voltage. When the peak voltage becomes higher than the applied voltage, it is considered as a non-physical solution. In order to obtain a meaningful physical solution for the given length $L = 10^{-2}$ m and applied voltage $V_{app} = 1.0$ V, the maximum absolute difference, $\max|n_h(x) - n_e(x)|$, should be in the order of 10^{13} m^{-3}. As expected, this number is much smaller than the thermal density.

Based on this analysis, it can be estimated that in order to obtain a meaningful physical solution for the voltage distribution, the maximum difference between holes and electrons is limited to a certain value. This value is dictated directly by the dielectric constant of the material ϵ_r, the applied voltage V_{app}, the length L, and
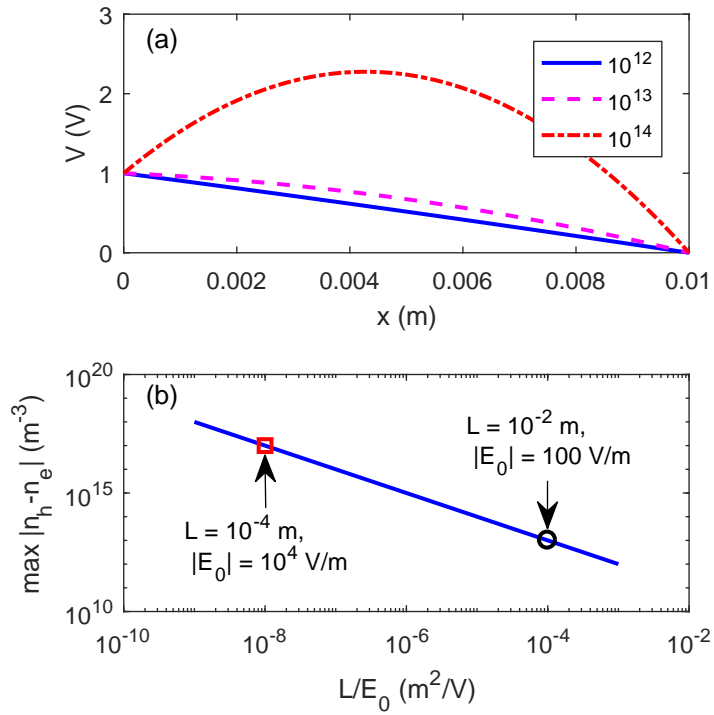
Figure 3.3: (a) Voltage distribution for various values of $\max|n_h(x) - n_e(x)|$ obtained with Eq. (3.16). Parameter values: $D = 10^{-3}$ m, $L = 10^{-2}$ m, $V_{app} = 1.0$ V, ($E_0 = 100$ V/m); legend: $\max|n_h(x) - n_e(x)|$ (m^{-3}). (b) $\max|n_h(x) - n_e(x)|$ vs. L/E_0.

indirectly affected by the carrier mobility μ_{ave}, the effective carrier mass $m_c^\star$, and diameter D.

On the other hand, in order to have a slightly nonlinear voltage distribution there needs to be a small difference between the electron and hole densities. Moreover, note that the electron, hole, and thermal densities vary along the rod due to a non-uniform temperature distribution; therefore, it is expected that the difference $n_h(x) - n_e(x)$ also varies along the length of the rod. In conclusion, it can be stated that for a given ϵ_r, knowing that $n_h(x) \approx n_e(x) \approx n_{th}(T_L)$, it is expected that $0 < \max|n_h(x) - n_e(x)| < \xi(L/E_0)$, where $\xi(L/E_0)$ is a function of L/E_0.

Poisson's equation can also be written incorporating the Reynolds number, Re, which is analogous to the Reynolds number used in fluid mechanics. Rewriting Eq. (3.14) we obtain

$$\frac{d^2 V^*(x^*)}{dx^{*2}} = -\frac{\mu_{ave}^2 m_c^\star}{\epsilon_r \epsilon_0} \frac{1}{\text{Re}} \max|n_h(x^*) - n_e(x^*)| \tag{3.17}$$

where the Reynolds number is defined as [59]

$$\text{Re} = \frac{\mu_{ave}^2 m_c^\star (|V_{app}|/L)}{eL} \tag{3.18}$$

In fluid mechanics, the Reynolds number quantifies the ratio of the inertia to the viscous forces; as Re increases the inertia forces dominate. Based on Eq. (3.18), for the given material properties μ_{ave}, m_{eff}, and ϵ_r, Re increases with E_0/L. Thus, as a consequence, $\max|n_h(x) - n_e(x)|$ increases with Re.

Before wrapping up this subsection, it is noted that the results were obtained using a value of 13 for the dielectric constant, ϵ_r. Because this value was not found, let us explore what happens when this value changes in magnitude. The dielectric constant is in the denominator on the coefficient multiplying the first term on the right-hand side of Eq. (3.15). Therefore, as ϵ_r increases the coefficient decreases and $\max|n_h(x) - n_e(x)|$ increases. For instance, if $\epsilon_r = 1300$ instead of 13, the coefficient in Eq. (3.16) is decreased by two orders of magnitude to 6.96×10^{-16} m^3. As a consequence, $\max|n_h(x) - n_e(x)|$ increases by two orders of magnitude as well.

3.5.3 Determining the spatial variation of the difference between hole and electron densities

The analyses in Subsections 3.5.1 and 3.5.2 showed that indeed the electron, hole, and thermal densities are nearly equal, yet slightly different. The order of magnitude of the maximum absolute difference between hole and electron densities was quantified in Subsection 3.5.2 under different operating conditions. In this subsection, the governing equations given by Eqs. (3.10) are solved consistently taking into account the discussions from Subsections 3.5.1 and 3.5.2, i.e., the electric field is not constant due to the fact that the electron and hole densities are not exactly

31

equal. The system of equations (3.10) is rewritten for convenience, and rearranged to resemble the numerical algorithm as follows:

$$E(x) = \frac{J}{2e\mu_{ave}(T_L)n_{th}(T_L)}, \tag{3.19a}$$

$$0 = \frac{d}{dx}\left(k_L(T_L)\frac{dT_L(x)}{dx}\right) - \frac{4h_{Tot}}{D}[T_L(x) - T_\infty] + JE(x), \tag{3.19b}$$

$$-\frac{dV(x)}{dx} = E(x), \tag{3.19c}$$

$$n_h(x) - n_e(x) = \frac{\epsilon_r\epsilon_0}{e}\frac{dE(x)}{dx} = -\frac{\epsilon_r\epsilon_0}{e}\frac{d^2V(x)}{dx^2}. \tag{3.19d}$$

The equations were discretized using finite differences. The algorithm is as follows: given an initial value for the total current density, Eqs. (3.19a) and (3.19b) are solved iteratively until convergence for temperature is obtained. Once the temperature converges, Eq. (3.19c) is integrated to determine the voltage distribution, and the voltage solution at the left boundary is compared to the applied voltage. If the solution voltage at the left end differs from the applied voltage by more than the given tolerance, $|(V_{app} - V(0))/V_{app}| \leq \delta$, the current density is increased/decreased accordingly; this procedure is a form of the shooting method. Equations (3.19a) through (3.19b) are then solved iteratively until convergence for both temperature and voltage is achieved. Consequently, Eq. (3.19d) is used to solve for $n_h(x) - n_e(x)$.

Case I.B: $D = 10^{-3}$ m, $L = 10^{-2}$ m, and $V_{app} = 1.0$ V. Results for this case are shown in Fig. 3.4, where it can be seen that the electric field is not constant, and its average magnitude is close to the nominal value $E_0 = V_{app}/L = 100$ throughout the rod. The fact that the electric field is not constant gives rise to a nonlinearity in the voltage distribution, which can be seen as a slight distortion on the almost linear solid line, shown in Fig. 3.4(a). The thermal density and the difference between the hole and electron densities are shown in Fig. 3.4(b). Because the thermal density has a nearly linear dependence with respect to temperature, the thermal density curve resembles that of the temperature distribution, reaching a maximum value slightly higher than 9×10^{24} m^{-3}. The difference between hole and electron densities is represented by the dashed black curve. It can be seen that the values vary approximately between $+0.5 \times 10^{13}$ m^{-3} and -0.5×10^{13} m^{-3}, displaying a non-symmetric distribution, where the difference becomes zero at the midpoint along the length of the rod. It is also observed that the maximum difference between holes and electrons coincides with the largest gradient of electric field and temperature, which in this case occurs near the boundaries. In addition, there are more holes than electrons on the left half of the rod due to the positive voltage and more electrons than holes on the right half of the rod near the grounded end. Although $\max|n_h(x) - n_e(x)| \ll n_{th}(T_L)$, the small difference gives rise to the small non-linearity in the voltage and a non-constant electric field. The operating conditions used for this case corresponds to the black circle depicted in Fig. 3.3(b). These results corroborate the hypothesis
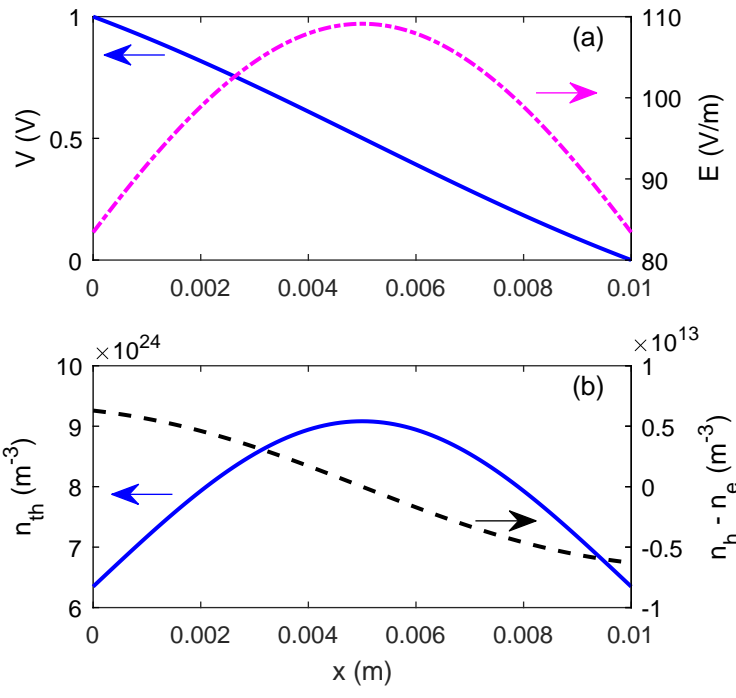
Figure 3.4: Results for *Case I.B* with parameter values: $D = 10^{-3}$ m, $L = 10^{-2}$ m, $V_{app} = 1.0$ V.

from Subsection 3.5.1 and the results from Subsection 3.5.2; and Eqs. (3.19) have been solved in a consistent fashion.

3.5.4 General results for both charge and heat transport parameters

In addition to the results shown in Subsection 3.5.3, Eq. (3.19b) is used to quantify the Joule heating power and the heat losses. Moreover, Eqs. (3.1b) and (3.1c) are used to compute the net generation terms for electrons and holes, respectively, and the second term on the right-hand-side of Eq. (3.7) is used to compute the diffusion current density, J_{Diff}.

Case I.B: in this case the parameter values from Table 5.3 are used together with an applied voltage, V_{app}, equal to 1.0 V to obtain the distribution of the lattice temperature, electric field, electron and hole densities, as well as, the Joule heating effect. These parameter values correspond to those used in case *I.A*. For consistency across the figures in this subsection, the results for *Case I.B* shown in Fig. 3.4 are included in Fig. 3.5. Fig. 3.5(c) shows the Joule heating power and heat losses due to convection and radiation, given in a per-unit-length basis.

The Joule heating power, P'_{Jh}, has an order of magnitude of about 1.5×10^4 W/m, about three to four orders of magnitude higher than the heat losses, $q'_{r+c} = (4h_{Tot}(T_L(x) - T_\infty)/D)A_c$. The heat losses are small due to the relatively small surface area of the rods. The temperature distribution profile is shown in Fig. 3.5(d). The maximum temperature reaches about 173 °C in the middle of the rod, due to the symmetric boundary conditions.

The electron and hole velocities are equal in magnitude, but have opposite signs. Their magnitude ranges from about 85 m/s at the boundaries to a minimum of about 60 m/s in the middle of the rod, see Fig. 3.5(e). The velocity is proportional to the mobility, and because the mobility decreases with temperature, so does the velocity. Since the mobility has an order of magnitude close to one, the magnitude of the velocity follows closely the magnitude of the electric field. The total, electron and hole current densities are shown in Fig. 3.5(f). The total current density has a constant value of about 1.74×10^8 A/m². It is the sum of the electron and hole densities, which have equal values. The diffusion current density is shown in Fig. 3.5(g). Its value was calculated using a carrier temperature, $T_c = 298$ K. It can be seen that its value is positive, varies with position, and is several orders of magnitude lower than the total current density. For this case, T_c would have to be several orders of magnitude higher in order for the diffusion current density to have a significant contribution to the total current density. Thus, this result corroborates the assumptions made in Sec. 3.3, i.e., $J \approx J_{Drift}$, and $J_{Diff} \approx 0$.

The net generation rates for electrons and holes are shown in Fig. 3.5(h). Both values are negative and equal to each other, as mentioned in Sec. 3.3. The value of the net generation rate is negative, meaning that recombination rate is larger than the generation rate. The absolute value of the net generation rate is in the order of 10^{16} m⁻³ s⁻¹. The curve shows a significant amount of noise because G_{net} is obtained
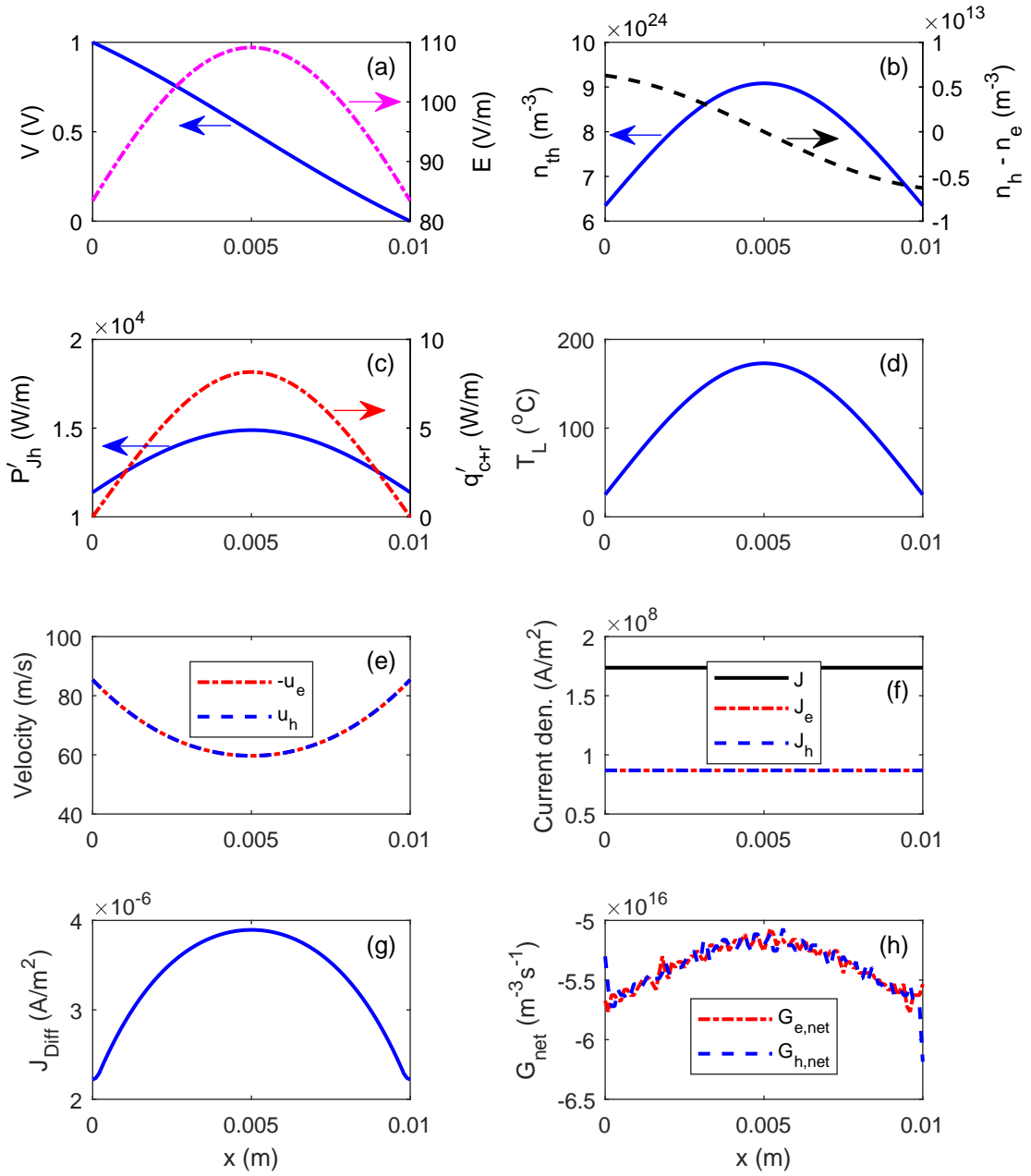
Figure 3.5: Results for *Case I.B* with parameter values: $V_{app} = 1.0$ V, $L = 10^{-2}$ m, $D = 10^{-3}$ m.

35

by dividing over the elementary charge, which has an order of magnitude of 10^{-19}. Also, G_{net} is a secondary variable, i.e., it is calculated after the overall solution of the problem is obtained.

At this time it is noted that the results presented in Subsections 3.5.3 through 3.5.9 were obtained using a dielectric constant value of 13. Additional cases were run using higher values of ϵ_r to determine its effect on the overall results. However, except for increases in the difference between electrons and holes there are no visible changes to the rest of the results.

Case II: the parameter values from Table 5.3 are used again, but with an applied voltage, $V_{app} = -2.0$ V, in order to analyze the effects of polarity and magnitude of the applied voltage. The voltage distribution and the electric field are shown in Fig. 3.6(a). The electric field has a larger variation, and therefore, the non-linearity of the voltage distribution is more pronounced compared to *Case I.B.*

The thermal density and the difference between the hole and electron densities are shown in Fig. 3.6(b). It can be seen that the magnitude of the difference increased compared to *Case I.B.* A maximum absolute difference between holes and electrons of about 0.5×10^{13} m^{-3} was calculated for *Case I.B* compared to about 2.7×10^{13} m^{-3} for *Case II.* Also, because the polarity of the voltage changed, the variation of the difference between holes and electrons changed, there are more electrons on the left half of the rod and more holes on the right (grounded) half.

The Joule heating power and heat losses are shown in Fig. 3.6(c), where it is seen that the magnitude of both the Joule heating power and the heat losses increased with voltage. The maximum Joule heating power increased from 1.49×10^4 W/m for *Case I.B* to 4.86×10^4 W/m for *Case II*, while the maximum heat losses increased from 8.16 W/m for *Case I.B* to 85.4 W/m for *Case II.* Although the heat losses increased more with voltage, the order of magnitude of the Joule heating power is still about two to three orders of magnitude higher.

The temperature distribution is shown in Fig. 3.6(d), where the maximum temperature increased from 173 °C for *Case I.B* to 763 °C for *Case II.* The total current density for *Case II* is -2.42×10^8 A/m^2, which is about a 39% increase from the *Case I.B.* This result suggests that the Joule heating power (or total current density), does not vary linearly with applied voltage. This will be explored and discussed in more detail in Secs. 3.5.6 and 3.5.9.

The electron/hole velocities are shown in Fig. 3.6(e). Because the applied voltage changed sign from positive to negative, their values also changed sign. The magnitude of the velocities increased due to the increase in applied voltage. The total current density also changed sign due to the negative applied voltage, it is shown in Fig. 3.6(f). Its magnitude increased to 2.42×10^8 A/m^2. Again, its value is the sum of the electron and hole current densities, which are equal in magnitude.

The diffusion current density is shown in Fig. 3.6(g). Its value varies between about $+1.26 \times 10^{-5}$ A/m^2 near the boundaries to about -7.83×10^{-6} A/m^2 at the middle. In this case the diffusion current density became negative at and around
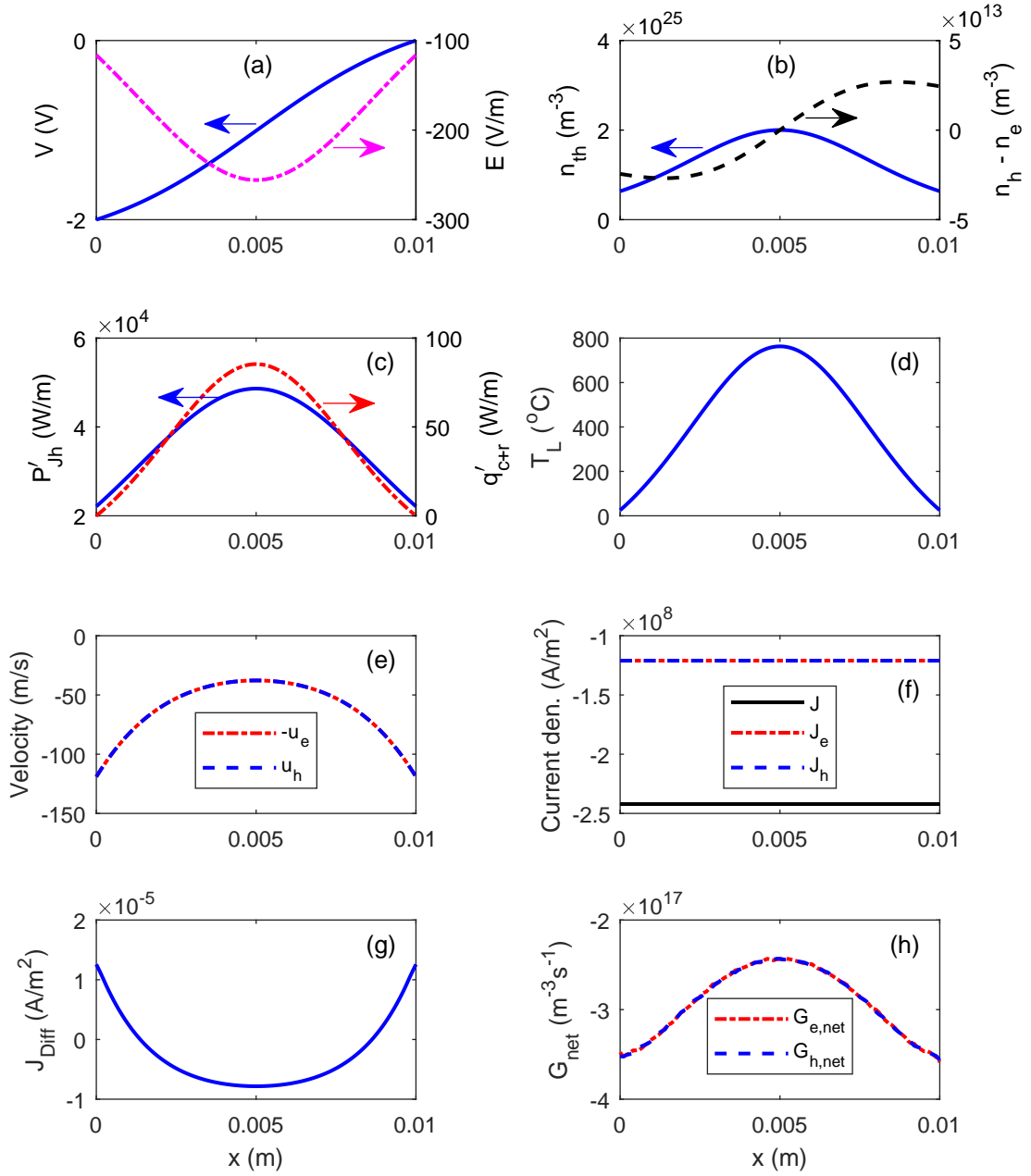
Figure 3.6: Results for *Case II* with parameter values: $V_{app} = -2.0$ V, $L = 10^{-2}$ m, $D = 10^{-3}$ m.

the middle section. This means that while electrons and holes are diffusing to the right near both boundaries, the are diffusing to the left near the middle. In addition, the order of magnitude is still similar to *Case I.B*. The net generation rate is shown in Fig. 3.6(h). The values still remain negative, but about one order of magnitude higher than *Case I.B*.

As discussed previously, both the thermal conductivity and mobility are dependent on the lattice temperature, and results were obtained and analyzed using the temperature-dependent values, cases *I.B* and *II*. Several more cases are solved assuming quasi-constant values for k_L, μ_{ave}, and n_{th}. Thus, a single value of k_L, μ_{ave}, and n_{th} evaluated at the lattice average temperature, $T_{L,ave}$, will be used across the rod. To a lesser extent, this methodology still allows to take into account the effect of the increasing temperature without having to evaluate k_L and μ_{ave} at each node. Thus, saving some computational effort, especially in transient modeling. However, making such simplifications may reduce the accuracy of the results, as will be shown next.

Case I.B.1: uses the same parameter values as in *Case I.B*, but with $k_L = k_L(T_{L,ave})$. The results for this case are shown in Fig. 3.7. Comparing these results to the results from *Case I.B*, it is observed that $E(x)$, $V(x)$, $n_{th}(x)$, $P'_{Jh}(x)$, $q'_{r+c}(x)$, $u_h(x)$, and $u_e(x)$ remain nearly equal. The difference $n_h(x) - n_e(x)$ has less curvature, and its magnitude reaches slightly larger values near the boundaries, Fig. 3.7(b); the temperature curve is smoother, Fig. 3.7(d), and $T_{L,max} = 185$ °C, which is 12 degrees higher than *Case I.B*; J had a small decrease, seen in Fig. 3.7(f), from 1.74×10^8 A/m^2 to 1.70×10^8 A/m^2; the curvature of J_{Diff} flipped, Fig. 3.7(g), and its magnitude decreased by about ten times; lastly, the value of G_{net}, shown in Fig. 3.7(h), increased by nearly one order of magnitude. In this case, $T_{L,max}$ reached a higher value because the thermal conductivity near the boundaries has a smaller magnitude, since k_L decreases significantly with temperature, therefore, less heat is dissipated to the boundaries. In addition, because the electrical conductivity of pyrolytic graphite decreases with temperature, the total current density also decreased by a small amount.

Case I.B.2: uses the same parameter values as in *Case I.B*, but with $k_L = k_L(T_{L,ave})$ & $\mu_{ave} = \mu_{ave}(T_{L,ave})$. The results for this case are shown in Fig. 3.8. Comparing to *Case I.B*, it is readily observed that the curvature of the electric field is flipped, Fig. 3.8(a), and its highest magnitude has increased from about 109 to 127 V/m. The fact that the electric field is lower near the middle of the rod is due to the higher temperature at this location. Recall that $\sigma = 2e\mu_{ave}n_{th}$, and in this case we have only evaluated μ_{ave} at $T_{L,ave}$, while n_{th} has been evaluated at the local temperature at each node. This means that while μ_{ave} has a constant value across the rod, the magnitude of n_{th} will increase from the boundaries to the middle of the rod. Thus, σ increases in the same manner, i.e., σ increases with temperature, which contradicts the real dependency with temperature. Since $J = \sigma E$ is constant, higher values of σ mean lower values of E. The voltage curve, Fig. 3.8(a) has changed from a "Z" shape
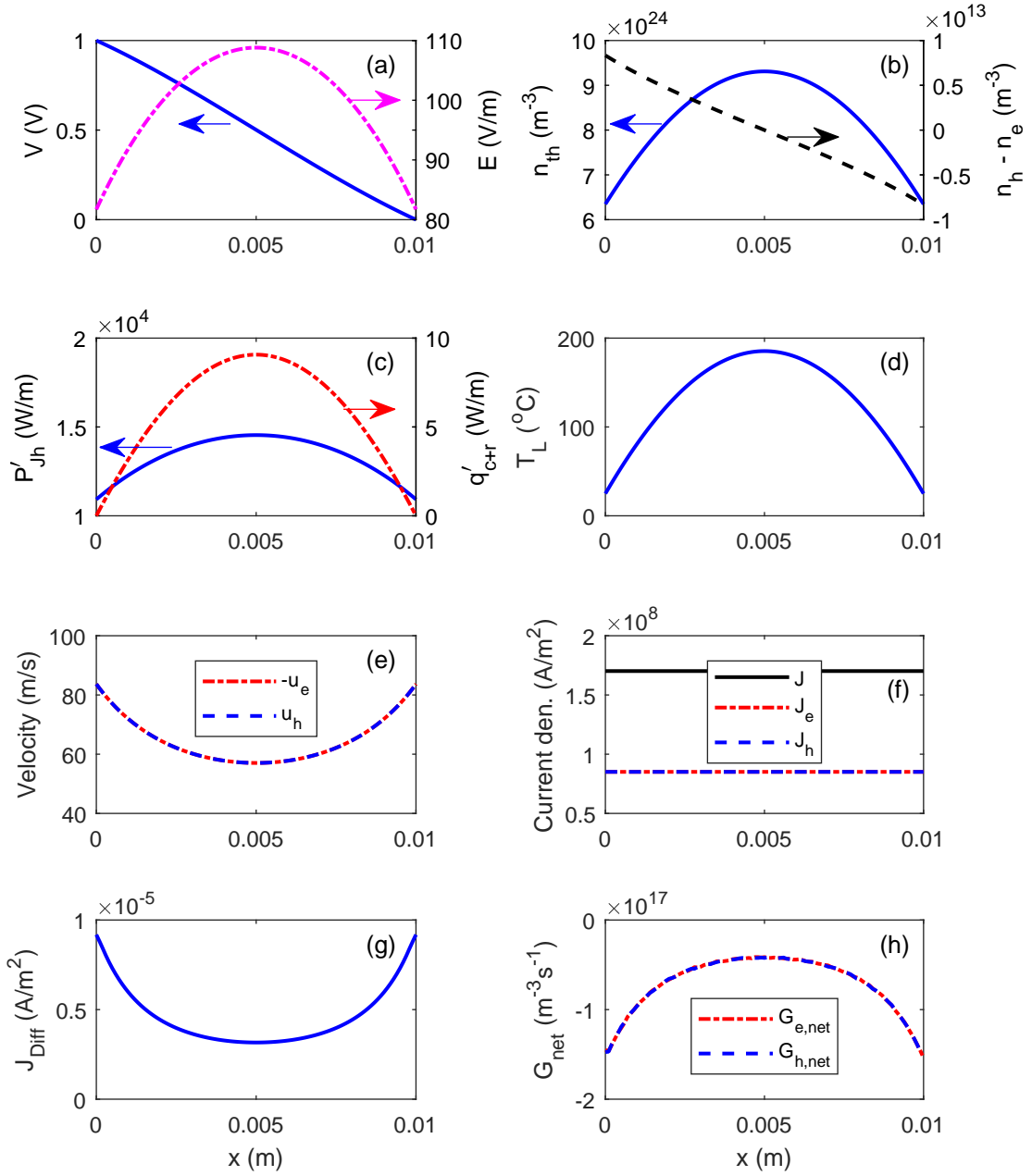
Figure 3.7: Results for *Case I.B.1:* $k_L = k_L(T_{L,ave})$, with parameter values: $V_{app} = 1.0$ V, $L = 10^{-2}$ m, $D = 10^{-3}$ m.
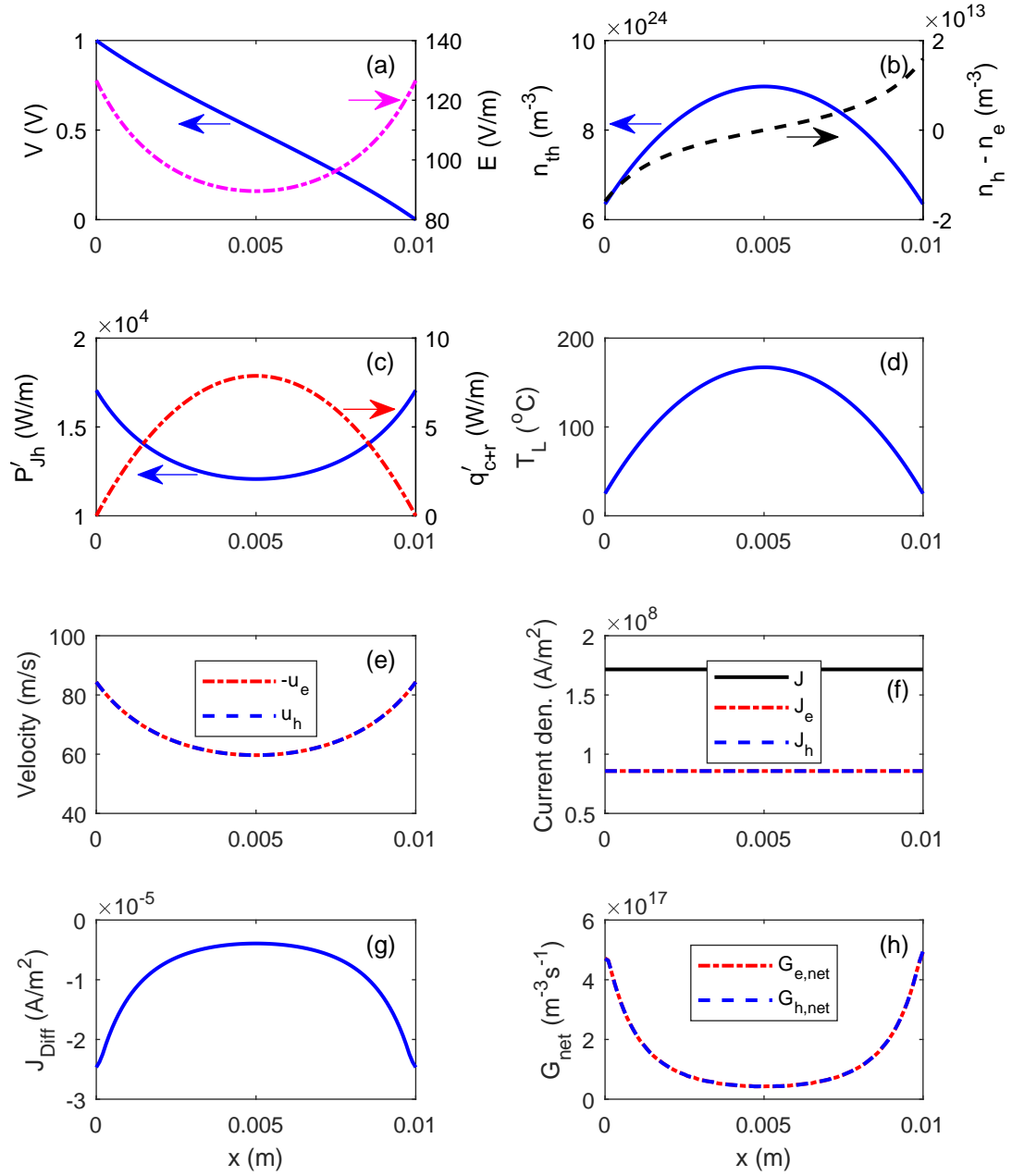
Figure 3.8: Results for *Case I.B.2:* $k_L = k_L(T_{L,ave})$, $\mu_{ave} = \mu_{ave}(T_{L,ave})$, with parameter values: $V_{app} = 1.0$ V, $L = 10^{-2}$ m, $D = 10^{-3}$ m.

to an "S" shape, and the curvature is more pronounced. While the thermal density remains nearly the same, the difference between holes and electrons increases monotonically from left to right, Fig. 3.8(b), and the magnitude also increases by about a factor of three compared to *Case I.B*. The curvature of the Joule heating curve also flips, following the shape of the electric field, while the magnitude increases near the boundaries and decreases around the middle of the rod, Fig. 3.8(c); the curvature and magnitude of the heat losses remains about the same. The temperature distribution again is smoother, Fig. 3.8(d), and $T_{L,max}$ reaches 167 °C, which is 6 degrees lower than *Case I.B*. This occurs because the Joule heating (and electric field) has a smaller magnitude than *Case I.B* near the middle of the rod. The carrier velocities, $u_h(x)$ & $u_e(x)$, Fig. 3.8(e), are also nearly equal to *Case I.B*. The velocities depend on both the mobility and electric field, and because the mobility is constant the velocities have a scaled curvature of the electric field. The total current density, $J = 1.72 \times 10^8$ A/m^2, Fig. 3.8(f), which is slightly smaller than *Case I.B*. The diffusion current density has changed sign from positive to negative, Fig. 3.8(g), and the magnitude is one order smaller than *Case I.B*. Lastly, the net generation rate is positive, Fig. 3.8(g), with an order of magnitude of 10^{17} m^{-3}s^{-1}.

Case I.B.3: uses the same parameter values as in *Case I.B*, but with $k_L = k_L(T_{L,ave})$, $\mu_{ave} = \mu_{ave}(T_{L,ave})$, and $n_{th} = n_{th}(T_{L,ave})$. The fact that both the mobility and the thermal density have a constant value across the rod means that the electrical conductivity also has a constant value across the rod. This causes several curves to also be constant across the rod, such is the case for $E(x)$, $n_h(x) - n_e(x) = 0$, $P'_{Jh}(x)$, $u_h(x)$ & $u_e(x)$, $J_{Diff} = 0$, and $G_{net} = 0$, as shown in Fig. 3.9. A constant electric field yields a linear voltage distribution as seen on Fig. 3.9(a). A constant electric field also creates a difference between electrons and holes equal to zero, Fig. 3.9(b), though the curve shows a small value near the boundaries due to numerical error. The Joule heating power has constant value of 1.34×10^4 W/m, Fig. 3.9(c), which appears to be the mean power when compared to case I.B. The heat losses, Fig. 3.9(c), remain about equal because the lattice temperature is nearly the same as *Case I.B*. The lattice temperature, Fig. 3.9(d), reaches a maximum value of 178 °C, 5 degrees hotter than *Case I.B*. The carrier velocities, Fig. 3.9(e), have a constant value of 65.1 m/s, which is 5 m/s faster than the minimum velocity from *Case I.B*. The current density, Fig. 3.9(f), has a value of $J = 1.71 \times 10^8$ A/m^2, compared to $J = 1.74 \times 10^8$ A/m^2 from *Case I.B*. The diffusion current density and the net generation rate are both zero, Figs. 3.9(g) & 3.9(h), respectively.

While using a constant value of the thermal conductivity only shifts the curves slightly, evaluating the mobility, or both the mobility and the thermal density, at the average lattice temperature affects the results quite significantly. However, the temperature distribution and the total current density remain relatively equal to those values from case I.B. If this are the only results of interest, then the the quasi-constant values for the mobility and thermal conductivity can be used to produce the desired results knowing that the results will contain some error. However, if one
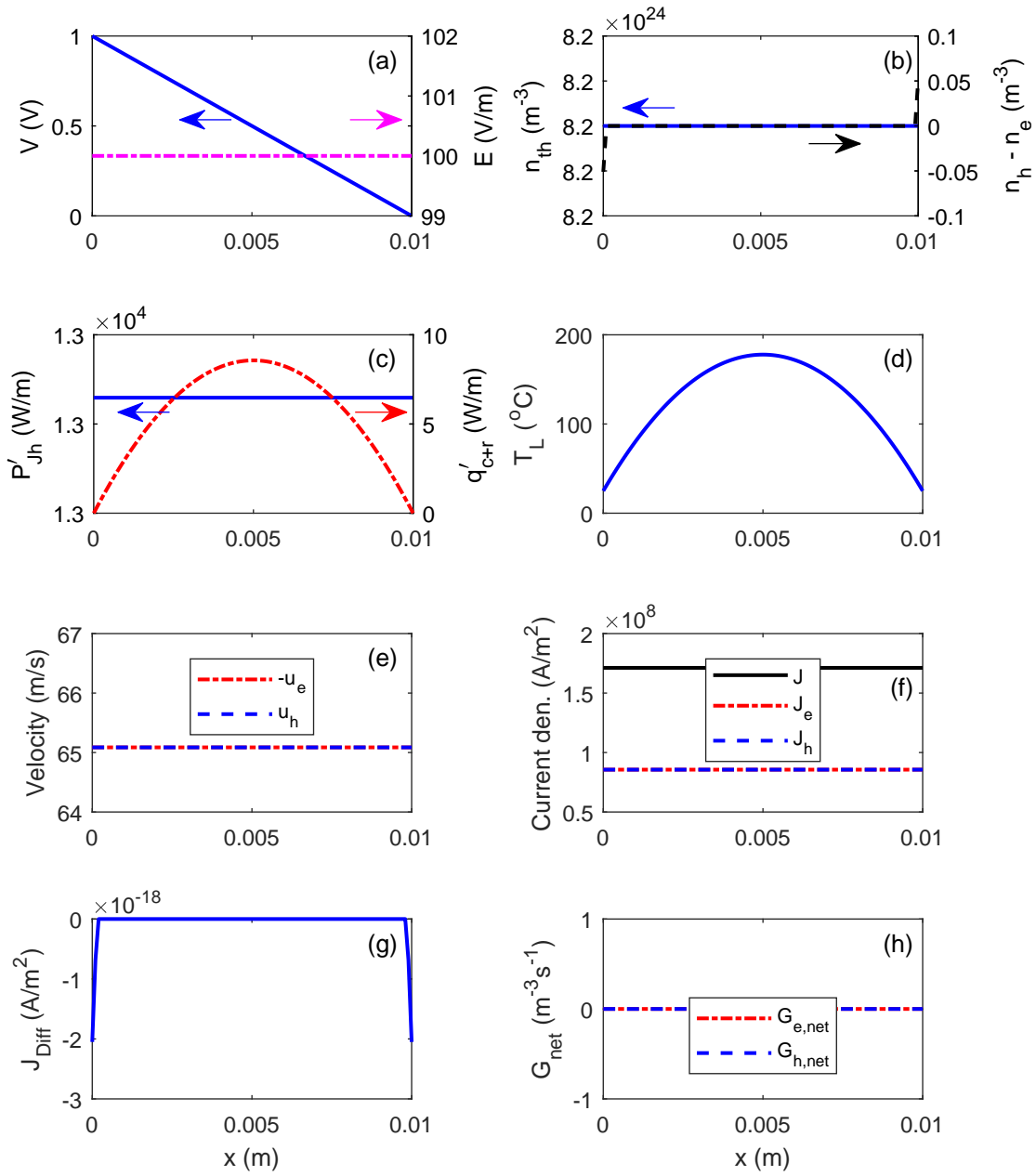
Figure 3.9: Results for *Case I.B.3:* $k_L = k_L(T_{L,ave})$, $\mu_{ave} = \mu_{ave}(T_{L,ave})$, $n_{th} = n_{th}(T_{L,ave})$ with parameter values: $V_{app} = 1.0$ V, $L = 10^{-2}$ m, $D = 10^{-3}$ m.

desires an accurate account of the rest of the parameters, one needs to evaluate the temperature-dependent values at each node.

It is also noted that when the applied voltage was set to 2 Volts, keeping the rest of the parameters the same, i.e, *Case II*, it took less than 1,000 iterations for the voltage to converge and less than 100 iterations for temperature to converge. In contrast, for the cases using quasi-constant values, similar to cases *I.B.1* through *I.B.3*, with $V_{app} = 2.0$ V, the code exceeded 1,000,000 iterations and still did not converge. Nonetheless, if the properties are kept constant at a given temperature, the code converges faster than when using temperature-dependent properties. Though the similar trends as using quasi-constant values are obtained.

3.5.5 Comparison with published results

In order to verify the model developed in this work, the temperature distribution obtained with the present model is compared to the analytical expression for steady-state temperature distribution for graphene, nanowires, and filaments developed by Chandran [103]. His analytical expression was validated against experimental data from Ref. [104]. In his work, the steady-state temperature distribution is determined from knowledge of the volumetric power generation, end contact temperature, and ambient temperature as follows:

$$T_L(x) = T_{L,ec} + \left[\frac{P_{Jh}''' A_c}{h_{conv} p} + T_\infty - T_{L,ec} \right] \left[1 - \frac{\cosh(\sqrt{h_{conv} p / k_L A_c} x)}{\cosh(\sqrt{h_{conv} p / k_L A_c} l)} \right] \quad (3.20)$$

where $T_L(x)$ is the steady-state temperature distribution, $T_{L,ec}$ is the end contact temperature, P_{Jh}''' is the volumetric power generation due to Joule heating, A_c is the cross-sectional area, h_{conv} is the convection heat transfer coefficient, p is the perimeter, T_∞ is the ambient temperature, k_L is the thermal conductivity, and l is half the length of the rod. The parameter values used are as follows: $V_{app} = -1.2$ V, $L = 2l = 10^{-4}$ m, $D = 10^{-5}$ m, $k_L = 1100$ W/(m K), $h_{Tot} = h_{conv} = 10$ W/(m^2 K), with no radiation losses, and where $T_{L,ec} = T_\infty = 298$ K. The temperature distributions are compared in Fig. 3.10. The solid black line is the temperature distribution obtained with our model, and the dashed blue line is the temperature distribution obtained using Eq. (3.20). The results show very good agreement, with only a 15 degree difference on the peak temperature. Note that the Joule heating power on Eq. (3.20) is constant, i.e., it is defined as the total input power divided by the total volume $P_{Jh}''' = JV_{app}/L$ =constant, whereas, in our model, in addition to this constant value, we also know the Joule heating power variation in space $P_{Jh}'''(x) = JE(x)$; the Joule heating power varies in space due to the temperature dependence of the mobility and carrier density. If we were to use this definition on Eq. (3.20), though not strictly correct, a temperature distribution would be as shown by the red dotted line in Fig. 3.10. In this case there is also about 15 degrees of difference on the peak temperature. Finally, it is mentioned that the comparison of the results is limited to that of the lattice temperature distribution as this is the only relevant solution found in the literature.
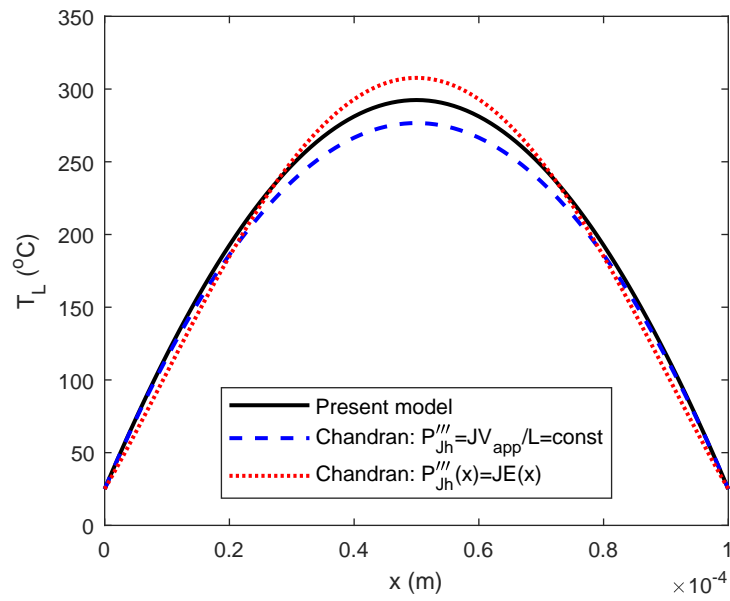
Figure 3.10: Comparison of temperature distribution with the published expression by Chandran [103]. Parameter values: $V_{app} = -1.2$ V, $L = 10^{-4}$ m, $D = 10^{-5}$ m, $k_L = 1100$ W/(m K), $h_{Tot} = h_{conv} = 10$ W/(m^2 K), no radiation losses, $T_{L,ec} = T_\infty = 298$ K.

44

3.5.6   Parametric analyses

The developed model is used in this section to perform several parametric analyses to investigate the effects of applied voltage, rod diameter, rod length, and heat transfer coefficient.

Applied voltage: The first parametric analysis consisted in increasing the applied voltage from 0.2 to 2.0 V, for which the results are shown in Figs. 3.11 and 3.12. The results for the thermal density are shown in Fig. 3.11(a), while the temperature distributions are shown in Fig. 3.11(b). Since the thermal density depends almost linearly with temperature, both curves show a similar behavior. While the maximum temperature for an applied voltage of 0.4 V increases to about 47 °C, the maximum temperature for 2.0 V reaches about 763 °C, showing a nonlinear increase of temperature with respect to applied voltage.

The results for Joule heating power are shown in Fig. 3.11(c), and the heat losses are shown in Fig. 3.11(d). It is observed that both Joule heating power and heat losses increase with voltage, where the Joule heating power is about three orders of magnitude larger than the heat losses, producing the sharp temperature increase with higher applied voltages.

Figure 3.12 summarizes the parametric study for applied voltage in terms of two important parameters: total current density, J, and maximum lattice temperature, $T_{L,max}$. It is seen that as the applied voltage increases from 0.2 V to 2.0 V, the current density increases. However, for higher applied voltages, the current density tends to reach a saturation value. On the other hand, as the applied voltage is set to higher values, $T_{L,max}$ increases almost exponentially. Because the electrical conductivity decreases with temperature, the current density does not increase linearly with voltage, thus, the current density shows this saturation effect.

Rod diameter: The second parametric study consisted of increasing the rod diameter from 0.5 mm to 8.0 mm, for which the results are shown in Fig. 3.13. This study revealed that there is negligible change on the heat losses due to an increase in diameter within the stated range. Therefore, there is only a small change on the maximum temperature and total current density. While the total current density slightly decreases with increasing diameter, the maximum temperature increases only a fraction of a degree. The small decrease in current density is mainly due to the slight increase in temperature, for as the temperature increases the electrical conductivity ($\sigma = 2e\mu_{ave}n_{th}$) decreases, and so does the current density. The nonlinearity arises because the cross sectional area depends on the square of the diameter.

Heat transfer coefficient: The third parametric study consisted of increasing the convection heat transfer coefficient from 1.0 to 100.0 W/(m^2 K), for which the results are shown in Fig. 3.14. As indicated before, the linearized radiative heat transfer coefficient is a function of temperature, and is included in these simulations. In this case, higher convection coefficients translate into slightly larger heat losses that result
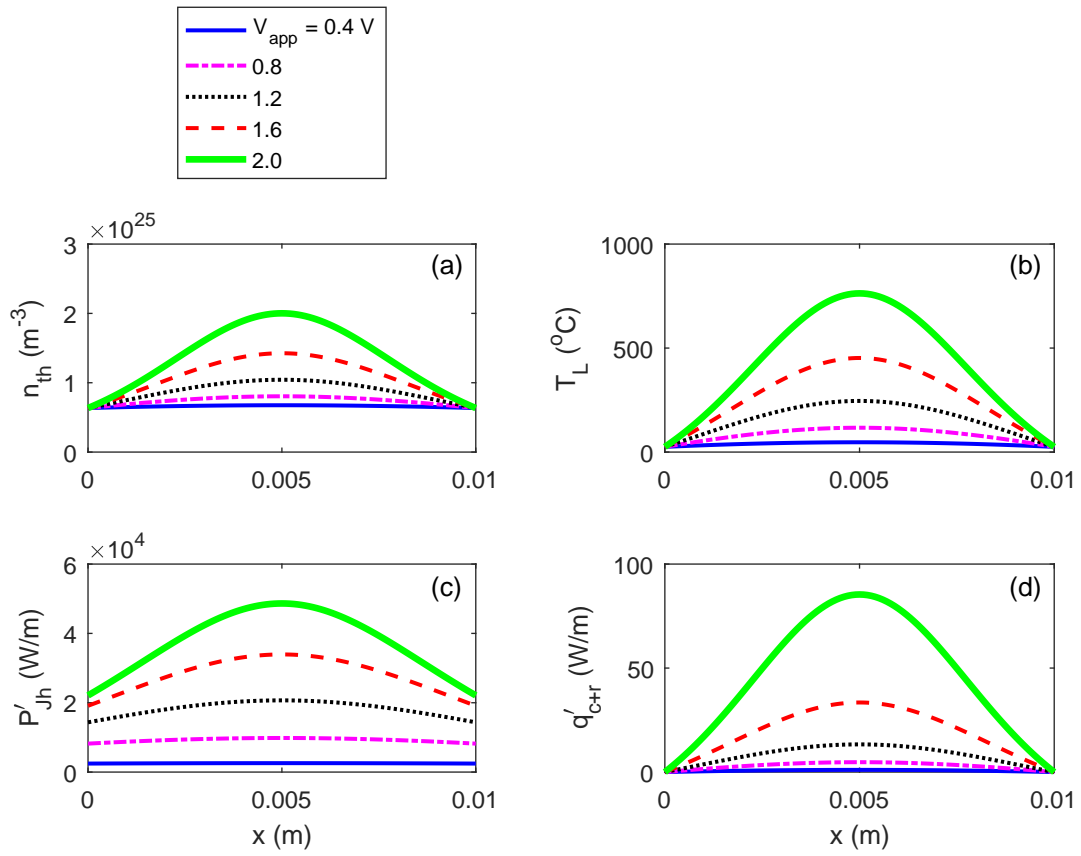
Figure 3.11: Parametric study based on *Applied voltage*. Parameter values: $L = 10^{-2}$ m and $D = 10^{-3}$ m.
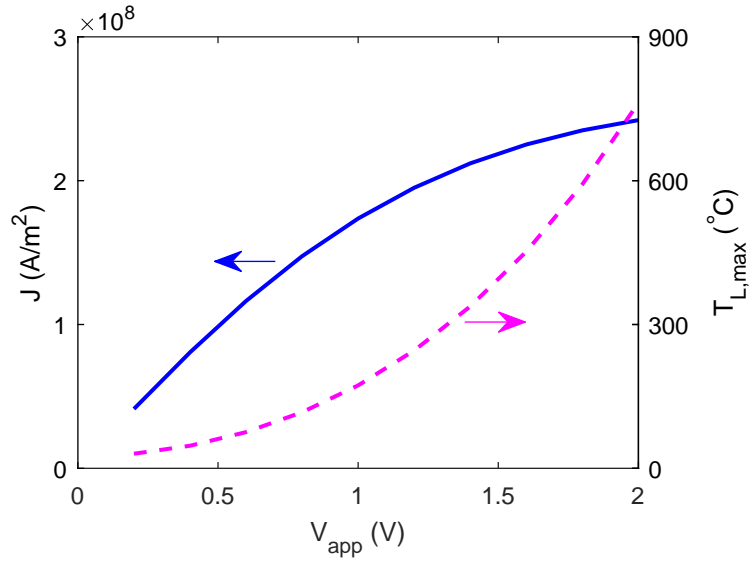
Figure 3.12: Parametric study based on *Applied voltage.* Parameter values: $L = 10^{-2}$ m and $D = 10^{-3}$ m.
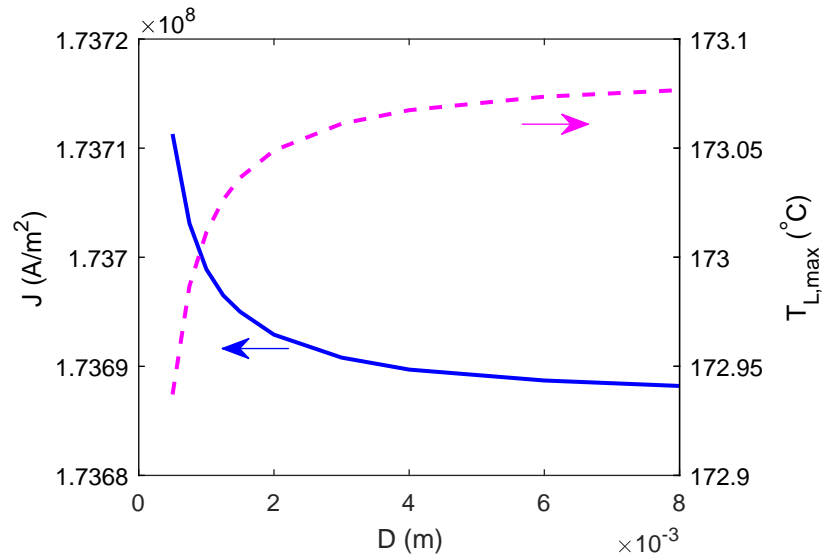
Figure 3.13: Parametric study based on *Rod diameter:.* Parameter values: $V_{app} = 1.0$ V and $L = 10^{-2}$ m.

in a reduction in temperature of less than half of a degree. Although the convection coefficient was increased by two orders of magnitude, the heat losses are still relatively small because of the small surface area of the rods. A linear dependency on h_{conv} of both, the total current density and maximum temperature is observed.
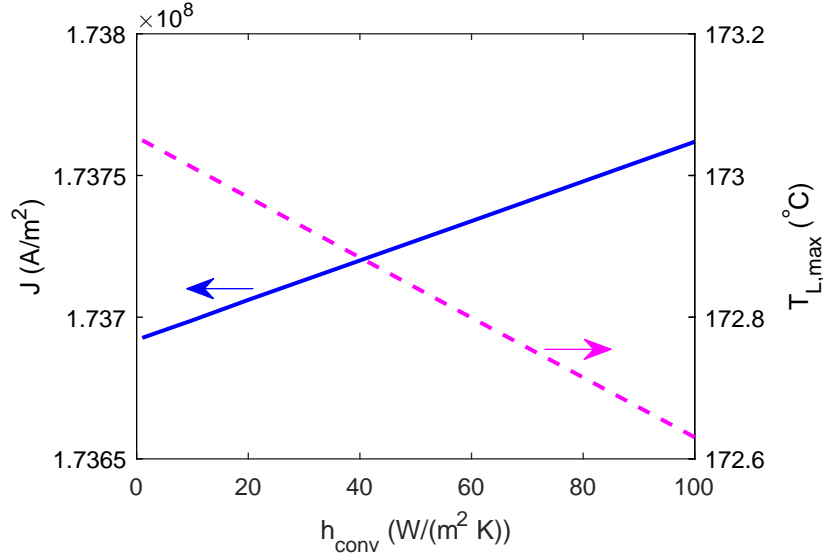
Figure 3.14: Parametric study based on *Heat transfer coefficient*. Parameter values: $V_{app} = 1.0$ V, $L = 10^{-2}$ m, and $D = 10^{-3}$ m.

Rod length: The fourth parametric study consisted of varying the rod length while keeping all other parameters constant; the length was varied from 0.5×10^{-3} to 1.0×10^{-2} m with a diameter of 0.5×10^{-3} m, and an applied voltage of 1.0 V. The dependence of the total current density and maximum lattice temperature with length is shown in Fig. 3.15. It is observed that initially the total current density has a sharp decrease with length, then it levels off as the magnitude of the length is increased further. Although the maximum temperature remains virtually constant, meaning negligible changes in the resistivity of graphite, larger lengths translate into larger resistances. Under a fixed applied voltage, the average electric field decreases with length, therefore, larger resistances are generated by longer rod lengths, which coupled to lower average electric fields, result in smaller current densities. The fact that the maximum lattice temperature remains virtually constant is attributed to the fact that the thermal conductivity of pyrolytic graphite is rather high and the boundaries act as heat sinks, and for shorter rod lengths more heat is dissipated into the boundaries.

Figure 3.16 shows more detailed results for a few selected rod lengths, i.e., $L = 0.5 \times 10^{-3}$, 1.0×10^{-3}, 5.0×10^{-3}, 10×10^{-3} m, where the positions along the rod have been normalized with the respective length for each simulated case. The voltage and electric field distributions are shown in Figs. 3.16(a) and 3.16(b),

respectively. Because the applied voltage is fixed, increasing the length decreases the magnitude of the electric field. The difference between holes and electrons is shown in Fig. 3.16(c), where the magnitude decreases with larger lengths, which agrees with the trends shown in Figs. 3.5 & 3.6. Lastly, the Joule heating power also decreases with length because both the current density and the electric field decrease.
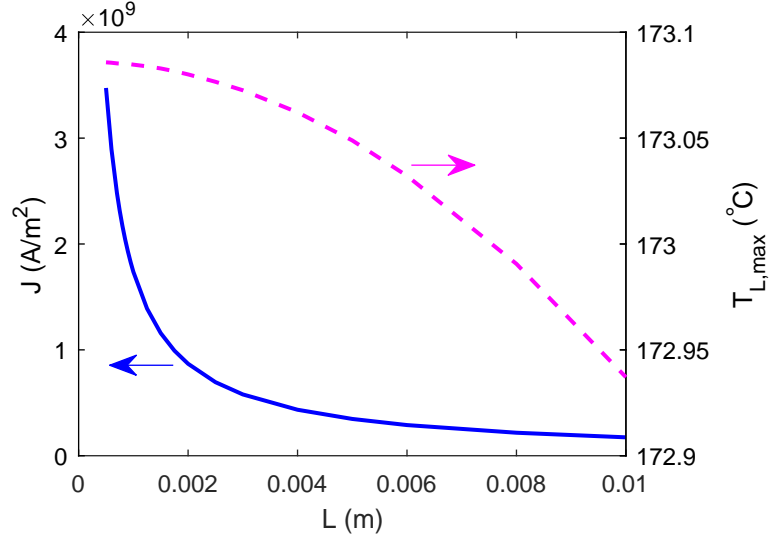
Figure 3.15: Parametric study based on *Rod length*. Parameter values: $V_{app} = 1.0$ V and $D = 0.5 \times 10^{-3}$ m.

3.5.7 Nondimensional analysis

Equations (3.19) are nondimensionalized using the following parameter definitions: $V^* = V/V_{app}$, $n_e^* = n_e/n_{th,ref}$, $n_h^* = n_h/n_{th,ref}$, $x^* = x/L$, and $T_L^* = T_L/T_\infty$, and re-written as follows:

$$J^* = \frac{\mu_{ave}(T_L^*)}{\mu_{ave,ref}} \frac{n_{th}(T_L^*)}{n_{th,ref}} E^*(x^*), \tag{3.21a}$$

$$0 = \frac{d}{dx^*}\left(\frac{k_L(T_L)}{k_{L,ref}}\frac{dT_L^*(x^*)}{dx^*}\right) + \frac{1}{\beta}J^*E^*(x^*)$$
$$- \frac{\gamma}{\beta}\frac{h_{Tot}(T_L^*)}{h_{Tot,ref}}\left[T_L^*(x^*) - 1\right], \tag{3.21b}$$

$$E^*(x^*) = -\frac{dV^*(x^*)}{dx^*}, \tag{3.21c}$$

$$\frac{d^2V^*(x^*)}{dx^{*2}} = -\zeta(n_h^*(x^*) - n_e^*(x^*)), \tag{3.21d}$$

where, $\zeta = eL^2 n_{th,ref}/V_{app}\epsilon_r\epsilon_0$, $\beta = k_{L,ref}T_\infty/J_0 V_{app}L$, $\gamma = 4h_{Tot,ref}T_\infty L/J_0 V_{app}D$, $J^* = J/J_0$, and $J_0 = 2e\mu_{ave,ref}n_{th,ref}V_{app}/L$.

49
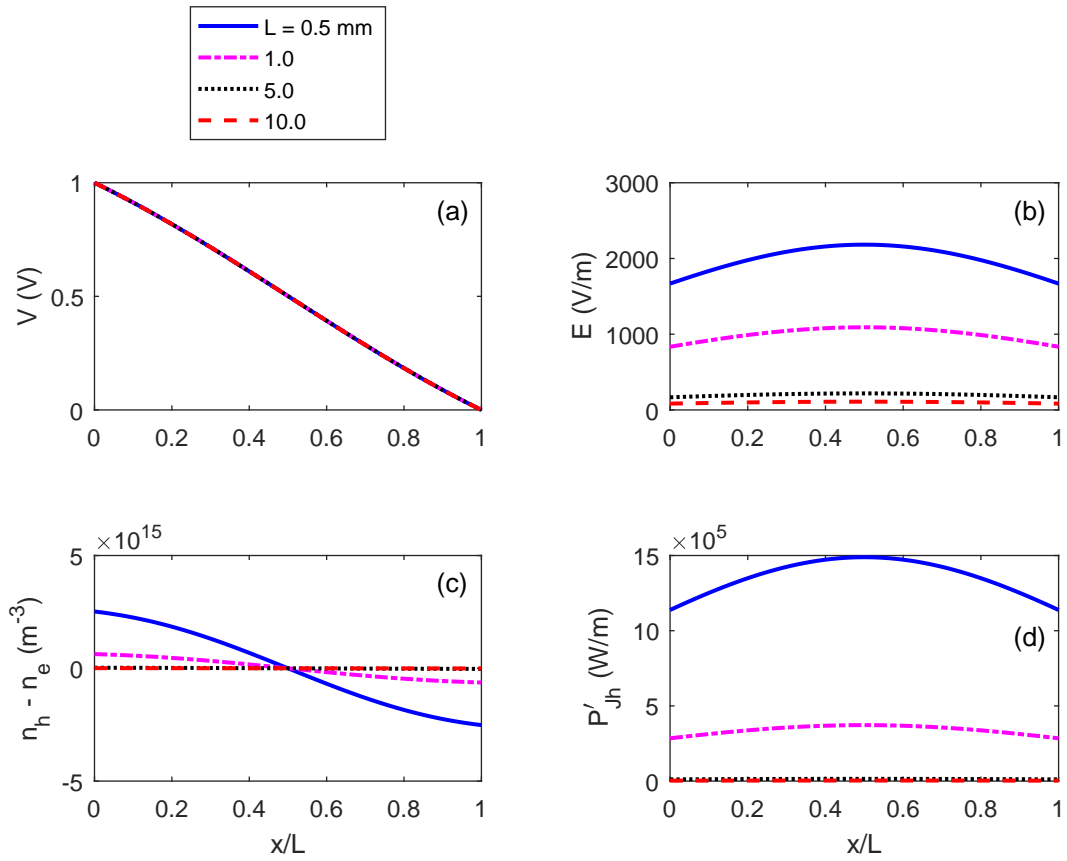
Figure 3.16: Parametric study based on *Rod length*. Parameter values: $V_{app} = 1.0$ V and $D = 0.5 \times 10^{-3}$ m.
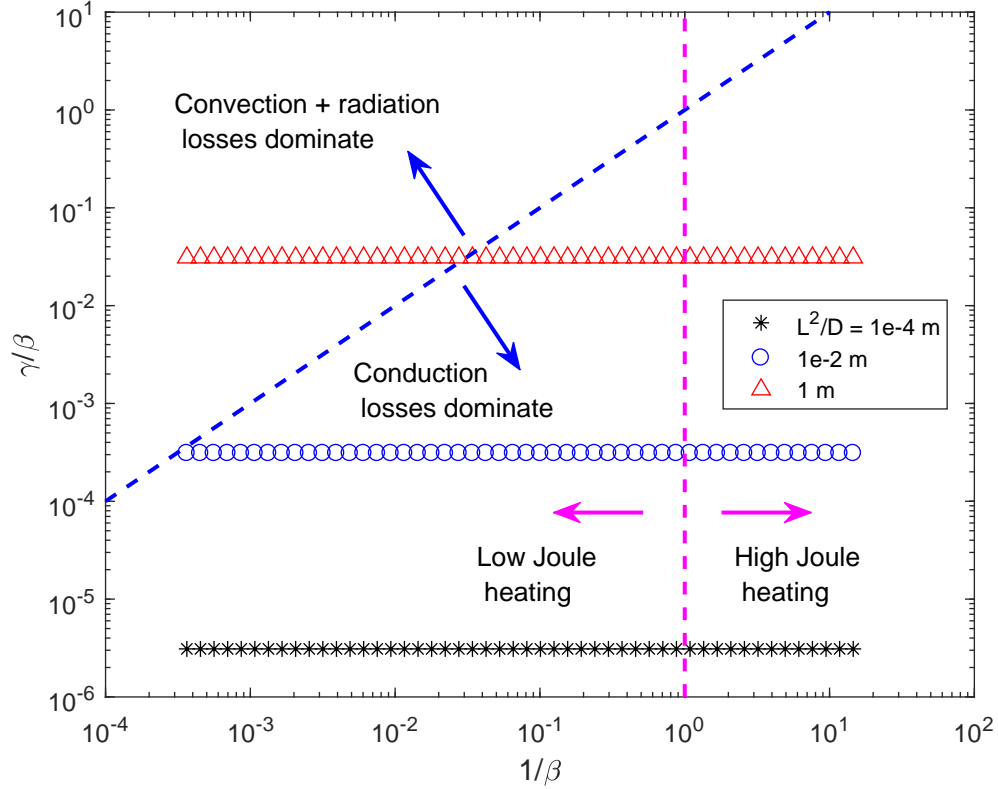
Figure 3.17: Comparison of the magnitude of the nondimensional coefficients in the energy equation (3.21b).

Equations (3.21), being in nondimensional form, allow for a quick comparison of the orders of magnitude of the various terms involved. Let us focus in the heat equation (3.21b) for instance. The diffusion term has a coefficient of order one, the Joule heating term has a coefficient equal to $1/\beta$, and the convection plus radiation losses term has a coefficient of γ/β. Both coefficients, $1/\beta$ and γ/β, can be re-written as follows:

$$\frac{1}{\beta} = \frac{J_0 E_0 L^2}{k_{L,ref} T_\infty},$$ (3.22)

and

$$\frac{\gamma}{\beta} = \frac{4 h_{Tot,ref} L^2}{k_{L,ref} D},$$ (3.23)

which resembles the well-known Biot number, $\mathrm{Bi} = hD/k$. A comparison of the three terms can be made by varying the value of $1/\beta$ through the applied voltage, and the value of γ/β through the length and diameter, keeping the heat transfer coefficient fixed. The results are shown in Fig. 3.17. Above the diagonal blue dashed line, $\gamma/\beta > 1/\beta$, which means that the convection and radiation losses dominate, while below the line, $\gamma/\beta < 1/\beta$, which means that conduction losses through the boundaries

51

dominate. However, the vertical magenta dashed line separates the regions where Joule heating is low and high, left and right, respectively. In other words, to the left of the vertical magenta line, there is low amounts of Joule heating to be removed regardless of which losses dominate. To the right of the vertical magenta line and to the bottom of the diagonal blue curve, most of the Joule heating will be removed by heat conduction through the boundaries. Lastly, to the right of the vertical magenta dashed line and above the blue dashed line most of the Joule heating will be removed by convection plus radiation losses. Moreover, the intersection of both dashed lines means that all three coefficients have an order of magnitude of one, which means that all three terms are equally important. Consequently, three different ratios of L^2/D were used, representing the range of interest in our studies. The three cases are represented by the different symbols in the same figure. It can be seen that all three cases fall well below the intersection of the dashed lines. Two major conclusions can be drawn. First, Joule heating is significant for values of $1/\beta \gtrsim 1$, which corresponds to an applied voltage greater than about 0.54 Volts. Second, all our cases fall well below the intersection point of the dashed lines. This means that heat losses by convection plus radiation are negligible for all our cases when high Joule heating is present. In order for convection plus radiation losses to become significant for the high Joule heating cases, the ratio of L^2/D has to be about 100 m or larger.

To further explore the extent of the effect of the convection and radiation losses, the ratio of h_{Tot}/D was varied over more than three orders of magnitude. It was found that the difference in the maximum lattice temperature reached was less than about 1 °C. In addition, the current density was only affected in the fourth significant digit. Thus, again, convection and radiation losses are insignificant for all operating conditions considered in this study.

3.5.8 Scaling analysis

Using scaling analysis, and safely ignoring the convection term, the energy equation (3.19b) can be written as follows:

$$\frac{k_L \Delta T_L}{L^2} \sim JE, \tag{3.24}$$

or by taking $\Delta T_L \sim T_{L,max}$, $k_L \sim k_L(T_{L,max})$, and $JE \sim P'''_{Jh,max}$, we get

$$k_L(T_{L,max})T_{L,max} \sim P'''_{Jh,max}L^2. \tag{3.25}$$

The order of magnitude of the two terms can be compared for a given range of applied voltages, similarly as done in Subsection 3.5.7. Notice that $P'''_{Jh,max}L^2/ k_L(T_{L,max})T_{L,max} \equiv 1/\beta$, evaluated at $T_{L,max}$ instead of T_∞. The ratio of these two quantities may be seen as the efficiency at which the input energy, i.e., electrical current, is converted into heat, i.e., high temperature. Figure 3.18 presents the dependency of this ratio vs. applied voltage. It can be seen that as the applied voltage increases, the 'efficiency' of heating the material increases. Rather than following a straight line, the efficiency increases in a non-linear fashion. This is due to the

fact that because the mobility decreases with temperature, so does the conductivity, which in turn means the current density saturates at higher temperatures, and thus it affects this ratio. As explained in Subsection 3.5.7, the Joule heating effects are usually stronger at applied voltages larger than about 0.5 Volts, as can also be seen in Fig. 3.18.
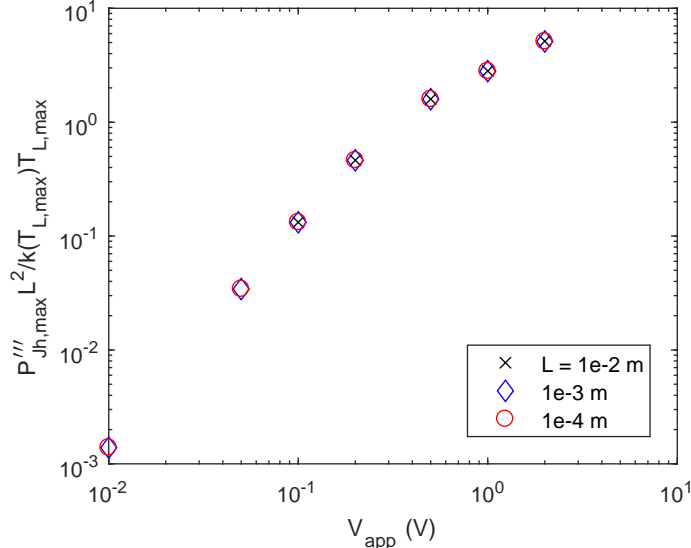
Figure 3.18: Comparison of the ratio of Joule heating over thermal energy vs. length and applied voltage.

The results just described can also be reached by plotting the ratio of the heat losses at the boundaries over the Joule heating, as can be seen in Fig. 3.19. The ratio is defined as $|q''|/P'''_{Jh,max}L$, where $|q''| = k_L dT_L/dx$, and k_L was evaluated at the mid point of the one sided second order finite difference. Also, it is observed that the total heat loss at the boundaries is $2|q''|$. It can be readily seen in Fig. 3.19 that only for values of applied voltage of 0.5 Volts and higher, the heat losses at the boundaries cannot dissipate the Joule heating generated, and the ratio decreases very sharply. In addition, the ratio is smaller for larger values of L, thus reaching the same conclusions as in the previous paragraph.

Lastly, applying scaling to Eq. (3.19d) the following expression can be obtained:

$$\frac{V_{app}}{L^2} \sim \frac{e}{\epsilon_r \epsilon_0} \max|n_h - n_e|, \tag{3.26}$$

thus, $V_{app} \propto \max|n_h - n_e|L^2$. Equation (3.26) also resembles the definition of ζ from Subsection 3.5.7. Using this relationship, the dependency of the maximum difference between holes and electrons was plotted vs. the applied voltage shown in Fig. 3.20. As the applied voltage is increased, the maximum difference between holes and electrons increases in a non-linear fashion due to temperature-dependent properties, especially the mobility.

53
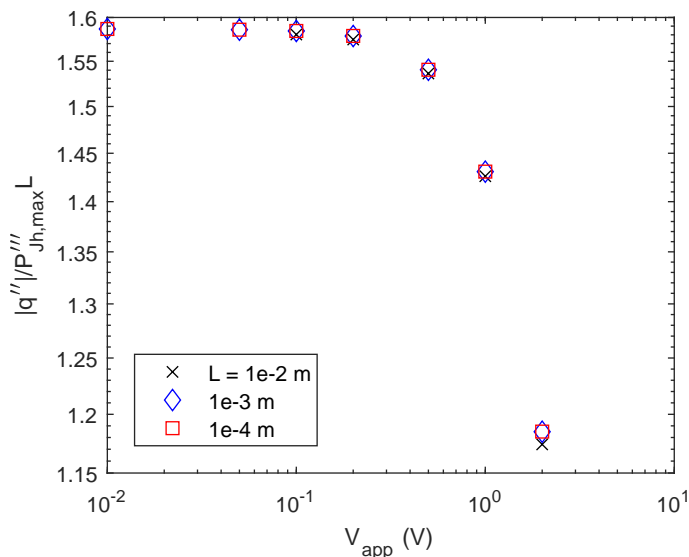
Figure 3.19: Comparison of the ratio of heat losses over Joule heating vs. length and applied voltage.

As a summary, these parametric studies, under the range of conditions analyzed here, show that there is a very small dependency of lattice temperature with respect to rod diameter, length, and heat transfer coefficient. However, an increase in applied voltage generates a significant rise in temperature. Therefore, in order to keep the rods at a certain temperature, the voltage has to be carefully controlled to avoid overheating of the rods. On the contrary, if one desires to heat up the rods quickly, relatively large values of applied voltage should be used.

3.5.9 Application of Joule heating as an efficient method of thermochemical decomposition of carbon-based materials

Joule heating can be utilized as an enhancement of thermochemical conversion processes such as pyrolysis and gasification, which tend to produce biochar, a carbon-rich material, as a byproduct. As discussed in Subsections 3.5.4 through 3.5.6, the combination of large Joule heating with low heat losses produces a sharp temperature rise in the rods. Although in conventional semiconductors and graphene-based semiconductors high temperatures are avoided, high temperatures are desired in carbonization processes, and therefore, Joule heating may be used as to enhance these processes. It was shown in Fig. 3.12 that as the applied voltage is increased the total current density tends to reach a saturation value, while the maximum lattice temperature increases sharply with higher applied voltages. For instance, comparing the total power, $P = V_{app}JA_c$, used in cases *I.B* and *II* described in Subsection 3.5.4, $P = 137$ Watts for *Case I.B*, while $P = 190$ Watts for *Case II*. Therefore, an increase in power of 39% raised the maximum lattice temperature from 173 °C to nearly 800
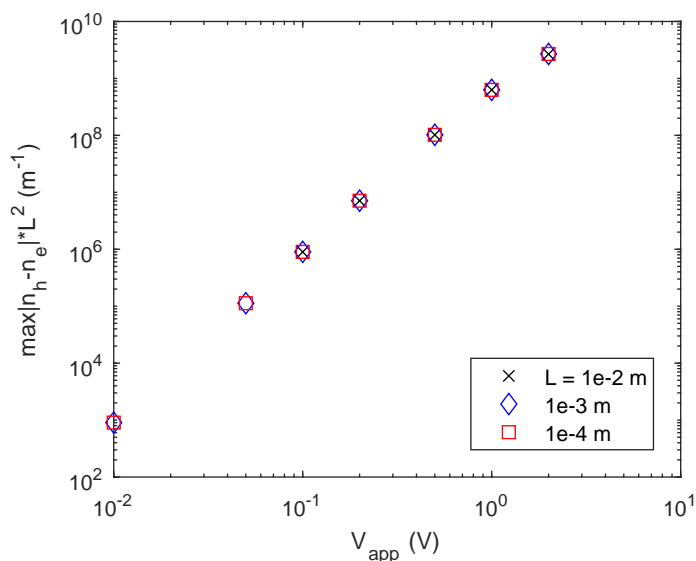
Figure 3.20: Dependency of the maximum difference of holes and electrons vs. length and applied voltage.

°C. No thermochemical conversion occurs in *Case I.B* but with a modest increase in power, temperatures suitable for carbonization can be reached. The model developed in this work can be utilized as a first approximation of the behavior of graphitic materials in the presence of Joule heating.

3.6 Conclusions

A one-dimensional steady-state drift-diffusion thermal-electric model has been developed to determine the difference between hole and electron densities, and to simulate charge and heat transport in rods of intrinsic pyrolytic graphite. Although the electron, hole, and thermal densities are nearly equal to each other for intrinsic pyrolytic graphite, there exists a small difference among them, i.e., $n_h(x) \approx n_e(x) \approx n_{th}(T_L)$, and the maximum absolute difference, $\max|n_h(x) - n_e(x)| \ll n_{th}(T_L)$. It was found that the difference between hole and electron densities, $n_h(x) - n_e(x)$, varies along the rod and that the maximum absolute difference occurs where the gradient of the electric field is largest, while the difference is zero at the midpoint along the rod. It was also determined that there are more holes than electrons on the half corresponding to the positive polarity of voltage, while there are more electrons on the half near the grounded end. Furthermore, when the applied voltage was negative, the variation of the difference between holes and electrons was inverted. It was further determined that the maximum absolute difference between holes and electrons, given a dielectric constant, decreases with increasing ratio of length over electric field. Lastly, for our arbitrary problem of interest with $L = 10^{-2}$ m and

applied voltage $V_{app} = 1.0$ V, $\max|n_h(x) - n_e(x)|$ is of the order of 10^{13} m^{-3}, which is orders of magnitude lower than the intrinsic density.

In addition to the previous results, the model was used to investigate other Joule heating effects for intrinsic pyrolytic graphite rods. The distribution of voltage, electric field, electron and hole velocities, diffusion and total current densities, net generation rate of electrons and holes, as well as, lattice temperature, Joule heating power, and heat losses were determined. Additional results were obtained by evaluating the mobility, thermal conductivity, and/or thermal density at the rod's average lattice temperature rather than at the local temperature. These results were less accurate than when the properties are evaluated at the local temperature, and in some cases convergence was not achieved.

Lastly, parametric analyses for voltage, diameter, length, and heat transfer coefficient were carried out for various operating conditions, followed by nondimensional and scale analyses. It was found that while the diameter, length and overall heat transfer coefficient values have a negligible effect on the maximum steady-state lattice temperature, the applied voltage affected the lattice temperature significantly. The results also showed that the total current density increases with applied voltage. In addition, the total current density tends to saturate at higher voltages, while the lattice temperature increases almost at an exponential rate. It was also discussed that the Joule heating effect can be utilized to enhance carbonization processes.

Chapter 4

HYDRODYNAMIC MODEL

4.1 Introduction

The drift-diffusion model used in Chapter 3 was used to analyze charge and Joule heat transport in graphite rods. The drift-diffusion model is a highly simplified version of the hydrodynamic model from Eqs. (2.4); however, it was solved successfully and yielded a significant amount of results and physical insights. In this chapter, the goal is to develop a more complete version of the hydrodynamic model along with a stable numerical scheme – in this dissertation a complete hydrodynamic model refers to Eqs. (2.4). The purpose for these developments – to be done in the near future – is to use the hydrodynamic model to analyze charge and Joule heat transport in a graphite rod or device. Moreover, the model might be applicable in the analysis of multilayer graphene devices, which are being highly investigated in the present time.

Though, the transition from the drift-diffusion model to the hydrodynamic model may seem trivial, this transition is not as straightforward. Because the hydrodynamic model is composed of highly-coupled nonlinear partial differential equations, they have various sources of instabilities [74, 105]. In addition, hydrodynamic models have been used extensively to analyze charge and heat transport in conventional semiconductors, such as GaAs and Si, but they have never been used to analyze charge/heat transport in graphite. As a consequence, the adaptation of the hydrodynamic model and the development of the numerical scheme to graphite need to be done with extreme care.

The hydrodynamic model used in this dissertation, Eqs. (2.4), was developed based on similar models in the literature, as has been stated in previous chapters. Starting from Eqs. (2.4), Eqs. (4.1) below are obtained by making certain simplifications based on physical characteristics of the system. The complete derivation of the hydrodynamic model in Eqs. (4.1) is given in Appendix A. Once a suitable hydrodynamic model for graphite (and perhaps multilayer graphene) has been developed, the next step consists of performing a detailed analysis based on the nondimensional

equations, Eqs. (4.1). This analysis will help determine a proper range of operating conditions and the importance of each term on the equations. In addition, it will help determine (a) proper characteristic time(s) and proper grid spacing to improve the stability of the numerical scheme. This analysis is presented in Sec. 4.5.

Subsequently, a numerical scheme is developed for the transient model in Sec. 4.6. The numerical scheme adopted is also based on similar approaches found in the literature. The numerical scheme uses a fourth-order Runge-Kutta method to integrate in time, and second order finite difference approximations in space. The numerical scheme is then validated by solving a similar problem found in the literature in Subsection 4.6.1 and Appendix B. This validation is very strong because the model solved in that article was steady-state and the numerical solution was based on perturbation methods, while we used our transient numerical scheme and finite difference method to extend the range of validity of the results. Thus, these two steps complete the main goals of this chapter.

The next steps are needed to be able to apply the hydrodynamic model to graphite. Though the boundary conditions for electron and hole densities are typically well known when using conventional semiconductors, these are not so trivial when using intrinsic (not doped) graphite, see Subsection 4.6.2. Thus, determining these boundary conditions is a critical step. In addition, the net generation rates of electrons and holes need to be determined. To aid in this front, two steady-state versions of the transient model are developed. In one version, the net generation rates of electrons and holes are canceled out, and the mass action law is invoked in order to have a single carrier density as the only unknown variable. Thus, it is easier to explore and determine the boundary conditions for graphite. This analysis is presented in Subsection 4.6.4. The second version is utilized to ensure that the equations are stable. This analysis is presented in Subsection 4.6.5.

4.2   Description Of The Problem

In this chapter, a similar problem to that described in Chapter 3 is considered, see Fig. 4.1. The hydrodynamic model is developed to describe the charge carrier and Joule heat transport in a graphite rod of length L and diameter D, with $L \geq D$. A DC voltage, V_{app}, is applied on the left end of the rod while the right end is grounded. Due to the electric field, charge carriers, i.e., electrons and holes, move across the rod producing a current density, which generates Joule heating on the rod. Consequently, due to Joule heating, the lattice temperature rises and results in thermal generation of electrons and holes. Both ends of the rod have a fixed temperature equal to T_∞. The rod is exposed to generic heat losses to the surroundings. The heat losses might be due to convection and radiation to the environment, or to conduction losses to a substrate in the case of a semiconductor device.

4.3   Governing Equations

The governing equations for the hydrodynamic model are explained in detail in Sec. 2.3 and Appendix A, where they have also been nondimensionalized and

At the top of the schematic:

$T_L^*(x^*)$ q_l^*

Graphite rod D

$\mapsto x^*$

0 L

Left boundary:
$$V^* = V_{app}$$
$$T_L^* = T_\infty$$
$$n_e^* = n_{e,lb}^*$$
$$n_h^* = n_{h,lb}^*$$

Right boundary:
$$V^* = 0$$
$$T_L^* = T_\infty$$
$$n_e^* = n_{e,rb}^*$$
$$n_h^* = n_{h,rb}^*$$
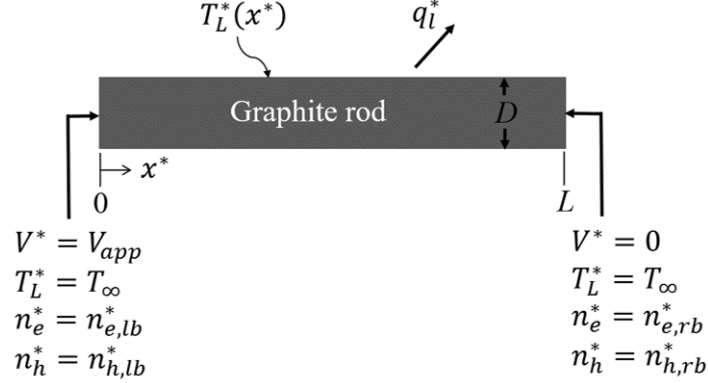
Figure 4.1: Schematic: Graphite rod under an applied voltage with generic heat losses, and with boundary conditions shown.

simplified. Hence, in this section the nondimensional hydrodynamic model is given with few details.

The general hydrodynamic model used in this chapter is referred to as a *transient one-dimensional two-temperature two-carrier hydrodynamic model*, where two-temperature refers to one lattice temperature and one carrier temperature, and two-carrier refers to the presence of both electrons and holes. Having a single carrier temperature means that the electrons and holes are in thermal equilibrium, thus, a single carrier temperature. A detailed discussion about this is given in Sec. A.3.

The parameters used to nondimensionalize the equations are the following: $x^* = x/L$, $V^* = V/V_0$, $n_e^* = n_e/N_0$, $n_h^* = n_h/N_0$, $u_e^* = u_e/U$, $u_h^* = u_h/U$, $T_L^* = T_L/T_0$, $T_c^* = T_c/T_0$, and $t^* = tU/L$, with V_0 a reference voltage, N_0 a reference density, and T_0 a reference temperature. Where, x^* is the space variable, t^* is the time, $V^*(x^*, t^*)$ is the electrostatic potential, $n_e^*(x^*, t^*)$ is the electron density, $n_h^*(x^*, t^*)$ is the hole density, $u_e^*(x^*, t^*)$ is the electron velocity, $u_h^*(x^*, t^*)$ is the hole velocity, T_c^* is the (constant) carrier temperature, and $T_L^*(x^*, t^*)$ is the lattice temperature. The asterisk denotes the nondimensional parameters.

The nondimensional equations of the hydrodynamic model include Gauss's law in Eq. (4.1a), charge conservation equations for electrons and holes in Eqs. (4.1b) and (4.1c), momentum conservation equations for electrons and holes in Eqs. (4.1d) and (4.1e), and energy conservation for the lattice in (4.1f). The system of equations is

$$\frac{\partial^2 V^*}{\partial x^{*2}} = -\zeta \left(n_h^* - n_e^* \right), \tag{4.1a}$$

$$\frac{\partial n_e^*}{\partial t^*} + \frac{\partial (u_e^* n_e^*)}{\partial x^*} = G_{e,net}^*, \tag{4.1b}$$

$$\frac{\partial n_h^*}{\partial t^*} + \frac{\partial (u_h^* n_h^*)}{\partial x^*} = G_{h,net}^*, \tag{4.1c}$$

$$u_e^* = \frac{\mu_e}{\mu_{e,ref}} \left[\frac{\partial V^*}{\partial x^*} - \beta \frac{1}{n_e^*} \frac{\partial n_e^*}{\partial x^*} \right], \tag{4.1d}$$

$$u_h^* = -\frac{\mu_h}{\mu_{e,ref}} \left[\frac{\partial V^*}{\partial x^*} + \beta \frac{1}{n_h^*} \frac{\partial n_h^*}{\partial x^*} \right], \tag{4.1e}$$

$$\psi_0 \frac{C_{L,v}}{C_{L,v,ref}} \frac{\partial T_L^*}{\partial t^*} = \psi_1 \frac{\partial}{\partial x^*} \left(\frac{k_L}{k_{L,ref}} \frac{\partial T_L^*}{\partial x^*} \right) - \beta \left(n_e^* \frac{\partial u_e^*}{\partial x^*} + m_r n_h^* \frac{\partial u_h^*}{\partial x^*} \right)$$
$$+ \left(1 - \frac{1}{2}\nu \right) \left[\frac{\tau_{M,e,ref}}{\tau_{M,e}} n_e^* u_e^{*2} + \frac{\tau_{M,e,ref}}{\tau_{M,h}} n_h^* u_h^{*2} \right] + q_l^{*\prime\prime\prime}. \tag{4.1f}$$

where $\zeta = eL^2 N_0/\epsilon_r \epsilon_0 V_0$, $\beta = k_B T_c/eV_0$, $m_r = m_e^\star/m_h^\star$, $\nu = \tau_{M,e}/\tau_{E,e} = \tau_{M,h}/\tau_{E,h}$, $\psi_0 = \tau_{M,e,ref} C_{L,v,ref} T_0/m_e^\star N_0 UL$, and $\psi_1 = \tau_{M,e,ref} k_{L,ref} T_0/m_e^\star N_0 U^2 L^2$. In addition, $G_{e,net}^* = G_{e,net} L/N_0 U$ is the net generation rate of electrons, $G_{h,net}^* = G_{h,net} L/N_0 U$ is the net generation rate of holes, $q_l^{*\prime\prime\prime} = q_l^{\prime\prime\prime} \tau_{M,e}/N_0 m_e^\star U^2$ is the generic heat losses term, and $U = eV_0 \tau_{M,e,ref}/m_e^\star L = \mu_{e,ref} V_0/L$ is the maximum average electron velocity.

The physical parameters are the elementary charge, e, the relative permittivity of the material, ϵ_r, the permittivity of free space, ϵ_0, the effective electron mass, $m_e^\star$, the effective hole mass, $m_h^\star$, Boltzmann's constant, k_B, the momentum relaxation time for electrons, $\tau_{M,e}$, the momentum relaxation time for holes, $\tau_{M,h}$, the energy relaxation time for electrons, $\tau_{E,e}$, the energy relaxation time for holes, $\tau_{E,h}$, the thermal conductivity of electrons, k_e, the thermal conductivity of holes, k_h, the thermal conductivity of the lattice, k_L, and the volumetric heat capacity of the lattice $C_{L,v}$.

Note that the transient and convective terms on the momentum equations for electrons and holes, Eqs. (4.1d) and (4.1e), have been discarded. This is because the Reynolds number is presumed to be small due significant scattering events. The equivalent physics in fluid dynamics would be a viscous flow, for which the inertia terms may be safely neglected [50, 57, 59, 106] – in this case, based on our nondimensional parameters, the transient terms have also been safely neglected. In a semiconductor, $\mathrm{Re} = U\tau_{M,e,ref}/L$, which is the Reynolds number for the electron cloud [50, 57, 59, 106]. Please refer to Secs. A.4 and A.5 for more details. Also, note that in the definition of ν it was assumed that the ratio of momentum relaxation time to energy relaxation time was equal for both electrons and holes. More details about this assumption are given in Sec. A.7.

In order to make the solution of Eqs. (4.1) more tractable, the continuity and momentum equations for electrons and holes are combined and the equations are re-written as follows:

$$\frac{\partial n_e^*}{\partial t^*} = -\frac{1}{\mu_{e,ref}}\frac{\partial}{\partial x^*}\left(\mu_e n_e^* \frac{\partial V^*}{\partial x^*}\right) + \frac{\beta}{\mu_{e,ref}}\frac{\partial}{\partial x^*}\left(\mu_e \frac{\partial n_e^*}{\partial x^*}\right) + G_{net}^*, \qquad (4.2a)$$

$$\frac{\partial n_h^*}{\partial t^*} = \frac{1}{\mu_{e,ref}}\frac{\partial}{\partial x^*}\left(\mu_h n_h^* \frac{\partial V^*}{\partial x^*}\right) + \frac{\beta}{\mu_{e,ref}}\frac{\partial}{\partial x^*}\left(\mu_h \frac{\partial n_h^*}{\partial x^*}\right) + G_{net}^*, \qquad (4.2b)$$

where G_{net}^* represents both the net generation of electrons and holes; in intrinsic materials, the generation of electrons and holes is equal. This is explained as follows: as an electron gains sufficient energy to 'jump' from the valence band to the conduction band, a hole is left in the valence band. On the other hand, when an electron loses enough energy it decays to the valence band, where it recombines with a hole.

Note that the electron and hole momentum (velocity) equations, Eqs. (4.1d) and (4.1e), are still included explicitly. However, the electron and hole velocities have become secondary variables. They were kept in order to avoid writing an extra long energy equation (4.1f).

4.4   Thermophysical Properties Of Pyrolytic Graphite

A few of the thermophysical properties of pyrolytic graphite have been given in Chapter 3. The temperature-dependent thermal density, mobility, and thermal conductivity are given in Eqs. (3.8), (3.11), and (3.12), respectively. Studies performed at ambient and lower temperatures show that while the thermal conductivity of commercial and pyrolytic graphites can be very different in magnitude, the specific heat is within the same order of magnitude [107]. It will be assumed here that this similarity holds above room temperature. Thus, the specific heat of pyrolytic graphite above room temperature will be assumed to be equal to that of POCO graphite. The temperature dependence of the specific heat from ambient temperature to 3200 K is described by the following expression

$$c_p(T_L) = 4184(0.44391 + 0.30795 \times 10^{-4} T_L - 0.61257 \times 10^5 T_L^{-2}$$
$$+ 0.10795 \times 10^8 T_L^{-3}), \qquad (4.3)$$

which is accurate to within 1.5% of the experimental value [88]. The mass density of commercial polycrystalline graphites is typically lower than 80 percent of the theoretical density, 2260 kg/m^3 [88]. The mass density of pyrolytic graphites on the other hand tends to virtually reach the theoretical value upon intense heat treatment [88, 107]. In light of this information, a mass density of 2200 kg/m^3 will be used in this dissertation. For this initial analysis, based on the fact that the electron and hole mobilities are almost equal, they have actually been assumed to be equal. Also the effective masses have been assumed to be equal. A summary of the properties at room temperature is given in Table 4.1.

As a final note, it is reiterated here that the properties are temperature-dependent. While the mobility and thermal conductivity vary greatly with temperature, the thermal density and the specific heat do not vary as much. However,

Table 4.1: Properties of pyrolytic graphite at various temperatures [80, 88, 100, 101].

Property	Temperature (K) 298 Value	398 Value	498 Value	Units
ϵ_r	13			
$\mu_e = \mu_{ave}$	1.02	0.65	0.46	$m^2/(V\ s)$
$\mu_h = \mu_{ave}$	1.02	0.65	0.46	$m^2/(V\ s)$
$m_e^\star = m_c^\star$	$0.0125m_0$			kg
$m_h^\star = m_c^\star$	$0.0125m_0$			kg
$\tau_M = \mu_{ave}m_c^\star/e$	7.3×10^{-14}	4.6×10^{-14}	3.3×10^{-14}	s
$\tau_E = 50\tau_M$	7.3×10^{-12}	4.6×10^{-12}	3.3×10^{-12}	s
k_L	1911	1403	1104	$W/(m\ K)$
ρ_m	2200			kg/m^3
$C_{L,v}$	1.58×10^6	2.22×10^6	2.76×10^6	$J/(m^3\ K)$

the thermal conductivity and mobility play critical roles in the results, thus if the temperature increases significantly from room temperature, the results may also be significantly affected. The effect of using temperature (in)dependent properties was shown in Chapter 3. As such, the numerical schemes developed in this chapter will be applicable to devices with temperature-dependent material properties.

4.5 Nondimensional Analysis

The purpose of this section is to perform a thorough analysis of the non-dimensional equations to gain more physical insights from the hydrodynamic model. This will also allow us to determine the range of operating conditions that are suitable for the model.

Let us start by revisiting the voltage distribution in nondimensional form, Eq. (3.15), from Subsection 3.5.2. The equation is re-written here using the nondimensional coefficient ζ

$$V^*(x^*) = \zeta \max|n_h^*(x^*) - n_e^*(x^*)| \left[x^* - x^{*2}\right] + [1 - x^*], \qquad (4.4)$$

This equation was obtained through integration of Gauss' Law by considering the maximum absolute value of the difference between electrons and holes; the results are shown in Fig. 3.3. The voltage distribution is expected to be nearly linear, which requires the quadratic term to be of order one, as is the linear term. Since ζ is proportional to $\max|n_h^*(x^*) - n_e^*(x^*)|$, as ζ decreases $\max|n_h^*(x^*) - n_e^*(x^*)|$ increases. The development of hydrodynamic models arose based on the need to analyze submicrometer semiconductor devices. Nonetheless, the range of lengths considered here spans from 100 to 0.1 micrometers in order to better capture the effect of the length.

In addition, though the length of the devices became smaller than a micrometer, the voltage has remained constant at 1 Volt, thus yielding electric fields of 10^6 V/m or higher. Lastly, it has been reported that smaller values of ζ (smaller lengths and/or higher voltages) make the equations less stable [105].

Three different lengths are considered, which are given in Table 4.2 – in addition to other system parameters. The nondimensional coefficient ζ decreases with length since the voltage and other parameters are fixed. Consider $L = 1.0 \times 10^{-6}$ m, for which $\zeta = 2.78 \times 10^4$, see Table 4.3. This means that the value of $\max|n_h^*(x^*) - n_e^*(x^*)|$ needs to be close to 10^{-4} to keep the quadratic term near a value of 1. Consequently, the dimensional value, after multiplying by N_0, becomes about 2×10^{21} m^{-3}. This value is significantly larger than the value 10^{13} m^{-3} obtained for a one-centimeter-long rod in Chapter 3.

The coefficient β is considered next. This nondimensional coefficient depends on the carrier energy (temperature) and on the characteristic voltage, V_0, but it is independent of length. Since V_0 is fixed, β increases with carrier temperature T_c. A value of $T_c = 3000$ K has been chosen as a maximum foreseeable carrier temperature [50, 59], and it results in $\beta = 2.59 \times 10^{-1}$. On the other hand, in the drift-diffusion model in Chapter 3, β was about one order of magnitude lower because the carriers were considered to be in thermal equilibrium with the lattice energy, that is, $T_c = T_L$. Since the coefficient was smaller, it was safer to discard the diffusion terms based on the nondimensional analysis. Based on the momentum equations, Eqs. (4.1d) and (4.1e), the only other term inside the square brackets is the gradient of the voltage (drift term), which has a coefficient of one. Thus, the drift term has a coefficient nearly 5 times larger than the diffusion term regardless of the length. Though, the diffusion terms are not too small, so they cannot be neglected right away. The diffusion terms will need to be included in the simulations and only after obtaining a solution can they be compared to the drift term more thoroughly. This can be achieved by calculating the gradient of the voltage and the gradient of the densities. Once the derivatives are known, both terms can be fully evaluated. This analysis can also be applied to the energy equation, Eq. (4.1f). Lastly, early analysis using various steady-state versions of the hydrodynamic equations suggest that smaller values of β make the momentum equations less stable. This might happen because small values of β cause the main diagonal of the matrix to lose its dominance.

The next nondimensional number to be considered is the Reynolds number as it also relates to the momentum equations. The Reynolds number is a measure of the scattering rates, a smaller Reynolds number means more collisions and vise versa. The Reynolds number in semiconductors is based on the relaxation time times the velocity divided by the length. Based on these definitions the Reynolds number may also be defined as the ratio of the electron mean free path and the device length, i.e., Re= l_{e-e}/L [50], which corresponds to the Knudsen number. The definition of the electron mean free path is $l_{e-e} = U\tau_{M,e}$ [50, 108]. In the case of graphite, the hole mobility is similar to that of the electrons so the hole mean free path will

be very close to that of the electrons. The Reynolds number for three different lengths is given in Table 4.3. It is readily seen that Re is generally a small number; however, when $L = 0.1$ micrometer, Re= 7.45 at room temperature – meaning that l_{e-e} is slightly smaller than one micrometer. This result can be interpreted in various manners. For example, it means that L has become larger than l_{e-e}, for which scattering has decreased significantly, and ballistic transport has become more dominant than diffusion transport [57]. It also means that the inertia terms cannot be neglected and that the complete momentum equations should be used. However, the continuum assumption on which the hydrodynamic is based, breaks down, and the hydrodynamic model is no longer able to capture the carrier dynamics at this or smaller lengths. As a consequence, the hydrodynamic model cannot be used in devices smaller than about 1 micrometer when graphite properties are used despite the fact that hydrodynamic models were developed for the purpose of analyzing submicrometer devices. The main reason for which the Reynolds number is quite large at submicrometer sizes is due to the fact that the mobility of electrons for graphite at ambient temperature is about $1 \text{ m}^2/(\text{V s})$ [80], compared to $0.145 \text{ m}^2/(\text{V s})$ for Silicon [45].

For the first analysis the effective mass of electrons and holes, $m_e^\star$ and $m_h^\star$, will be assumed to be equal, based on the fact that they have similar values [80, 94, 95]. As consequence, their ratio, m_r is equal to 1. This in turn causes the relaxation times of electrons and holes to be equal to each other, see Table 4.1. The value of m_r affects the magnitude of the electron diffusivity relative to the hole diffusivity in the energy equation, Eq. (4.1f).

The dimensionless coefficient ν is the ratio of the momentum to the energy relaxation time. Since the electron and hole momentum relaxation times are approximated to be equal, so will be the energy relaxation times. Thus, the value of ν is equal for both electrons and holes, which was already assumed in the model considered in this chapter, see Sec. A.7. Since the values for the energy relaxation times have not been found yet, their effect will be analyzed systematically through ν. In fact, a quick analysis was already performed in Appendix A. It was found that ν modulates the value of the Joule heating. As ν increases, the fraction of Joule heating affecting the system decreases, and vise versa. For example, when $\nu = 1$, only 50 percent of the energy is dissipated as Joule heating, and when $\nu = 0.02$, 99 percent of the energy will be dissipated as Joule heating into the system.

The energy equation, Eq. (4.1f), and its dimensionless coefficients are considered next. First the steady-state terms will be discussed, but the genetic term for heat losses, $q_l^{*\prime\prime\prime}$, will be excluded. The importance of each of the steady-state terms can be quickly assessed by evaluating the magnitude of the dimensionless coefficients. The three coefficients ψ_1, β, and ν are independent of L, while ψ_1 and β decrease with V_0. Because V_0, which is equal to 1 V, is the characteristic voltage of the system, it is kept constant. Thus, all three coefficients remain constant for the three different lengths considered here, see Table 4.3. As a summary, heat diffusion is the leading term with a coefficient of $\psi_1 = 1.75$, followed by the Joule heating

term with the coefficient $(1 - \nu/2) = 0.99$, and the last term being diffusion, whose coefficient is $\beta = 0.259$. Based on these coefficients, the conclusion is that the Joule heat will be successfully diffused by the lattice (phonons) to the boundaries, and only a small portion will be transported by the diffusion of the carriers. The heat diffusion coefficient ψ_1 is large mainly because the thermal conductivity of graphite is large.

At this time the transient terms in Eqs. (4.1) will be discussed. The energy equation will be considered first to continue the discussion from the last paragraph. Comparing the coefficient ψ_0 to the steady-state coefficients, it is readily seen that ψ_0 is about 3 to 4 orders of magnitude larger. This means that the lattice temperature will take a long time to reach steady-state. In contrast, the electrons and holes reach steady-state quite fast, that is one of the reasons the transient terms on the momentum equations were discarded, for the electron and hole velocities change almost instantaneously. An equivalent explanation is as follows. The carrier (or electronic) dynamics are typically determined by the momentum relaxation time, which for graphite is $\tau_M = 7.3 \times 10^{-14}$ seconds. In contrast, the heat transport dynamics are driven by a thermal characteristic time $\tau_{th} = (D/4)^2/\alpha = (10^{-7}/4)^2/5.5 \times 10^{-7} = 1.1 \times 10^{-9}$ seconds. Thus, the electronic dynamics are about 10^5 times faster.

Table 4.2: Characteristic parameters of the system.

Parameter	Value	Value	Value	Units
L	1.0×10^{-7}	1.0×10^{-6}	1.0×10^{-4}	m
D	1.0×10^{-8}	1.0×10^{-7}	1.0×10^{-5}	m
N_0	2.0×10^{25}			m^{-3}
V_0	1.0			V
T_∞	298			K
T_c	3000			K
T_0	3000			K

4.6 Development And Testing Of Numerical Schemes

The end-goal of the analysis presented in this chapter is to aid in the solution of Eqs. (4.1) in their most general form using the properties of graphite. In addition to the understanding obtained from nondimensional analysis from the last section, it would be ideal to find an existing hydrodynamic model that is similar to this one, so that we could develop the numerical scheme and apply it to an already existing semiconductor problem. This comparison will help ensure that (1) the code is error-free, (2) the numerical scheme is stable, and (3) to better understand possible sources of instability and (4) determine suitable ranges of operation. Because graphite is very

Table 4.3: Dimensionless parameters (and velocity U) for various temperatures and lengths.

| | Length (m) | | |
| | 1.0×10^{-7} | 1.0×10^{-6} | 1.0×10^{-4} |
Parameter	Value	Value	Value
$T_L = 298$ K			
ζ	2.78×10^2	2.78×10^4	2.78×10^8
β	2.59×10^{-1}		
m_r	1.0		
ν	2.0×10^{-2}		
ψ_0	1.48×10^3		
ψ_1	1.75×10^0		
U	1.02×10^7 m/s	1.02×10^6 m/s	1.02×10^4 m/s
Re	7.45×10^0	7.45×10^{-2}	7.45×10^{-6}
$T_L = 398$ K			
ψ_0	2.08×10^3		
ψ_1	2.01×10^0		
U	6.53×10^6 m/s	6.53×10^5 m/s	6.53×10^3 m/s
Re	3.03×10^0	3.03×10^{-2}	3.03×10^{-6}
$T_L = 498$ K			
ψ_0	2.58×10^3		
ψ_1	2.24×10^0		
U	4.61×10^6 m/s	4.61×10^5 m/s	4.61×10^3 m/s
Re	1.51×10^0	1.51×10^{-2}	1.51×10^{-6}

different from conventional semiconductors, this step is crucial in the development of the numerical scheme.

The numerical scheme adopted is presented next. Equations (4.1) and (4.2) were discretized using second order finite differences as follows:

$$\frac{V_{k+1} - 2V_k + V_{k-1}}{(\Delta x)^2} = -\alpha \left(n_{h,k} - n_{e,k} \right), \tag{4.5a}$$

$$\frac{\partial n_{e,k}}{\partial t} = -\frac{1}{\mu_{e,ref}\Delta x} \left[\mu_{e,k+1/2} n_{e,k+1/2} \frac{V_{k+1} - V_k}{\Delta x} - \mu_{e,k-1/2} n_{e,k-1/2} \frac{V_k - V_{k-1}}{\Delta x} \right]$$
$$+ \frac{\beta}{\mu_{e,ref}\Delta x} \left[\mu_{e,k+1/2} n_{e,k+1/2} \frac{1}{\Delta x} \ln\left(\frac{n_{e,k+1}}{n_{e,k}}\right) - \mu_{e,k-1/2} n_{e,k-1/2} \frac{1}{\Delta x} \ln\left(\frac{n_{e,k}}{n_{e,k-1}}\right) \right]$$
$$+ G_{net,k}, \tag{4.5b}$$

$$\frac{\partial n_{h,k}}{\partial t} = \frac{1}{\mu_{e,ref}\Delta x} \left[\mu_{h,k+1/2} n_{h,k+1/2} \frac{V_{k+1} - V_k}{\Delta x} - \mu_{h,k-1/2} n_{h,k-1/2} \frac{V_k - V_{k-1}}{\Delta x} \right]$$
$$+ \frac{\beta}{\mu_{e,ref}\Delta x} \left[\mu_{h,k+1/2} n_{h,k+1/2} \frac{1}{\Delta x} \ln\left(\frac{n_{h,k+1}}{n_{h,k}}\right) - \mu_{h,k-1/2} n_{h,k-1/2} \frac{1}{\Delta x} \ln\left(\frac{n_{h,k}}{n_{h,k-1}}\right) \right]$$
$$+ G_{net,k}, \tag{4.5c}$$

$$u_{e,k} = \frac{\mu_{e,k}}{\mu_{e,ref}} \left[\frac{V_{k+1} - V_k}{\Delta x} - \frac{\beta}{\Delta x} \ln\left(\frac{n_{e,k+1}}{n_{e,k}}\right) \right], \tag{4.5d}$$

$$u_{h,k} = -\frac{\mu_{h,k}}{\mu_{e,ref}} \left[\frac{V_{k+1} - V_k}{\Delta x} + \frac{\beta}{\Delta x} \ln\left(\frac{n_{h,k+1}}{n_{h,k}}\right) \right], \tag{4.5e}$$

$$\psi_0 \frac{C_{L,v}}{C_{L,v,ref}} \frac{\partial T_{L,k}}{\partial t} = \frac{\psi_1}{k_{L,ref}\Delta x} \left[k_{L,k+1/2} \frac{T_{L,k+1} - T_{L,k}}{\Delta x} - k_{L,k-1/2} \frac{T_{L,k} - T_{L,k-1}}{\Delta x} \right]$$
$$+ \left(1 - \frac{1}{2}\nu \right) \tau_{M,e,ref} \left[\frac{n_{e,k} u_{e,k}^2}{\tau_{M,e,k}} + \frac{n_{h,k} u_{h,k}^2}{\tau_{M,h,k}} \right]$$
$$- \beta \left[n_{e,k} \frac{u_{e,k+1} - u_{e,k}}{\Delta x} + m_r n_{h,k} \frac{u_{h,k+1} - u_{h,k}}{\Delta x} \right] + q_{l,k}''', \tag{4.5f}$$

where the index 'k' denotes the node location, and the logarithm was introduced in the diffusion terms – those containing the coefficient β. The use of the logarithm improves the numerical scheme when the gradient becomes very large [109]. In addition, the Debye length can be used as a starting point to determine an appropriate grid size [50]. The Debye length for an intrinsic semiconductor material is defined as follows [110, 111]:

$$L_D = \sqrt{\frac{2\epsilon_r \epsilon_0 k_B T}{e^2 n_{th}}}. \tag{4.6}$$

The Debye length for graphite at a temperature of 298 K is equal to 2.4 nanometers. The temporal evolution of the equations was computed using an explicit fourth order Runge-Kutta method. In the case of time integration, the charge and heat characteristic times will help determine an appropriate time step, as was discussed

in the last paragraph of Sec. 4.5. The Poisson equation, Eq. (4.5a) was solved at each time step using the Tri-Diagonal Matrix Algorithm (TDMA). The system of equations was solved in the same order as they are listed. In addition to the numerical schemes, grid independence tests need to be done, and a stable time step needs to be determined. Lastly, it is mentioned here that this numerical scheme was developed for temperature-dependent material properties.

4.6.1 Replication of results from Ref. [59].

The hydrodynamic model used in this chapter is similar to that used to study charge and energy transport in GaAs PN junctions [59]. This presents a great opportunity to use the numerical scheme developed in this chapter and ensure the code is error-free and that the numerical scheme is stable. Osses-Márquez and Calderón-Muñoz [59] solved their steady-state hydrodynamic model using perturbation methods, which are very different from the numerical scheme developed in this chapter. Upon applying this numerical scheme to their problem, their results were successfully replicated. A detailed discussion and a set of the results is presented in Appendix B.

4.6.2 Initial conditions, boundary conditions, and net generation rate

The appropriate initial conditions for the hydrodynamic model will be explored. However, based on the electric-thermal model from Chapter 5, the following initial boundary conditions will be explored first: $E^*(x^*, 0) = V_{app}/V_0$, $T_L^*(x^*, 0) = T_\infty/T_0$, $n_e^*(x^*, 0) = n_{th}/N_0$, and $n_h^*(x, 0) = n_{th}/N_0$.

The hydrodynamic model of Eqs. (4.1) requires 8 boundary conditions (BCs):

- 2 BCs for voltage

- 2 BCs for the lattice temperature

- 2 BCs for the electron density

- 2 BCs for the hole density

The boundary conditions for voltage are $V^*(0, t^*) = V_{app}/V_0$, and $V^*(L^*, t^*) = 0$, and for temperature are $T_L^*(0, t^*) = T_\infty/T_0$ and $T_L(L, t) = T_\infty/T_0$. The appropriate boundary conditions for electrons and holes are not known yet. Though, there are a number of options in the literature, the correct boundary conditions for this problem need to be determined. The boundary conditions are critical parameters because they significantly affect the physics inside the device.

In addition to the boundary condition, the net generation rate of electron and holes, G_{net}^*, is unknown. The effect of this parameter will be explored in the simulations.

4.6.3 Sample set of results with transient hydrodynamic model applied to graphite

A sample set of results using the transient hydrodynamic model applied to graphite rods is shown next. This is done only for the purpose of showing the capabilities and types of solutions of the model and numerical scheme; the results will not be explained here. The boundary conditions for voltage and temperature are as given in the last section. The boundary values for electrons and holes are extrapolated at each time step. The net generation rates were set to zero. Sample results for a rod with $L = 1.0 \times 10^{-6}$ m, $D = 1.0 \times 10^{-7}$ m, and $V_{app} = 1$ V are shown in Fig. 4.2, where $\Delta t^* = 1.0 \times 10^{-8}$, or $\Delta t = 9.77 \times 10^{-21}$ seconds, and 101 grid points were used. The arbitrary time shown is 3.66×10^{-11} seconds. Because the simulations take a long time to run, the applied voltage and current density are rather high in this particular instance. This was done to be able to raise the temperature quickly to show its effect on the variables. The current density (voltage) will be kept to lower values in more realistic scenarios.

4.6.4 Steady-state hydrodynamic model

Based on the fact that there are four unknown boundary conditions (2 for electrons and 2 for holes), and the net generation rate is unknown at this time, it was determined that a simpler model would be of great benefit in order to reduce the number of unknowns. The hydrodynamic model was reduced to a steady-state version, where the net generation rate does not appear and only one carrier density is solved at a time.

As a first step, Eqs. (4.1) and (4.2) were simplified to a steady-state version. Then subtracting Eq. (4.2a) from Eq.(4.2b) the equations reduce to one as follows:

$$\frac{\partial}{\partial x^*}\left[(\mu_h n_h^* + \mu_e n_e^*)\frac{\partial V^*}{\partial x^*}\right] + \beta\frac{\partial}{\partial x^*}\left[\mu_h\frac{\partial n_h^*}{\partial x^*} - \mu_e\frac{\partial n_e^*}{\partial x^*}\right] = 0. \qquad (4.7)$$

The following step is to use the mass action law [112, 113], namely, $n_{th}^2/N_0^2 = n_e^* n_h^*$, solving for n_e^* and substituting, the equations become

$$\frac{\partial}{\partial x^*}\left[\left(\mu_h n_h^* + \mu_e\frac{n_{th}^2}{N_0^2 n_h^*}\right)\frac{\partial V^*}{\partial x^*}\right] + \beta\frac{\partial}{\partial x^*}\left[\mu_h\frac{\partial n_h^*}{\partial x^*} - \mu_e\frac{\partial}{\partial x^*}\left(\frac{n_{th}^2}{N_0^2 n_h^*}\right)\right] = 0. \quad (4.8)$$

In this equation the hole density is the only unknown variable. The net generation rates have been canceled out, and by now only the two boundary conditions for holes are unknown. This equation coupled with Gauss' Law, Eq. (4.1a), and the energy equation, Eq. (4.1f), will help determine the most appropriate boundary conditions for the hole density. Moreover, once the distribution of the hole density is obtained, the electron density can be solved for by invoking the mass action law. And finally, the net generation rate can also be back-calculated. The spacial discretization scheme is the same as that used in Eqs. (4.5). Lastly, in order to avoid the non-linearities, the hole densities which resulted because of the mass action law are evaluated at the previous iteration, while the other linear terms are evaluated at the present time step.
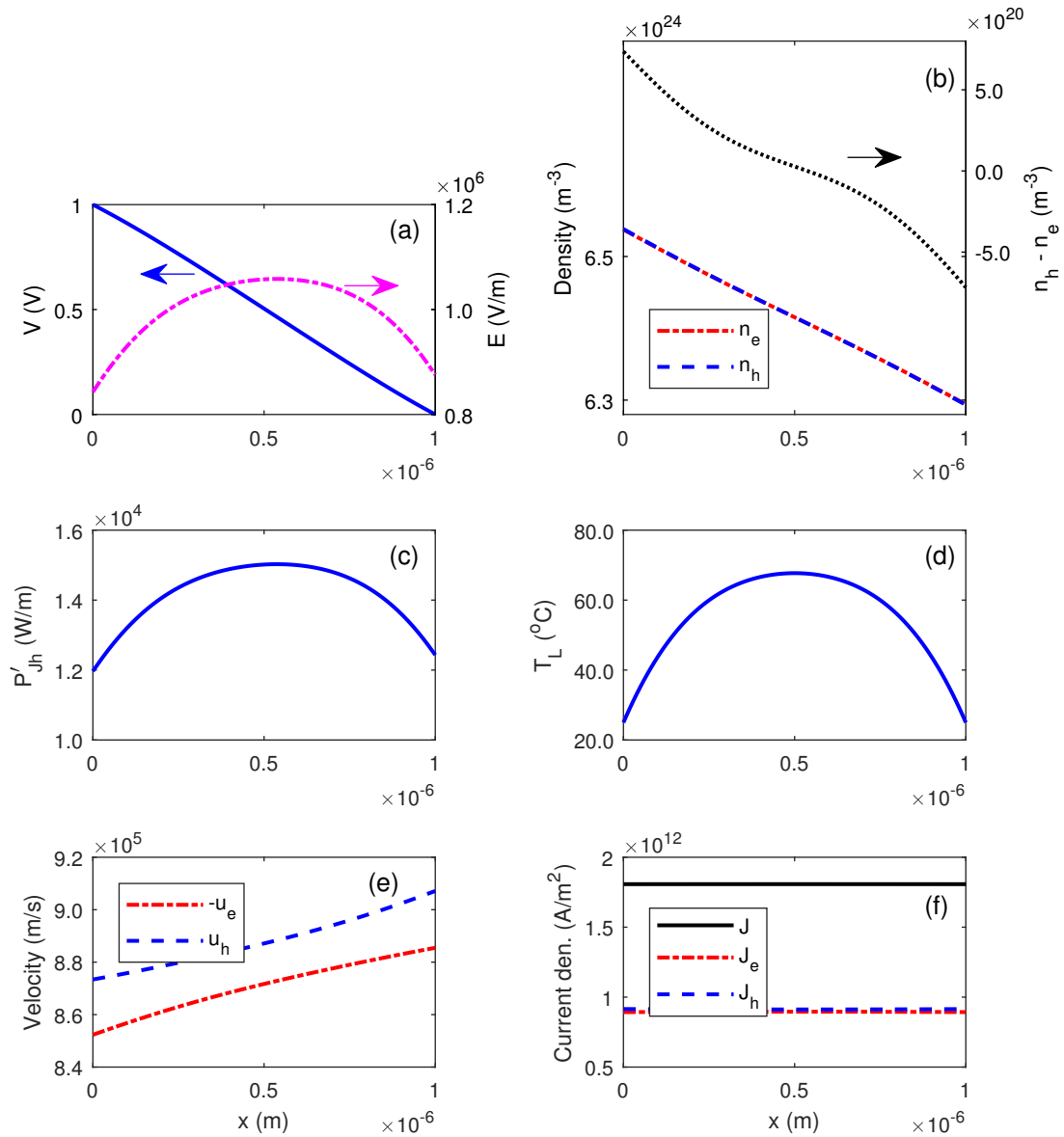
Figure 4.2: Sample set of solutions with hydrodynamic model when applied to graphite. Parameter values: $V_{app} = 1$ V, $L = 10^{-6}$ m, $D = 10^{-7}$ m.

4.6.5 Stability of the steady-state hydrodynamic model

Knowing that the hydrodynamic model is prone to some instabilities, some are due to the diffusion term, the stability of the steady-state version of Eqs. (4.1) will be checked in this section. To accomplish this goal, Eq. (4.8) was further simplified. By considering the electron and hole mobilities to be equal, the following equation is obtained

$$\frac{\partial}{\partial x^*}\left[\mu_h\left(n_h^* + \frac{n_{th}^2}{N_0^2 n_h^*}\right)\frac{\partial V^*}{\partial x^*}\right] + \beta\frac{\partial}{\partial x^*}\left[\mu_h\frac{\partial}{\partial x^*}(n_h^* - n_e^*)\right] = 0. \qquad (4.9)$$

Making use of Gauss' Law, Eq. (4.1a), to substitute the difference of holes and electrons on the second term, and rearranging yields

$$\frac{\partial}{\partial x^*}\left[\mu_h\left(n_h^* + \frac{n_{th}^2}{N_0^2 n_h^*}\right)\frac{\partial V^*}{\partial x^*} - \frac{\beta}{\zeta}\mu_h\frac{\partial^3 V}{\partial x^{*3}}\right] = 0. \qquad (4.10)$$

Integrating once

$$\mu_h\left(n_h^* + \frac{n_{th}^2}{N_0^2 n_h^*}\right)\frac{\partial V^*}{\partial x^*} - \frac{\beta}{\zeta}\mu_h\frac{\partial^3 V^*}{\partial x^{*3}} = C_1, \qquad (4.11)$$

and solving for n_h^*

$$n_h^{*2} - \left(\frac{\beta}{\zeta}\frac{\frac{\partial^3 V^*}{\partial x^{*3}}}{\mu_h\frac{\partial V^*}{\partial x^*}} + \frac{C_1}{\mu_h\frac{\partial V^*}{\partial x^*}}\right)n_h^* + \frac{n_{th}^2}{N_0^2} = 0, \qquad (4.12)$$

which is a quadratic equation in n_h^*. If a value of C_1 is found for which a root to this equation is found, then the equations are stable. Though, to be able to solve this equation, the voltage and thermal density distributions need to be known a priori. In this situation, an existing solution that was obtained with the drift-diffusion model can be used, for example. In this case, the solution for *Case I.B* from Chapter 3 is taken as an input solution. The value of the constant C_1 is changed iteratively until a solution is found for n_h^*. The density distributions for electron, hole, and thermal densities are shown in Fig.4.3, and the value of C_1 was found to be equal to -1.8080.

4.7 Conclusions And Future Work

In this chapter, a simplified transient one-dimensional hydrodynamic model was successfully developed. The hydrodynamic model is applicable to a material with two charge carriers, which need not be in thermal equilibrium with the lattice. In addition, nondimensional analysis gave deep physical insights of the equations. Moreover, a numerical scheme based on finite differences and a fourth order Runge-Kutta was developed and validated using a problem from the literature. This work completed the goals of the chapter.

Nonetheless, the end-goal is to apply this model to graphite, and possibly, multilayer graphene devices. Based on these goals, the steady-state version of the hydrodynamic model was considered to aid in determining the electron and hole
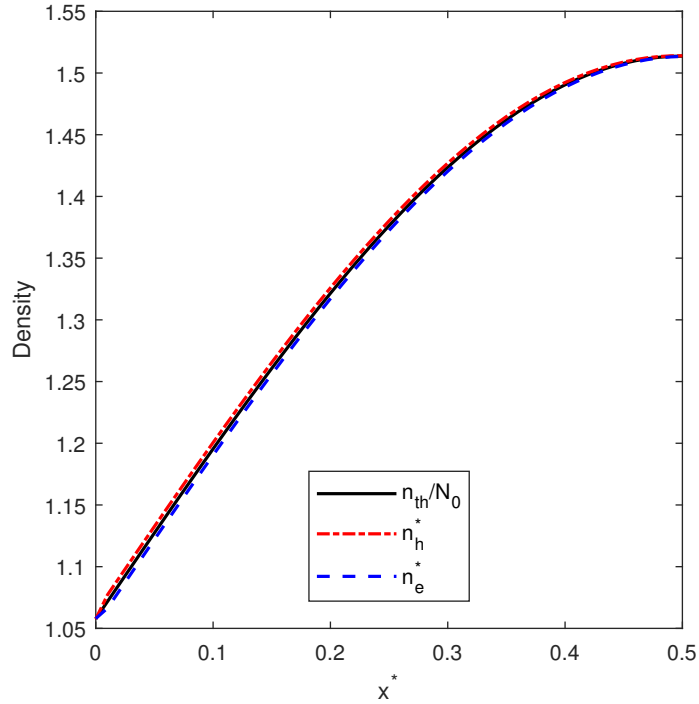
Figure 4.3: Density distributions obtained iteratively using Eq. (4.12).

densities, as well as the net generation rates. Moreover, an iterative scheme was developed to solve a simpler steady-state version to verify that the equations are stable.

Finally, the transient model will be applied to graphite devices. Because multilayer graphene has similar properties as graphite, it might be possible to apply this model to analyze multilayer graphene devices – a material of great interest in contemporary research.

Chapter 5

CONVENTIONAL ELECTRIC-THERMAL MODEL

5.1 Introduction

Extensive studies have been made regarding electronic/thermal breakdown on thin dielectric films with the purpose of understanding breakdown and devising preventive measures [14, 20–22]. In contrast, there is a lack of studies regarding thermal breakdown of biomass and other carbonaceous materials.

In this chapter, the objective is to elucidate the dynamics of the development of thermal breakdown. The main purpose is to use thermal breakdown as a mechanism for achieving conditions (temperatures) for thermochemical conversion, i.e., pyrolysis and gasification, of carbonaceous materials.

With this purpose in mind, a transient one-dimensional version of Eqs. (2.2) is used to obtain the temperature and voltage distributions for various carbonaceous materials whose thermophysical properties are very different: graphite, biochar, and wood. It is of special interest to compare the magnitude of the applied voltage and power needed to produce pyrolysis temperatures, as well as the time that such temperatures are reached under different applied voltages.

It is noted that because one of the main material properties used in this model, namely the electrical conductivity, is a 'macroscale' property, it can be readily measured for most materials. The electrical conductivity can be measured on crystalline and non-crystalline materials, as such, this model can be applied to either type of material. In contrast, hydrodynamic models are based on 'microscale' properties, such as carrier mobilities and densities. It is very difficult to define, and perhaps not viable to measure, these properties on non-crystalline materials such as biochar and wood. Therefore, the versatility of the electric-thermal model in this chapter will be exploited to analyze the three distinct carbonaceous materials of interest: graphite, biochar, and wood.

This chapter has been published as Ref. [114].

5.2   Description Of The Problem

In this study, a rod of carbonaceous material of length L and diameter D is subject to a constant voltage, V_{app}, applied on the left end of the rod while the right end is grounded, as shown in Fig. 5.1. Due to the electric field, the motion of charge carriers produces a total current density J, which generates Joule heating in the rod that results in a temperature rise. Both sides of the rod have a fixed temperature equal to the ambient temperature T_∞. The rod is exposed to heat losses by convection to the ambient air and radiation exchange with the surrounding surfaces. The surrounding surfaces and the ambient air are at the same temperature T_∞.
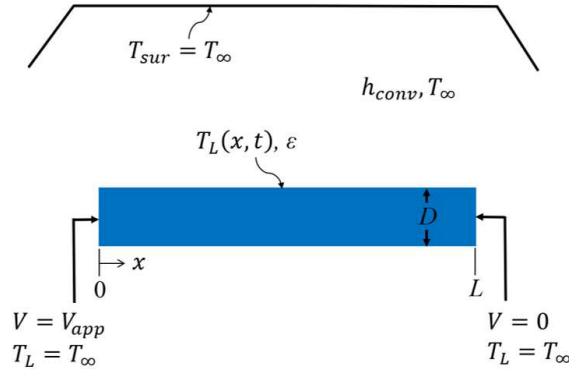
Figure 5.1:   Schematic representation of the rod under an applied voltage, with boundary conditions and heat losses.

5.3   Governing Equations

A transient one-dimensional version of the electric-thermal coupled model is composed of Gauss' Law (5.1a), charge conservation (5.1b), and energy conservation (5.1c), as follows:

$$\frac{\partial^2 V}{\partial x^2} = -\frac{\rho}{\epsilon_r \epsilon_0}, \tag{5.1a}$$

$$\frac{\partial \rho}{\partial t} = \frac{\partial}{\partial x}\left(\sigma(T_L)\frac{\partial V}{\partial x}\right), \tag{5.1b}$$

$$C_{L,v}(T_L)\frac{\partial T_L}{\partial t} = \frac{\partial}{\partial x}\left(k_L(T_L)\frac{\partial T_L}{\partial x}\right) + \sigma(T_L)\left(\frac{\partial V}{\partial x}\right)^2 - \frac{4h_{Tot}}{D}(T_L - T_\infty), \tag{5.1c}$$

where $V(x,t)$ is the electrostatic potential, $\rho(x,t)$ is the electric charge density, and $T_L(x,t)$ is the lattice temperature. The induced magnetic field effects are small, and, therefore, have been neglected. The Biot number is below 0.1 for the three materials analyzed in this paper. Consequently, temperature gradients in the radial and angular dimension have also been neglected. Thus, the problem effectively reduces to one

dimension. The total heat transfer coefficient is defined as $h_{Tot} = h_{conv} + h_{rad}$, where h_{conv} is the convection coefficient, and $h_{rad} = \varepsilon \sigma_{SB}(T_{L,ave} + T_{sur})(T_{L,ave}^2 + T_{sur}^2)$ is the linearized radiation coefficient [97]. The physical parameters are: the emissivity, ε, Stefan-Boltzmann's constant, σ_{SB}, the relative permittivity, ϵ_r, the permittivity of free space, ϵ_0, the electrical conductivity, $\sigma(T_L)$, the thermal conductivity, $k_L(T_L)$, and the volumetric heat capacity, $C_{L,v}(T_L) = \rho_m c_p(T_L)$, where ρ_m is the mass density and $c_p(T_L)$ is the specific heat.

The boundary conditions are: $T_L(0,t) = T_L(L,t) = T_\infty$, and $V(0,t) = V_{app}$ and $V(L,t) = 0$, as seen in Fig. 5.1. The initial conditions are as follows: the initial lattice temperature across the rod is equal to the ambient temperature, i.e., $T_L(x,0) = T_{L,i} = T_\infty = 298$ K. The charge density is equal to zero everywhere, i.e., $\rho(x,0) = 0$, which gives rise to an initial linear voltage distribution $V(x,0) = V_{app}(1 - x/L)$ and a constant electric field $E_0 = V_{app}/L$. The initial charge density may take moderate nonzero values, generating a non-uniform initial electric field distribution, however, this moderate change in initial conditions does not affect the final results. A value of charge density equal to zero was chosen for simplicity. Note that no boundary conditions are needed for the charge density.

In this model the current density is assumed to be uniform across the area of the rods. This assumption is more realistic for graphite than for biochar or wood due to the fibrous structure of these two materials, which affects the contact between the material and the electrode. However, it constitutes a good approximation during the onset of thermal runaway. The situation changes significantly for wood, a dielectric material, when thermal breakdown occurs, since this mechanism typically involves the formation of highly conductive channels.

5.4 Nondimensional Equations

Using the following dimensionless parameter definitions: $x^* = x/L$, $T_L^* = T_L/T_\infty$, $V^* = V/|V_{app}|$, and $\rho^* = \rho/\rho_0$, Eqs. (5.1) are nondimensionalized as follows:

$$\frac{\partial^2 V^*}{\partial x^{*2}} = -\rho^*, \tag{5.2a}$$

$$\frac{\partial \rho^*}{\partial t^*} = M_1 \frac{\partial}{\partial x^*}\left(\frac{\sigma(T_L)}{\sigma_{ref}}\frac{\partial V^*}{\partial x^*}\right), \tag{5.2b}$$

$$\frac{C_{L,v}(T_L)}{C_{L,v,ref}}\frac{\partial T_L^*}{\partial t^*} = \left(\frac{D/4}{L}\right)^2 \frac{\partial}{\partial x^*}\left(\frac{k_L(T_L)}{k_{L,ref}}\frac{\partial T_L^*}{\partial x^*}\right)$$
$$+ M_2 \left(\frac{D/4}{L}\right)^2 \frac{\sigma(T_L)}{\sigma_{ref}}\left(\frac{\partial V^*}{\partial x^*}\right)^2 - \mathrm{Bi}\frac{h_{Tot}}{h_{conv}}(T_L^* - 1), \tag{5.2c}$$

where $t^* = \mathrm{Fo} = \alpha t/(D/4)^2$ is the dimensionless time or Fourier number, $\alpha = k_{L,ref}/C_{L,v,ref}$ is the thermal diffusivity, $\rho_0 = |V_{app}|\epsilon_r\epsilon_0/L^2$, and $\mathrm{Bi} = h_{conv}(D/4)/k_{L,ref}$ is the Biot number. The characteristic length for both Fo and Bi numbers is

$L_c = D/4$, and $(D/(4L))^2$ is the geometric aspect ratio of the rods. The subscript 'ref' denotes reference value at room temperature. $M_1 = (\sigma_{ref}(D/4)^2/\epsilon_r\epsilon_0)/\alpha$, and by defining $\sigma_{ref}/\epsilon_r\epsilon_0 \equiv 1/\tau_d$, where τ_d is the dielectric relaxation time, M_1 can be re-written as $M_1 = (D/4)^2/(\tau_d\alpha) \equiv 1/\mathrm{Fo}_2$, which has the form of the inverse of a static Fourier number which represents a dimensionless time scale for the charge dynamics; $M_2 = \sigma_{ref}V_{app}^2/k_{L,ref}T_\infty$ can be interpreted as the effectiveness at which the input electrical energy is removed by heat conduction. Typical values of these dimensionless parameters are provided in Table 5.1.

5.5   Numerical Methods

Equations (5.2) were discretized using first and second order finite difference approximations, and Eqs. (5.2b) and (5.2c) were integrated in time using Euler's method. The set of discretized equations become

$$\frac{V_{k-1} - 2V_k + V_{k+1}}{(\Delta x)^2} = -\frac{\rho_k^{n+1}}{\epsilon_r\epsilon_0}, \tag{5.3a}$$

$$\frac{\rho_k^{n+1} - \rho_k^n}{\Delta t} = \frac{1}{\Delta x}\left[\sigma_{k+1/2}\frac{(V_{k+1} - V_k)}{\Delta x} - \sigma_{k-1/2}\frac{(V_k - V_{k-1})}{\Delta x}\right], \tag{5.3b}$$

$$C_{L,v,k}\frac{T_{L,k}^{n+1} - T_{L,k}^n}{\Delta t} = \frac{1}{\Delta x}\left[k_{k+1/2}\frac{(T_{L,k+1}^n - T_{L,k}^n)}{\Delta x} - k_{k-1/2}\frac{(T_{L,k}^n - T_{L,k-1}^n)}{\Delta x}\right]$$
$$+ P_{Jh,k}''' - \frac{4h_{Tot,k}}{D}(T_{L,k} - T_\infty), \tag{5.3c}$$

where the Joule heating power is evaluated as

$$P_{Jh,k}''' = \begin{cases} \sigma_{k+1/2}\left(\frac{V_{k+1} - V_k}{\Delta x}\right)^2 & \text{for } 0 \le x \le L/2, \\ \sigma_{k-1/2}\left(\frac{V_k - V_{k-1}}{\Delta x}\right)^2 & \text{for } L/2 < x \le L, \end{cases} \tag{5.4}$$

in order to improve the stability of the algorithm. Equations (5.3) were simplified by substituting Eq. (5.3b) into Eq. (5.3a) for ρ_k^{n+1}, where the index 'k' denotes the grid location and the superscript '$n+1$' denotes the next time step, forming a single semi-implicit equation. Upon this substitution, the charge density, ρ, becomes a secondary variable. In addition, because no boundary condition is needed (or specified) for the charge density, the boundary values are extrapolated.

The tri-diagonal matrix algorithm (TDMA) was employed to solve the tri-diagonal matrix resulting from the combined Eqs. (5.3a) and (5.3b). In this chapter, various carbonaceous materials with significantly different properties are analyzed. Thus, grid size and time step independence tests were performed to determine the necessary resolution for each material. The grid size and time step used for each material is stated in the corresponding results section.

76

5.6 Material Properties

Wood: The thermophysical properties of wood depend on various parameters, including moisture content and temperature [81–84]. During the simulations, average values for the thermal conductivity, heat capacity, and electrical conductivity were used for wood at 12% moisture content. Above ambient temperature, the thermal conductivity varies with absolute temperature, in Kelvin, as follows [83]:

$$k_L(T_L) = 0.0994 \exp(0.002T_L), \tag{5.5}$$

where k_L has units of W/(m K). Similarly, the specific heat depends on temperature as [83]:

$$c_p(T_L) = 1916.8 \ln(T_L) - 9268.8, \tag{5.6}$$

where c_p has units of J/(kg K). Lastly, the electrical conductivity depends on temperature as [82]:

$$\sigma(T_L) = 371535.2 \times 10^{-3660/T_L}, \tag{5.7}$$

where σ has units of $(\Omega \text{ m})^{-1}$. A constant value of 800 for the dielectric constant was estimated from Refs. [81, 83]. The properties of wood at ambient temperature are summarized in Table 5.2.

Biochar: It has been reported that the electrical conductivity of wood has a strong dependence on temperature [83]. However, the electrical conductivity of dry wood is so low that it still remains a good electrical insulator at moderate temperatures. Nonetheless, when wood is heated to temperatures of about $T_{carb} \approx 500 - 600$ °C, wood becomes char, also known as biochar, and the electrical conductivity increases by several orders of magnitude [85–87]. For instance, measured at room temperature, the electrical conductivity of oven dry wood is of the order of 10^{-15} $(\Omega \text{ m})^{-1}$ [83], whereas the electrical conductivity of biochar produced at $T_{carb} = 600$ °C is roughly 7×10^{-4} $(\Omega \text{ m})^{-1}$ [86]. In this study, average properties of biochar produced at $T_{carb} = 800$ °C are utilized, and they are summarized in Table 5.2. The specific heat of biochar increases for the first 50 degrees above room temperature, then decreases for the next 30 degrees [115], therefore, it has been considered as constant. The thermal conductivity depends on temperature approximately as follows [85, 116]:

$$k_L(T_L) = 0.0013T_L - 0.01, \tag{5.8}$$

and the electrical conductivity depends on temperature as [86, 117]:

$$\sigma(T_L) = 64565 \times 10^{-1000/T_L}, \tag{5.9}$$

where the units of k_L and σ are the same as for wood. A value of 64 for the dielectric constant was estimated from Ref. [117].

Graphite: As biomass is carbonized, its electrical conductivity increases by several orders of magnitude. In a similar manner, graphite is made when a mixture of hydrocarbons are heated to even higher (graphitization) temperatures. As opposed to biochar, graphite may be a highly crystalline material with a comparatively low

porosity. These attributes enhance the electrical conductivity of graphite, which is about two to three orders of magnitude higher than that of biochar obtained at temperatures above 700 °C. However, compared to metals, the electrical conductivity of graphite is more than two orders of magnitude lower. For example, the electrical conductivity of POCO graphite is 7.8×10^4 $(\Omega$ m$)^{-1}$ compared to copper, which is 3.58×10^7 $(\Omega$ m$)^{-1}$ [88]. In this chapter, properties of (polycrystalline) POCO® Graphite AXF-5Q are used, so when future reference is made to graphite without a qualifier, it means POCO graphite. The electrical conductivity and other thermophysical properties of POCO and other commercial polycrystalline graphites are nearly isotropic. The temperature dependence of the specific heat is given in Eq. (4.3). From ambient temperature to 1000 K, the experimental data [88] for the thermal conductivity were fitted with the following equation

$$k_L(T_L) = 9 \times 10^{-5}T_L^2 - 0.2048T_L + 166.2, \tag{5.10}$$

where $R^2 = 0.998$. The temperature dependence of the electrical conductivity [88] from ambient temperature to 1000 K was fitted as:

$$\sigma(T_L) = -0.0937T_L^2 + 174.7T_L + 34298, \tag{5.11}$$

where $R^2 = 0.998$. The same dielectric constant value of 13 used for Pyrolytic graphite in Chapter 3 is used for POCO graphite. The properties of graphite at room temperature are summarized in Table 5.2.

Table 5.1: Nondimensional parameters.

Material	Bi	Fo$_2 \equiv 1/M_1$	M_2
Wood	1.4×10^{-2}	9.37×10^{-2}	1 (at $V_{app} = 1.7 \times 10^4$ V)
Biochar	6.6×10^{-3}	2.41×10^{-10}	1 (at $V_{app} = 2.1$ V)
Graphite	2.2×10^{-5}	2.89×10^{-11}	1 (at $V_{app} = 3.0$ V)

Table 5.2: Material properties at ambient temperature T_∞ [81–86, 88, 97, 115–117].

Material	$\rho_{m,ref}$ (kg/m^3)	$c_{p,ref}$ (J/(kg K))	$k_{L,ref}$ (W/(m K))	ε -	σ_{ref} $((\Omega$ m$)^{-1})$	ϵ_r -
Wood	680	1650	0.18	0.82	1.9×10^{-7}	800
Biochar	500	1100	0.38	0.75	2.6×10^1	64
Graphite	1770	721	113	0.8	7.8×10^4	13

Table 5.3: Simulation parameter values.

Parameter	Symbol	Value
Rod length	L	10^{-2} m
Rod diameter	D	10^{-3} m
Dimensionless ratio	$(D/(4L))^2$	6.25×10^{-4}
Convection heat transfer coefficient	h_{conv}	10 W/(m^2 K)
Ambient temperature	T_∞	298 K

5.7   Results And Discussion

The results from our previous steady-state drift-diffusion model for pyrolytic graphite, see Chapter 3 and Ref. [96], are utilized in Subsection 5.7.1 to validate the proposed transient model, which is run until steady-state is reached. Analyses for charge and heat transport mechanisms for POCO graphite, biochar, and wood are presented in Subsections 5.7.2, 5.7.3, and 5.7.4, respectively. Unless otherwise stated, the parameter values used for the simulations are provided in Table 5.3. Subsequently, the nondimensional energy equation (5.2c) is analyzed for two purposes: (1) to compare the magnitude of the right-hand side terms for each material, and (2) to calculate the nondimensional time needed to reach a certain maximum lattice temperature (Subsection 5.7.5).

Let us pause here for a second to draw attention regarding the dielectric constant, ϵ_r. The values for ϵ_r for the three carbonaceous materials under consideration in this chapter have been estimated based on values found in the literature, see Sec. 5.6; therefore, they constitute a source of uncertainty. As a consequence, the values were varied to understand their effect on the overall results. Because ϵ_r is inversely proportional to the charge density, ρ, (See Eq. (5.1a)), an increase in ϵ_r results in an increase in ρ to maintain the right-hand side term of Eq. (5.1a) constant. Aside from a change in magnitude of ρ, there are no visible effects on the rest of the results when this value is increased a few orders of magnitude, just as determined in Subsections 3.5.2 and 3.5.4.

5.7.1   Comparison with steady-state drift-diffusion model for intrinsic pyrolytic graphite

A one-dimensional steady-state drift-diffusion electric-thermal model was derived in Chapter 3 and Ref. [96] to analyze charge carrier densities and Joule heating on intrinsic pyrolytic graphite rods. The model was based on fundamental variables such as electron/hole densities and their mobilities, and it was validated against published results [103, 104]. The drift-diffusion model cannot be used for non-crystalline materials, such as wood and biochar, because the needed properties are not available. In contrast, the present electric-thermal model is based on the electrical conductivity

of the materials, which can be measured regardless of material structure or composition.

In this section, the drift-diffusion model is used to validate the transient one-dimensional electric-thermal model. The electrical conductivity for pyrolytic graphite is defined as $\sigma = 2en_{th}\mu_{ave}$, where e is the elementary charge, n_{th} is the thermal/intrinsic density, and μ_{ave} is the carrier mobility. The temperature-dependent expressions for the thermal density and the mobility, in addition to the thermal conductivity, are given in Sec. 3.4 and Ref. [96]. The mass density of pyrolytic graphite is taken as 2200 kg/m^3 [88], and the temperature-dependent specific heat is given in Ref. [88]. It is noted that the electrical and thermal conductivities of pyrolytic and POCO graphite are different. In this section, the properties of pyrolytic graphite are used. The parameter values are the same as those used for *Case I.B* in Subsection 3.5.4: $V_{app} = 1.0$ V, $L = 10^{-2}$ m, and $D = 10^{-3}$ m. The time step used was $\Delta t = 10^{-7}$ seconds, combined with a spatial resolution of 101 nodes, chosen after grid size and time step independence tests.

The temporal and spatial distribution for the charge density, $\rho/e = (n_h - n_e)$, and the lattice temperature, T_L, are shown in Figs. 5.2(a) and 5.2(b), respectively. The charge density varies in space from left to right in an anti-symmetric fashion from about 0.5×10^{13} m^{-3} to -0.5$\times10^{13}$ m^{-3}, and the lattice temperature has a shape similar to an inverted parabola with a maximum temperature value of 173 °C. For this case, steady-state is reached in 8.0×10^{-2} seconds, and the corresponding current density has a value of 1.74×10^8 A/m^2, just as computed with the drift-diffusion model from Chapter 3 and Ref. [96]. Figure 5.2 compares the charge distribution (difference between holes and electrons) and the lattice temperature distribution obtained with the two models, and it is seen that the steady-state results are virtually the same. Figure 3.5 contains a full set of results for this case (*Case I.B*).

5.7.2 POCO graphite

Compared to biomass and biochar, POCO graphite has higher thermal and electrical conductivities. While the electrical conductivity increases moderately with temperature, the thermal conductivity decreases. This enhances the Joule heating effect, which means that higher temperatures are reached faster.

Figure 5.3 shows the spatial and temporal evolution of relevant variables under the following operating parameters: $V_{app} = 3$ V, $L = 10^{-2}$ m, and $D = 10^{-3}$ m. The spatial resolution needed for the numerical solution for this material is 1001 nodes with a time step of $\Delta t = 10^{-7}$ s. Figures 5.3(a), (c), and (e) show the voltage distribution, electric field, and charge density, respectively. Because the initial condition for charge density is zero, and the initial temperature is constant across the rod, the electric field is initially constant across the domain. As time advances, it starts displaying a minimum at the center of the rod, mainly due to the positive temperature dependence of the electrical conductivity. While the nominal value of the electric field is 300 V/m, its value at the center of the rod is 277 V/m and the maximum value is 402 V/m, which occurs at both boundaries. Also as time

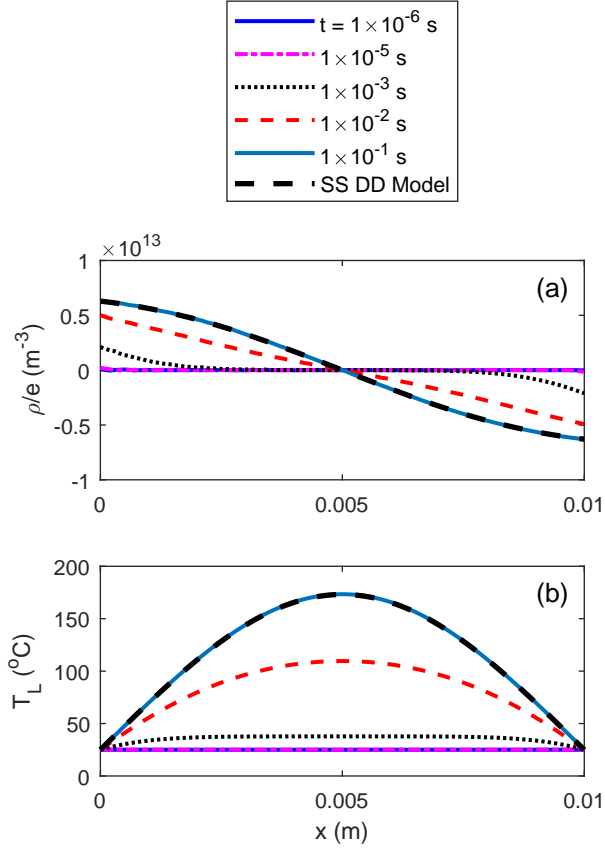Figure 5.2: Spatial distribution and temporal evolution of the charge density, $\rho/e = (n_h - n_e)$, and lattice temperature, T_L, for pyrolytic graphite. Comparison of the solution using the transient electric-thermal model (this chapter) and the steady-state drift-diffusion (SS DD) electric-thermal model from Chapter 3 and Ref. [96]. Parameter values: $V_{app} = 1.0$ V, $L = 10^{-2}$ m, $D = 10^{-3}$ m.

progresses, the voltage distribution starts deforming from a perfect straight diagonal line into an elongated "S" shape, while the distribution of charge density takes an anti-symmetric shape, increasing smoothly from large negative values on the left end of the rod to large positive values on the right end. The maximum magnitude of the charge density at the boundaries is approximately $\rho/e = 10^{14}$ m^{-3}. Thus, most of the charge accumulates near the boundaries.

Figures 5.3(b), (d), and (f) show Joule heating power, heat losses by convection and radiation, and the lattice temperature, respectively. From Fig. 5.3(b) it is seen that as time progresses, the Joule heating power across the rod increases, due to the increasing magnitude of the current density. The magnitude of Joule heating power is larger at the boundaries and relatively flat towards the middle of the rod. The highest value of the Joule heating power is 9900 W/m at the boundaries and its lowest value is 6800 W/m. The magnitude of the radiation and convection losses follow closely the distribution of the lattice temperature, with a maximum value in the middle that reaches 46 W/m, and a value of zero at the boundaries where the temperature is kept constant at T_∞. As mentioned, the lattice temperature displays a maximum value in the middle, where $T_{L,max}$ reaches 500 °C, which was the maximum temperature allowed in the simulation. From the figure, it is observed that the maximum lattice temperature was reached at $t = 1.4127 \times 10^{-1}$ s, as noted in the legend. In addition, the total current density at this time was 3.14×10^7 A/m^2.

A second case was simulated for graphite using the same rod diameter and length, but with $V_{app} = 30$ V, one order of magnitude higher than the previous case. The results are shown in Fig. 5.4, where one of the most noticeable effects is that the temperature reaches 500 °C at 1.1939×10^{-3} seconds, which is about two orders of magnitude faster than for the case with $V_{app} = 3$. It is also seen that the spatial distribution for all the parameters became steeper near the boundaries and the plateau covers the majority of the inner domain of the rod. Because a higher applied voltage was used, the actual values of the relevant variables also increased. For example, the maximum electric field at the boundaries has a value of 4250 V/m while the minimum value is nearly the same as the nominal value of 2980 V/m, as shown in Fig. 5.4(c). The sharp variation of electric field near the boundaries is caused by a large increase of charge density, which reaches a maximum magnitude of roughly 10^{16} m^{-3} with much less charge accumulation inside the domain, as shown in Fig. 5.4(e). This higher charge at both ends of the rod causes the voltage distribution to have a sharp curvature near the boundaries, as seen in Fig. 5.4(a). The maximum value of the Joule heating power is 1.12×10^6 W/m at the boundaries, while inside the domain the minimum value is 7.88×10^5 W/m. The maximum magnitude of the heat losses is 62 W/m, shown in Fig. 5.4(d), and the total current density in this case reached a value of 3.37×10^8 A/m^2, about one order of magnitude higher than the previous case when 3 Volts were applied.

In order to analyze the temporal evolution of $T_{L,max}$ as a function of applied voltage, a third case with $V_{app} = 10$ Volts was simulated. The results of the thermal runaway as a function of applied voltage are shown in Fig. 5.5(a), where it is seen

Figure 5.3: Spatial distribution and temporal evolution of various variables for POCO graphite. Parameter values: $V_{app} = 3$ V, $L = 10^{-2}$ m, $D = 10^{-3}$ m.

Figure 5.4: Spatial distribution and temporal evolution of various variables for POCO graphite. Parameter values: $V_{app} = 30$ V, $L = 10^{-2}$ m, $D = 10^{-3}$ m.

that when $V_{app} = 30$ V, a lattice temperature of 500 °C is reached in just 1.1939×10^{-3} seconds, while for $V_{app} = 10$ V, the same temperature is reached in 1.0978×10^{-2} seconds, nearly 10 times slower. For the case of $V_{app} = 3$ V, the maximum temperature is reached in 1.4127×10^{-1} seconds, over 100 times slower than for $V_{app} = 30$ V. Thus, for an order of magnitude increase on the applied voltage, the temperature of the rod increases two orders of magnitude faster, displaying a typical behavior of thermal runaway. In addition to the maximum lattice temperature, the total current density for all three cases is shown in Fig. 5.5(b), where it is seen that all three current densities increase as time advances due to the positive temperature dependence of the electrical conductivity of POCO graphite. Also, at room temperature, the magnitude of the current density increases roughly by one order of magnitude when the applied voltage is increased by the same amount.
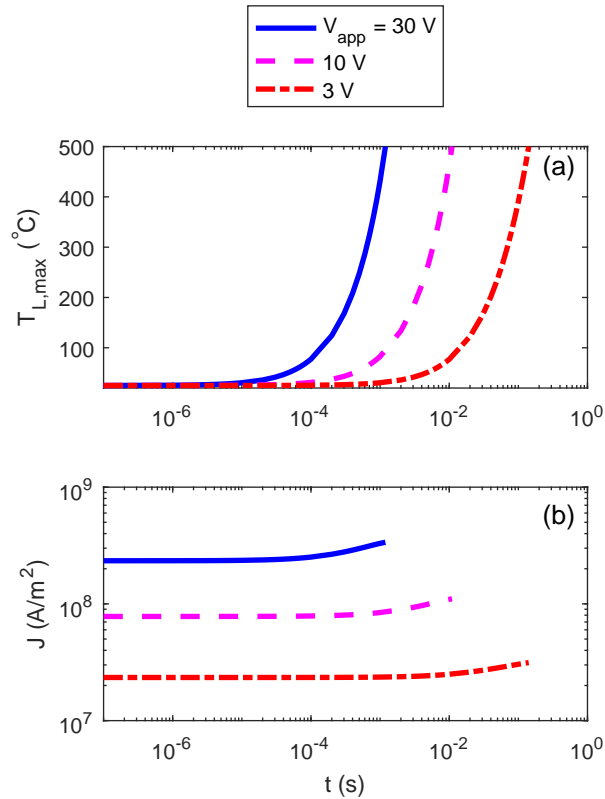
Figure 5.5: Temporal evolution of the maximum lattice temperature $T_{L,max}$ and total current density J for graphite under various applied voltages V_{app}, with $L = 10^{-2}$ m and $D = 10^{-3}$ m.

5.7.3 Biochar

Biochar has lower electrical and thermal conductivities than graphite, but the temperature dependence of the electrical conductivity is stronger. After grid

size and time step independence tests, it was determined that a spatial resolution consisting of 5001 nodes along with a time step of 10^{-7} seconds were needed for this material. The dynamics of charge and heat transport in biochar were analyzed using the following parameters: $V_{app} = 21$ V, $L = 10^{-2}$ m, and $D = 10^{-3}$ m, where the results are shown in Fig. 5.6. Because of the strong temperature dependence of the electrical conductivity, the steepness of the curves near the boundaries is very large for all the variables. Similar to the case for graphite when $V_{app} = 30$ V, in this case most of the charge accumulates at the boundaries of the rods, reaching a charge density of 5.21×10^{17} m^{-3}, as shown in Fig. 5.6(e). The charge accumulation produces an electric field of 9180 V/m at the boundary with a minimum value of 1970 V/m inside the domain, a value slightly lower than the nominal value of 2100 V/m seen in Fig. 5.6(c). For the same reason, the voltage distribution also undergoes a strong distortion near the boundaries, as observed in Fig. 5.6(a). The simulations of biochar were performed until a maximum lattice temperature of $T_{L,max} = 100$ °C was obtained because of the high uncertainty in the properties of this material at higher temperatures. This maximum lattice temperature was reached after 1.6556×10^{-1} seconds, as seen in Fig. 5.6(f). The heat losses by convection and radiation were small, reaching a maximum value of 3.9 W/m, shown in Fig. 5.6(d), while Joule heating power reached a much higher value of 413 W/m inside the rod and 1920 W/m at the boundaries. The value of the Joule heating power inside the domain is more than two orders of magnitude larger than the maximum heat losses by convection and radiation at the same location along the rod. In addition, the current density starts off at a value of 6.00×10^4 A/m^2 at room temperature and steadily increases to a maximum value of 2.66×10^5 A/m^2 when $T_{L,max}$ reaches 100 °C.

5.7.4 Wood

The last material to be analyzed is wood. While both, the electrical and thermal conductivities of wood are low, the former increases strongly with temperature. This causes a large gradient of the electrical conductivity near the boundaries which requires a large spatial resolution to resolve such gradients. In this case, 20001 nodes were used to obtain the distribution of variables inside the domain with a time step of 10^{-7} seconds. Due to the large gradients observed, the simulations were only run until a maximum lattice temperature of 30 °C was reached.

The applied voltage needed to raise the lattice temperature was 3.4×10^4 Volts, three orders of magnitude higher than for graphite and biochar, due to the low conductivity (large resistivity) of wood. Figure 5.7 also shows that even though the maximum lattice temperature reaches only 30 °C, the profiles for all variables, except voltage, are very steep near the boundaries and have large plateaus covering most of the interior domain of the rods. It is also seen that it took over 2.15 seconds for the temperature to increase to 30 °C, which is over one order of magnitude longer than the time needed for graphite to reach 500 °C when 3 Volts are applied.

The voltage, electric field, and charge density are shown in Figs. 5.7(a), (c), and (e), respectively. The charge density increases from -2.62×10^{20} m^{-3} on the left
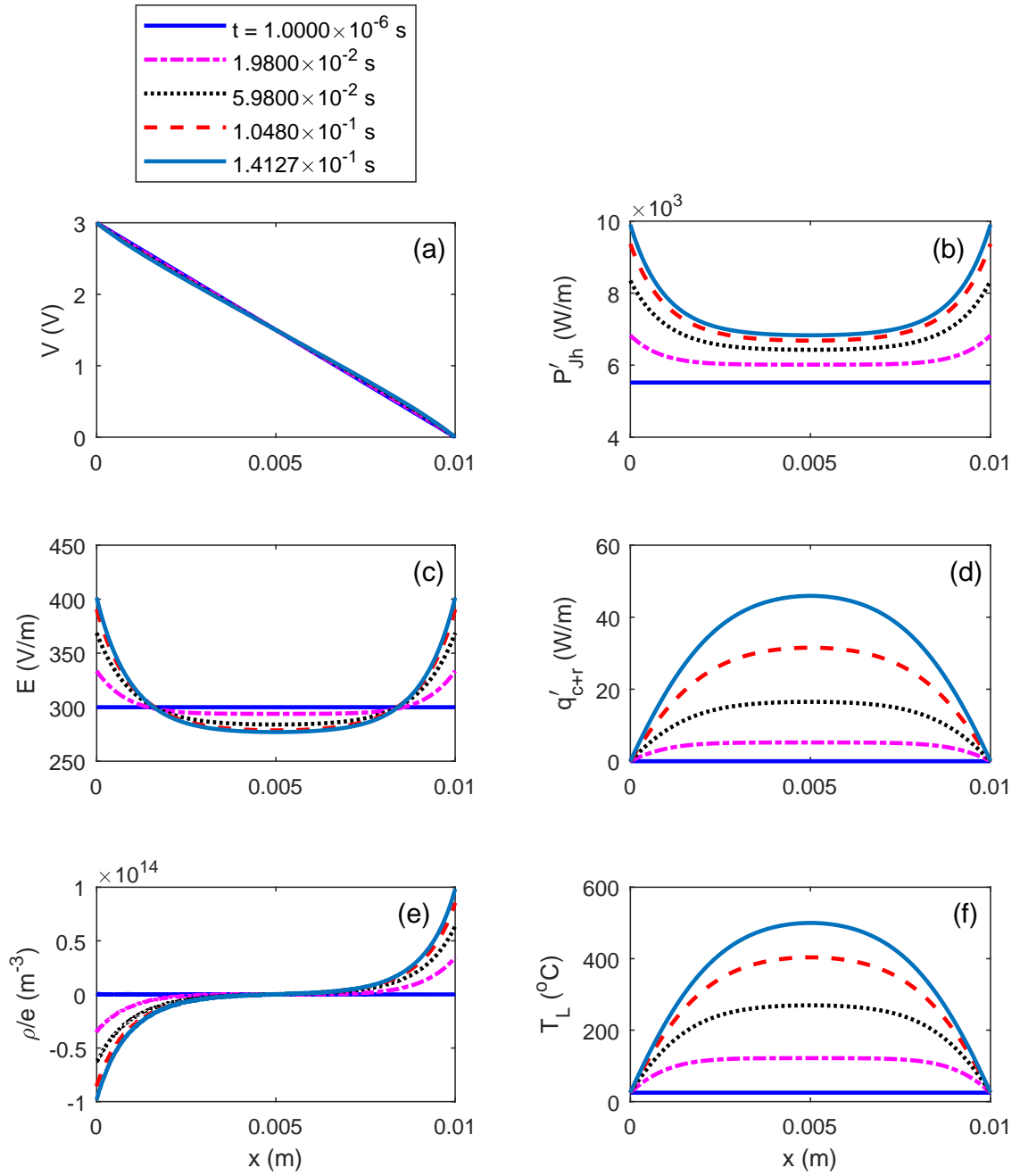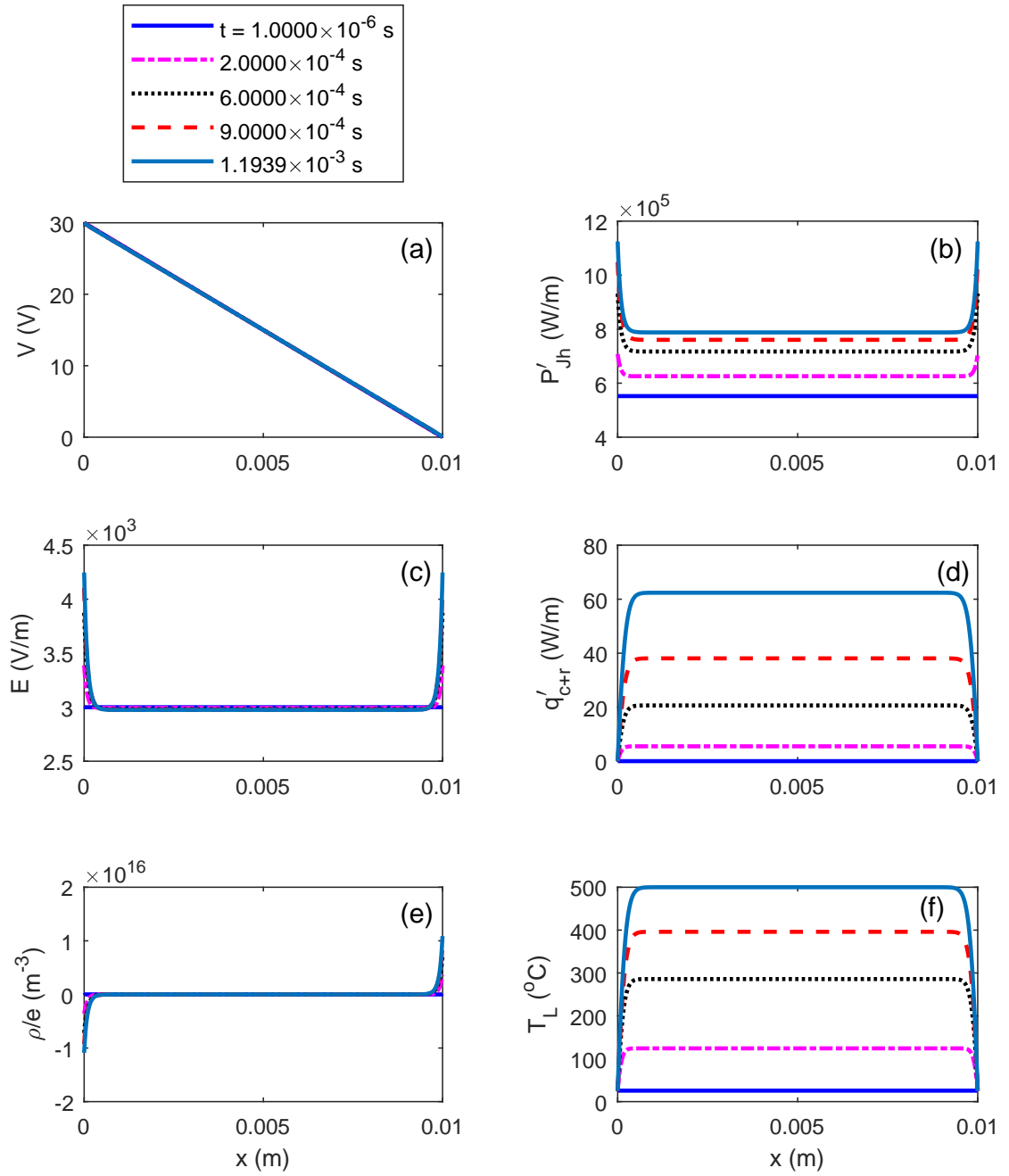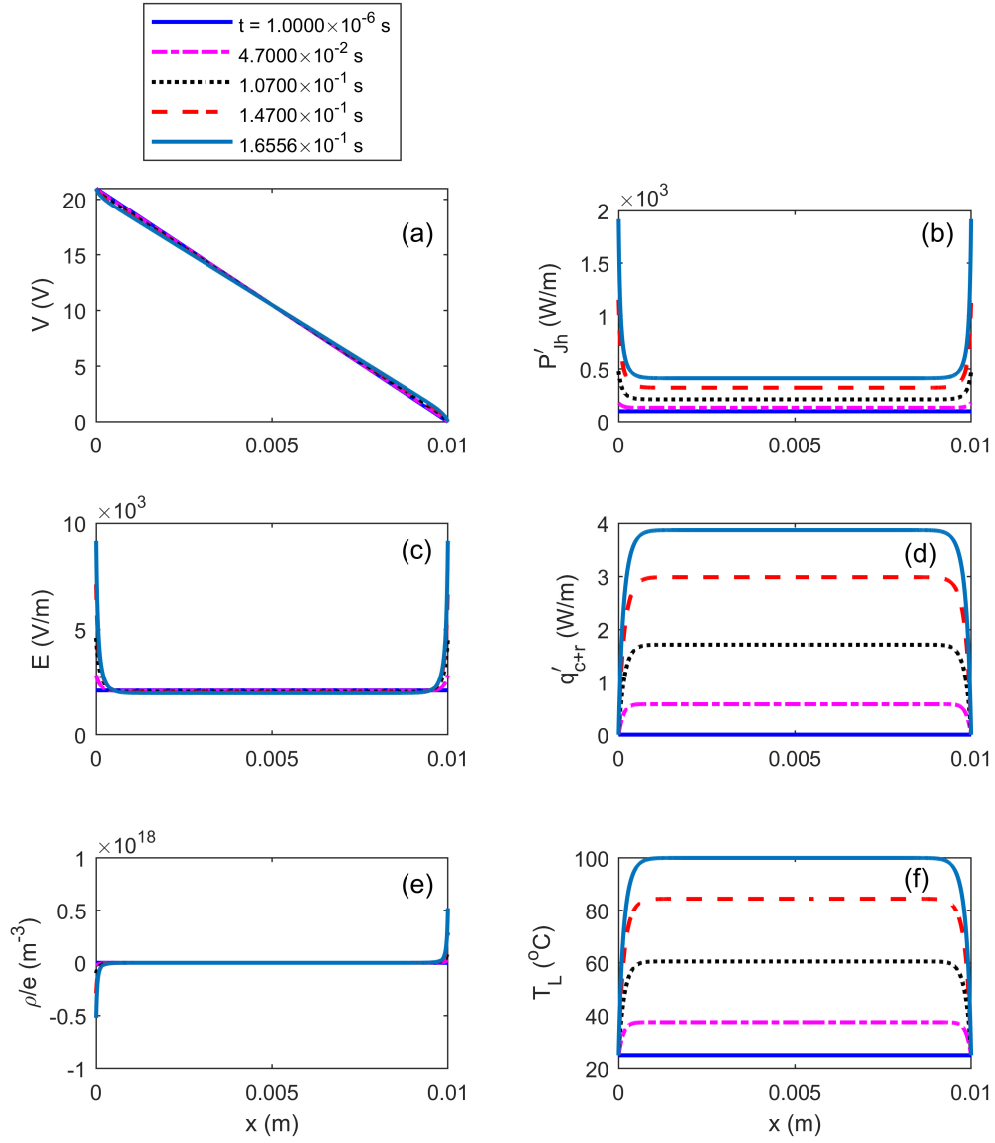
Figure 5.6: Spatial distribution and temporal evolution of various variables for biochar. Parameter values: $V_{app} = 21$ V, $L = 10^{-2}$ m, $D = 10^{-3}$ m.

boundary to 2.62×10^{20} m^{-3} on the right boundary. This causes the electric field to reach a value of 5.17×10^6 V/m at the boundaries and a value of 3.27×10^6 V/m in the middle of the rod, and the voltage distribution is distorted slightly from a straight diagonal line. Joule heating power is shown in Fig. 5.7(b) with a maximum value of 4.14 W/m at the boundary and a value of 2.64 W/m covering most of the inner length of the rod, while convection and radiation heat losses reach a maximum value of 0.236 W/m inside the rod, as seen in Fig. 5.7(d). Lastly, the initial current density has a value of 0.67 A/m^2 at room temperature and increases to 1.03 A/m^2 when $T_{L,max}$ reaches 30 °C, which is several orders of magnitude lower than that of graphite or biochar.

5.7.5   Nondimensional analyses

The nondimensional energy equation (5.2c) is used to generate Fig. 5.8, which provides a quick visual comparison of the relative magnitude of the various terms involved in the equation. It also serves as a guide to evaluate what terms are most relevant under different operating conditions for each material. The vertical dashed magenta line separates the low Joule heating area on the left from the high Joule heating area on the right. The dimensionless parameter M_2 on the horizontal axis depends on V_{app}, while the vertical axis depends on the geometry and the convection plus radiation heat transfer coefficient, represented by $\text{Bi}/(D/(4L))^2$. To the left of the dashed diagonal blue line, convection and radiation losses dominate, while to the right of this line, conduction losses through the boundaries are predominant.

Furthermore, Fig. 5.8 shows that due to the properties of graphite, even a small applied voltage results in a large value of M_2, while Bi remains quite small. Therefore, most cases result in high Joule heating with negligible convection and radiation losses. On the other hand, for biochar and wood, the heat losses will strongly depend on the magnitude of the applied voltage and the dimensions of the rod. For instance, the applied voltages that produce a value of $M_2 = 1$ (vertical dashed line) are 3 V for graphite, 2.1 V for biochar, and 1.7×10^4 V for wood. Thus, similarly to graphite, biochar requires low values of V_{app} to achieve high values of M_2, which results in high Joule heating; however, as opposed to graphite, biochar has a much lower thermal conductivity, which increases the value of Bi, and thus, both convective and radiative losses, as well as losses due to conduction at both ends of the rod are important. For the case of wood, the very small electrical conductivity implies that even high values of V_{app} result in low values of M_2 (low Joule heating) and the small thermal conductivity implies large values of Bi. Therefore, convective and radiative losses are large compared to other terms in the equation. Consequently, for thermal runaway to occur in wood, much larger applied voltages are required.

The results presented in Subsections 5.7.1 through 5.7.5 show that significantly different applied voltages are needed to raise the lattice temperature of the three materials analyzed. Therefore, further analysis to determine the relationship between lattice temperature, dimensionless applied voltage (M_2) and time (Fo), considering material and geometrical parameters, is performed in this section utilizing Eq. (5.2c).
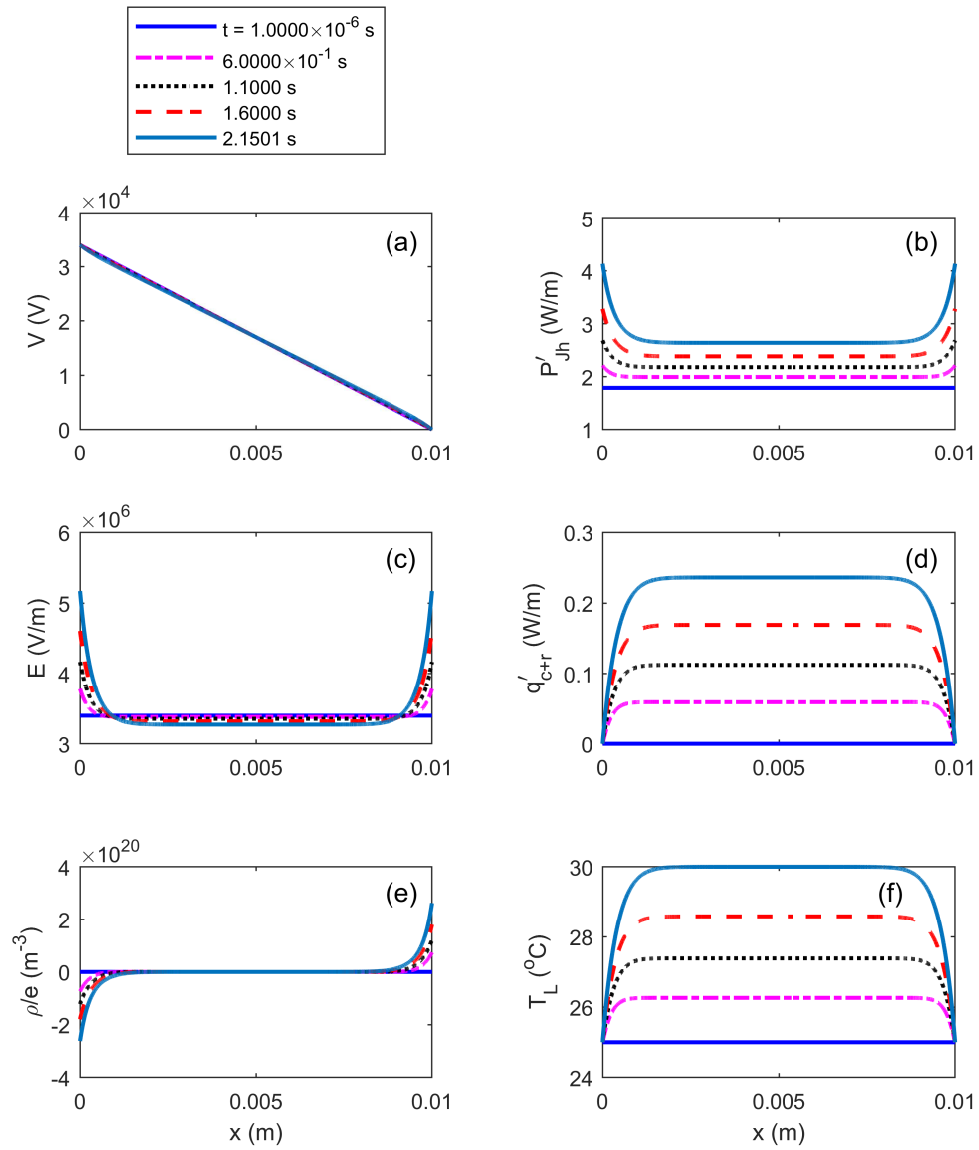
Figure 5.7: Spatial distribution and temporal evolution of various variables for wood. Parameter values: $V_{app} = 3.4 \times 10^4$ V, $L = 10^{-2}$ m, $D = 10^{-3}$ m.
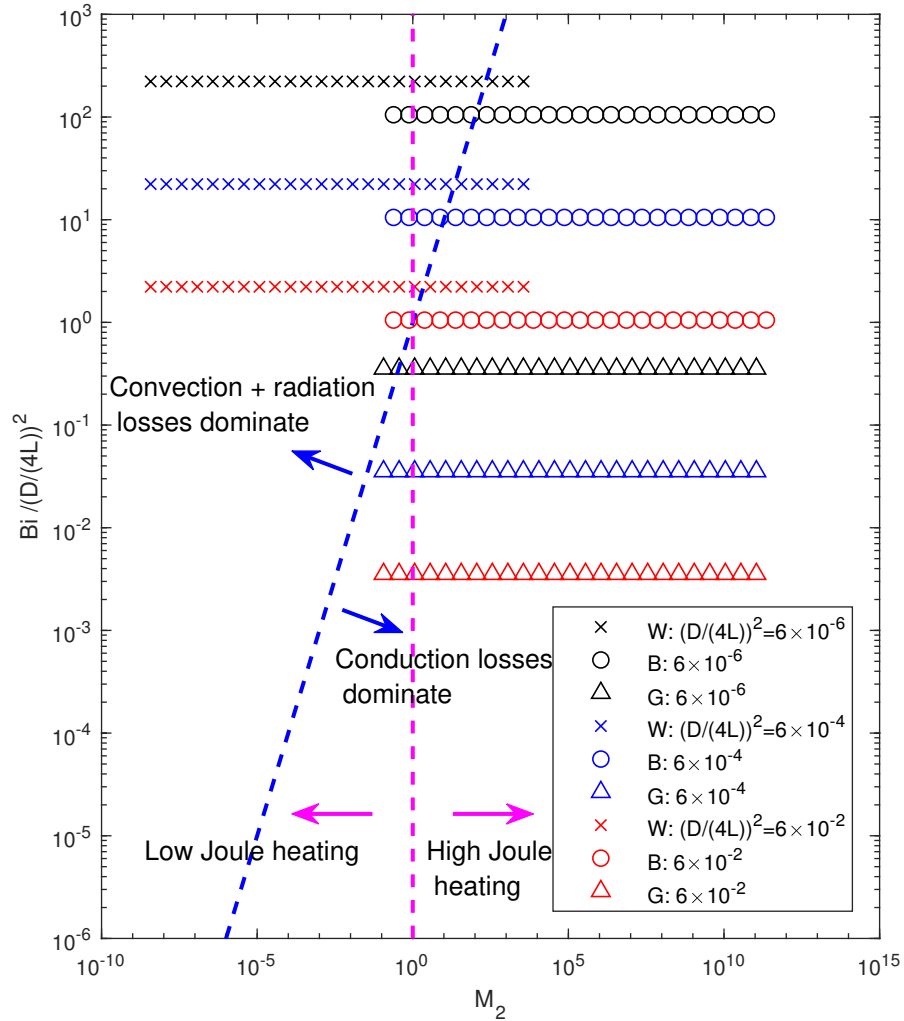
Figure 5.8: Comparison of the magnitude of the nondimensional coefficients in the energy equation (5.2c). Legend: W: Wood, B: biochar, G: graphite. $(D/(4L))^2$ is the geometric aspect ratio of the rods.

Figure 5.9 shows the relationship between Fo and M_2, where the red, blue, and black markers correspond to graphite, biochar, and wood, respectively, and where the dimensionless time needed to reach a desired $T_{L,max}$ is plotted as a function of $M_2(D/(4L))^2$. It is observed that for a prescribed $T_{L,max}$, all markers fall on a nearly straight line with a negative slope on a log-log plot. It is also seen that for a given value of $M_2(D/(4L))^2$ and for a given material, e.g., graphite, Fo increases nonlinearly with $T_{L,max}$. Lastly, for a given value of $M_2(D/(4L))^2$ and a prescribed $T_{L,max}$, Fo for biochar and wood has nearly the same value, while Fo for graphite is much lower. This means that, given a value of $M_2(D/(4L))^2$, it will take much longer for the temperature of biochar and wood to reach a certain value of $T_{L,max}$ than it will for graphite, as has been discussed in Subsections 5.7.2 through 5.7.4. Therefore, Figs. 5.8 and 5.9 are complimentary.
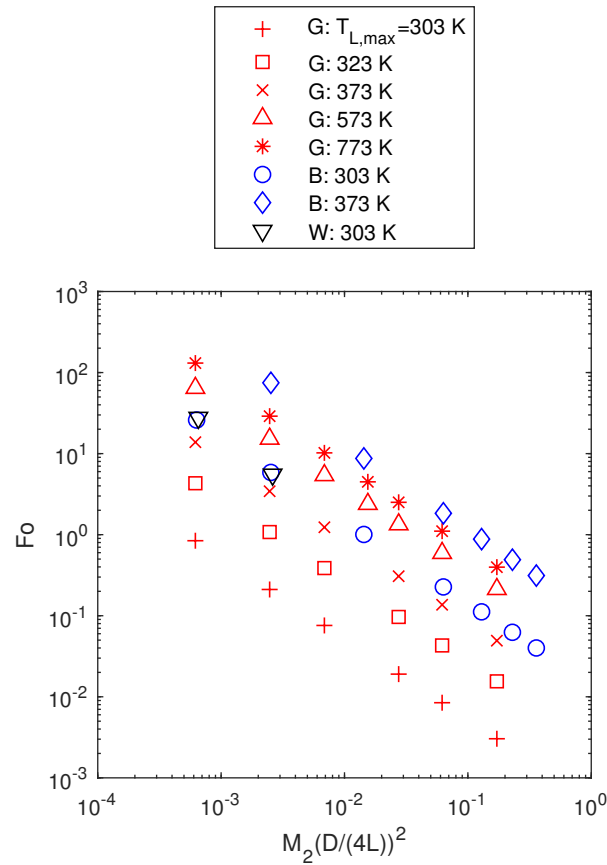
Figure 5.9: Nondimensional time Fo vs M_2 required to achieve a prescribed maximum lattice temperature $T_{L,max}$. Legend: G: graphite; B: biochar; W: wood.

For graphite, Eq. (5.12) correlates Fo and M_2 for different values of $T_{L,max} \leq$ 773 K. The error on the computed value of Fo is less than 6 % from the value obtained directly with the simulations.

$$\text{Fo}(T_{L,max}, M_2) = A(T_{L,max})M_2^{B(T_{L,max})}, \tag{5.12}$$

where the constants $A(T_{L,max})$ and $B(T_{L,max})$ depend on the maximum lattice temperature $T_{L,max}$ as follows:

$$A(T_{L,max}) = -(1.38 \times 10^{-10})T_{L,max}^3 + (2.52 \times 10^{-7})T_{L,max}^2$$
$$- (9.40 \times 10^{-6})T_{L,max} - (1.59 \times 10^{-2}), \tag{5.13}$$

and

$$B(T_{L,max}) = -(3.59 \times 10^{-8})T_{L,max}^2 - (1.91 \times 10^{-5})T_{L,max} - (9.88 \times 10^{-1}), \tag{5.14}$$

where $T_{L,max}$ is evaluated in Kelvin. Similar equations can be derived for biochar and wood, as well as other materials suitable for analysis with the present model.

5.8 Conclusions

In this chapter, a transient one-dimensional model with coupled equations for electric potential, charge conservation, and energy conservation was introduced. The model was used to analyze the dynamics of charge and heat transport leading to thermal runaway for various operating conditions using temperature-dependent properties for three different carbonaceous materials, i.e., graphite, biochar, and wood. It was found that for the materials with lower electrical conductivity, and for larger values of applied voltage, the charge accumulated mostly near the boundaries. In addition, due to the positive dependence of the electrical conductivity on temperature, the temperature increased rapidly and the dynamics of thermal runaway were observed. By performing nondimensional analyses, a plot was generated which helped visualize under which conditions significant Joule heating was prone to happen. Moreover, an equation to calculate the dimensionless time to reach a certain lattice temperature was developed for graphite. The concept of thermal runaway can be applied, for example, to biomass gasification systems, where it could help, especially during start-up conditions or for additional process control. Finally, the model only requires the input operating parameters and relevant properties, so it can be used to analyze other suitable materials.

Chapter 6

ACTIVATION OF BIOCHAR

6.1 Introduction

In the state of California there is an abundance of biomass. For example, the Central Valley is a major agricultural hub, and in addition to the main food produce, it yields an abundance of agricultural residues. Other sources of biomass include urban green waste and forest woody biomass, which has recently increased due to the mortality of millions of trees in the Sierra Nevada – which was caused by the prolonged drought, and a bark beetle infestation [69]. Dead trees in the Sierra increase the risk of fire; therefore, the state of California is planning to remove a portion of the trees to reduce the risk of fire and the spreading of the bark beetles. The state of California is seeking viable solutions and applications for the excess biomass. Gasification for electricity generation, biochar production, and biochar activation are currently being explored by different research groups and organizations.

It has become apparent that commercial success in gasification, particularly in the higher-cost forested settings depends on the sale of the biochar byproduct as much as the sale of electricity. However, with more biomass gasification plants being constructed, a rapid expansion of biochar supply is forcing the industry to create new markets for this byproduct. The focus of this work is to produce activated carbons from byproduct biochar produced in biomass gasification power plants and to assess their characteristics compared to commercially available coconut shell activated carbons. The biochar used in the experiments was obtained from a biomass gasification power plant from Phoenix Energy™, or from a commercial vendor.

This chapter continues with further information about the production, characterization techniques, and applications of activated carbons. Then, the experimental setup and procedure are provided. Finally, preliminary results of activated carbons from peach pit biochar feedstock are presented.

The preliminary results presented in this chapter have been published as Ref. [118].

6.2 Production Of Activated Carbons

Activated carbons are highly porous materials with surface functional groups that enhance the adsorption of a given adsorbate (pollutant) from a given aqueous solution or gas. Commercial activated carbons are mainly produced from two sources: coal and biomass. The former is produced in the United States from various types of coal, while the latter is produced from coconut shells – mainly in Asian countries.

The focus of the work in this chapter is in the production of activated carbon from biomass derived char, also known as biochar. At laboratory scales, biochar is typically activated using two methods: chemical activation and physical activation [63, 64]. Chemical activation consists of washing the biochar with strong chemicals such as zinc chloride, phosphoric acid, and potassium chloride. The material is then heated to temperatures below 500 °C. Physical activation can be achieved using steam or carbon dioxide at temperatures above 700 °C, generally above 800 °C for better results. Surface areas for the activated carbons can exceed 2000 m^2/g. Biochar activation by physical and chemical activation has been reviewed in Ref. [64].

There are other studies that focus on post-treatment of activated carbons with the intent of enhancing their properties for specific applications. These studies include post-treatment with microwaves, plasma discharges, and ozone [65, 119–123].

6.3 Physical Activation Parameters

There are four key parameters involved in steam activation of a given biochar: (1) activation temperature, (2) activation time, (3) steam/water flow rate, and (4) particle size range. In this analysis, the particle size range has been selected to be in the range from 0.6 to 2.36 mm. This range was selected for two main reasons: particles that are too small are easily gasified, and (b) because activation happens at the surface, much of the inner space of larger particles will not be activated.

Based on previous studies, using central composite design of experiments, it has been shown that for (the same) 3 parameters, 20 different runs are needed to fully optimize each parameter [66]. However, previous studies have been performed at various temperatures ranging from about 400 to 900 °C [66–68, 124–127], and it has been found that at temperatures below 700 °C the porosity and surface areas are relatively lower [66, 67, 125]. On the other hand, at temperatures above 850 °C, more than 50% of the biochar burns off relatively quickly, meaning that the higher surface area comes at the expense of higher mass losses. Moreover, it has been shown that at temperatures around 800 °C large surface areas and pore volumes are generally obtained for various materials [67, 68, 126], while the activation times range from about 15 to 60 minutes [67, 68]. In addition, the steam flow rates reported in recent articles also range from about 1 g/min to about 8 g/min [67, 125, 126]. Based on the published data, in this work the steam flow rate will be kept within the stated flow rates, 1 to 8 g/min. The activation temperature will be initially explored around the 800 °C, and the times varied within 15 to 75 minutes, as long as the mass losses are kept within 50%.

6.4 Characterization Of Activated Carbons

There are various characteristics of activated carbons that are of particular interest. The most common characteristic of activated carbons is their large surface area, which is typically larger than 1000 m^2/g, but can exceed 2000 m^2/g [122]. This area is referred to as the Brunauer-Emmett-Teller (BET) surface area. The BET surface area is calculated from the isotherm data and it is estimated to have an accuracy of ± 25 m^2/g [63]. Adsorption isotherms are curves obtained by plotting the amount of an adsorbed adsorbate over a range of relative pressures. They provide critical information such as pore size distribution and total/micro pore volume. Adsorption isotherms are usually obtained using nitrogen at 77 Kelvin but adsorbates such as CO_2, H_2O, and butane are also used. [63]. The iodine number is also commonly reported for commercial activated carbons.

Activated carbons are also imaged using the scanning electron microscope (SEM). SEM images allow for a visual inspection of the overall surface morphology of the carbons. Transmission electron microscope images are also used in some cases.

The ultimate/proximate analysis of the biochar and activated carbons is also usually obtained in order to compare the composition of the carbons before and after activation. In addition, the surface composition can also be obtained using x-ray diffraction spectroscopy and energy dispersive x-ray spectroscopy.

The surface functional groups such as carboxyl and carbonyl groups, are identified using Fourier transform infra red (FTIR) spectroscopy and the Boehm titration method [63, 67]. The surface chemistry or reactivity of the activated carbons will be enhanced by different groups.

In addition, the pH is also an important metric.

6.5 Physical Activation With Superheated Steam
6.5.1 Experimental setup

A schematic of the experimental setup for superheated steam activation is shown in Fig. 6.1. A vertical tube furnace with a maximum operating temperature of 1200 °C, and 24 in. heated length is used. A high temperature stainless steel (310S) work-tube with an inner diameter (ID) of 2.01 in. and flanges at both ends is placed inside the furnace. Inside the work-tube, a 2 in. outer diameter (OD) coil made with 3 mm OD 310S stainless steel tube extends from the beginning (bottom) of the heated region of the furnace to approximately 18 in. up into the heated region. It then connects to a 2 in. OD reactor, where the biochar is placed during the activation process. The reactor is 18 in. long and sits at the top of the work tube. It extends down to about 7 inches into the heated portion of the furnace, where it connects to the coil. The reactor has an end-cap at the top, into which an 18 in. long thermocouple is inserted; it measures the actual temperature near the biochar. In addition, a foot long, 1/4 in. pipe is connected to the reactor end-cap. The gases coming out from the activation process are flared at the end of the pipe. At the inlet (bottom) of the coil, a 1/4 in. OD stainless steel tube is attached, which extends well below the bottom of the work tube. Towards the bottom end of the 1/4 in. OD
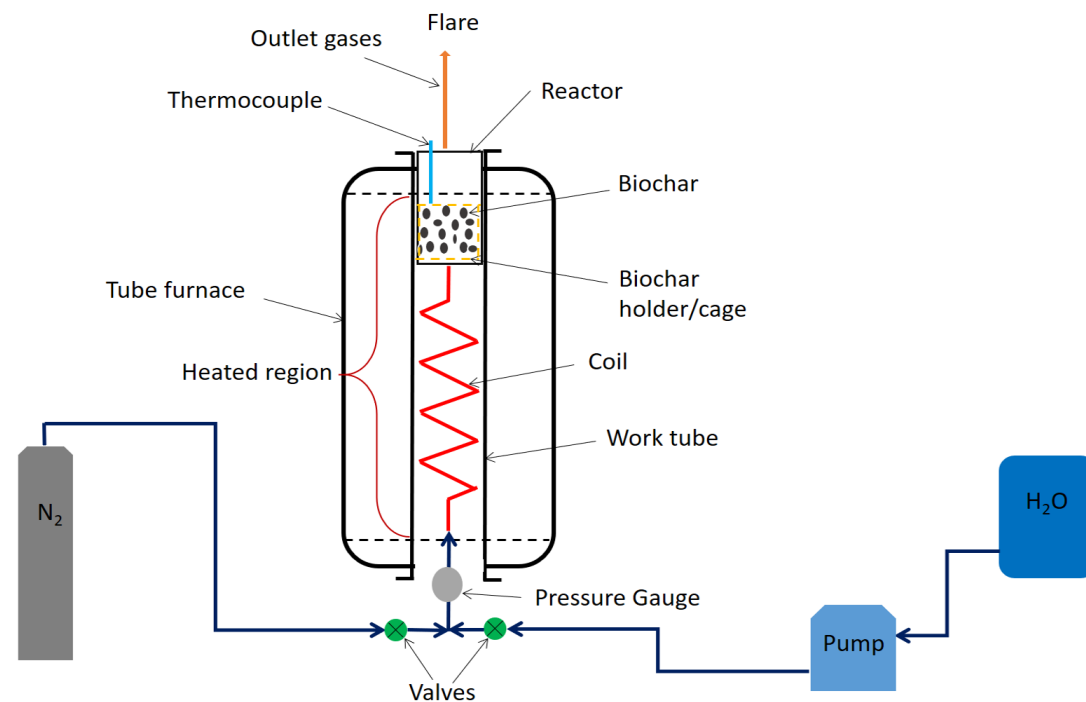
Figure 6.1: Schematic representation of the biochar activation experimental setup.

tube, a pressure gauge is connected and then the tube ends at a tee. One end of the tee receives a nitrogen line, while the other end receives a water line. The water line is fed by a high-pressure low-flow water pump. Deionized water is used for the experiments, which is stored in a container to feed the pump. On the other side of the tee, the nitrogen is fed from a nitrogen tank. A picture of the experimental setup is shown in Fig. 6.2.

6.5.2 Procedure

Biochar sample preparation: Peach pit biochar was selected due to its local availability. This is byproduct biochar produced from the biomass gasification process at, and donated by, Phoenix Energy™. It is sieved to the proper size range, 0.6 to 2.36 mm, and dried in an oven for 8 hours at 105 °C. A sample of 20 grams of the sieved, dried biochar is used for each activation run.

Physical activation procedure: Large scale physical activation of biochar occurs in large kilns where the input biochar is transported in conveyor belts and dropped inside the reactor which operates between 800 and 1000°C. Therefore, the material experiences a very high rate of heating from near ambient conditions to the temperature of the activation process. Our laboratory procedure intends to mimic this large heating rate by placing a biochar sample at ambient temperature inside a furnace operating at steam activation temperature. The experimental procedure is as follows: the furnace is preset and heats up to the activation temperature at a maximum

Figure 6.2: Biochar activation experimental setup.

rate of 8 °C/min. Once the furnace reaches the activation temperature, the water pump is turned on at the desired flow rate to initiate the production of superheated steam. After about 30 minutes, the reactor where the biochar sample is placed, also reaches the set furnace temperature. This happens since the reactor temperature always lags the furnace temperature due to thermal inertia. At this time, the water pump is turned off, the reactor end-cap is taken off, and the biochar sample is quickly placed inside the reactor. Then the reactor is closed and the pump is switched back on. Also, a propane torch is fired up to flare the outflowing gases. All these steps are performed in approximately 30 seconds. Because the thermocouple is attached to the end-cap, which is removed temporarily while inserting the biochar into the reactor, the temperature reading falls well below the furnace temperature, however, as soon as the thermocouple is re-inserted, the temperature reading goes back up close to the furnace temperature and eventually reaches the same value. The temperature profile is recorded for all the experiments, and a log-mean-temperature is used to refer to an average activation temperature, which is close to the set furnace temperature. Upon completion of the activation process, the water flow is stopped. At this time, nitrogen flow is initiated, and runs continuously thereafter while the activated carbon sample cools down to a temperature around 200 °C. The sample is taken out of the reactor at low temperatures to avoid instantaneous combustion of the biochar.

This process replicates what is done in industry more closely. Alternatively, the biochar could be placed in the reactor when the furnace is turned on, and nitrogen could flow during the heating process, as is typically done in laboratory experiments.

6.6 Results

The ultimate and proximate analyses for raw biochar and for an activated sample (dark blue marker on Fig. 6.5) are shown in Tab. 6.1. The sample was activated with a furnace temperature of 800 °C and a steam flow rate of 0.8 g/min for 30 minutes.

The material loss due to the steam activation process is usually referred to as burn off %. Equation 6.1 describes the way that the burn off percentage is calculated.

$$\text{Burn off \%} = \frac{\text{initial mass} - \text{final mass}}{\text{initial mass}} \times 100\% \qquad (6.1)$$

Figure 6.3 shows the burn off percentage with respect to activation time for peach pit biochar samples exposed to different operating temperatures and steam flow rates. Operating temperatures range between 800°C to 850°C and the mass flow rates of steam are in the range between 0.8 g/min and 4.3 g/min. It is observed that high burn off percentages were obtained at high mass flow rates of steam, high temperature, and longer activation times. High loss of mass is economically detrimental for large-scale production of activated carbon. Figure 6.4 shows the BET surface area for the treated biochar samples and one raw biochar sample. It is observed that the raw biochar sample (in dark blue) has a surface area of less than 1 m^2/g, which shows the low

Table 6.1: Properties of raw and activated peach pit biochar.

	Raw biochar	Activated biochar
Proximate Analysis (wt %, dry basis)		
Ash	21.24	35.00
Volatile matter	23.78	5.04
Fixed carbon	54.98	59.96
Ultimate Analysis (wt %, dry basis)		
Carbon	65.62	63.17
Hydrogen	2.33	<0.10
Nitrogen	0.57	0.32
Oxygen (by difference)	10.12	1.44
Chlorine	0.10	0.05
Sulfur	0.02	0.02

capability of being used as a filtering material. On the other hand, BET surface areas near 600 m^2/g were obtained with 810°C and a mass flow rate of steam of 4.3 g/min for activation times of 40 and 70 minutes, shown in grey color. It is noted that high flow rate of steam and higher operating temperatures translate into higher energy consumption to produce activated carbon. The figure also shows a green marker that corresponds to the BET surface area for a case where low heating rate was utilized on the biochar sample by slowly reaching steam activation temperatures with the biochar sample inside the reactor under nitrogen flow. Once the steam activation temperature was reached, the nitrogen flow was stopped and steam flow was started. The aspect of energy consumption to produce activated carbon is shown in Fig. 6.5, where the BET surface area has been multiplied by fraction of mass left after the activation process and divided by the energy used to produce the treated biochar sample. It is observed that the samples with high steam flow rate and activation times are at the bottom of the group, which means that it is very energy intensive to produce these samples. On the other hand, even though the blue marker, produced with 800°C, 0.8 g/min of steam mass flow rate, and 30 minutes of activation time, reached only 513 m^2/g of BET surface area, it is a good compromise between surface area per energy used in the process. The SEM picture of the sample with a blue marker is shown in Fig. 6.6 which characterizes the surface geometry that features a mean pore size of 20.7 Å and a total pore volume of 0.27 cm^3/g. It is noted that the burn off percentage of this sample was only 30.2%.

6.7 Conclusions

The abundance of agriculture and forest biomass is forcing the search for ways to process this material in an environmentally conscious way. Biomass gasification

Figure 6.3: Burn off % vs. activation time for different steam flow rates and furnace temperatures. Legend: FT: Furnace temperature; SFR: Steam flow rate; N2: Nitrogen.

produces synthesis gas that can be used for the production of power and/or heat, but it also produces a byproduct called biochar. Research is currently being performed to find ways to utilize this material. Steam activation is one path for potentially using this material in industrial filters. In this work, several tests were performed to analyze the BET surface characteristics of steam activated biochar from peach pits. It is shown that raw biochar has a very low surface area but it can be augmented several orders of magnitude after physical activation. A compromise of surface area is reached by minimizing operating temperature, steam flow rate, and activation time.

In addition to these results, physical activation of ponderosa pine biochar is being investigated. Results show surface areas with values up to 738 m^2/g. These results are very promising, therefore, more experiments are being carried out. Also, these results will serve as a benchmark to compare to plasma activated samples. This work will be published elsewhere.
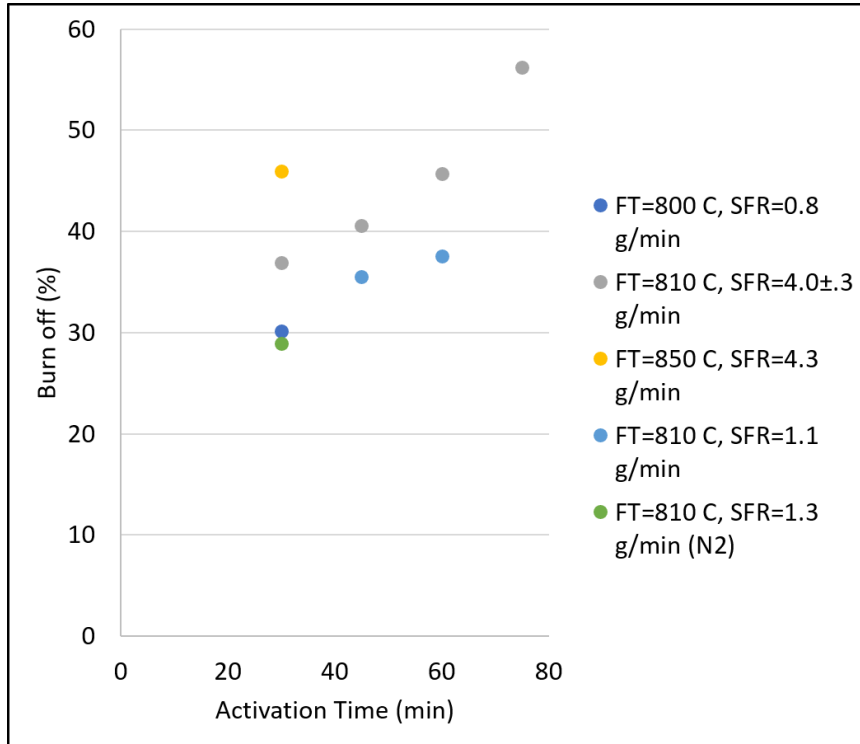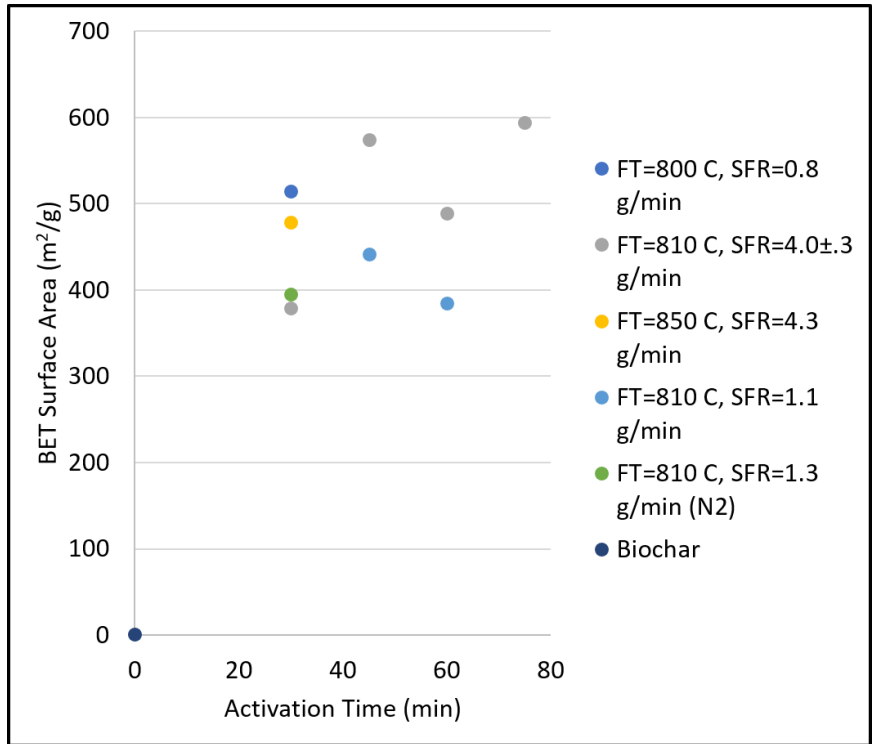
Figure 6.4: BET surface area vs. activation time for different steam flow rates and furnace temperatures. Legend: FT: Furnace temperature; SFR: Steam flow rate; N2: Nitrogen.
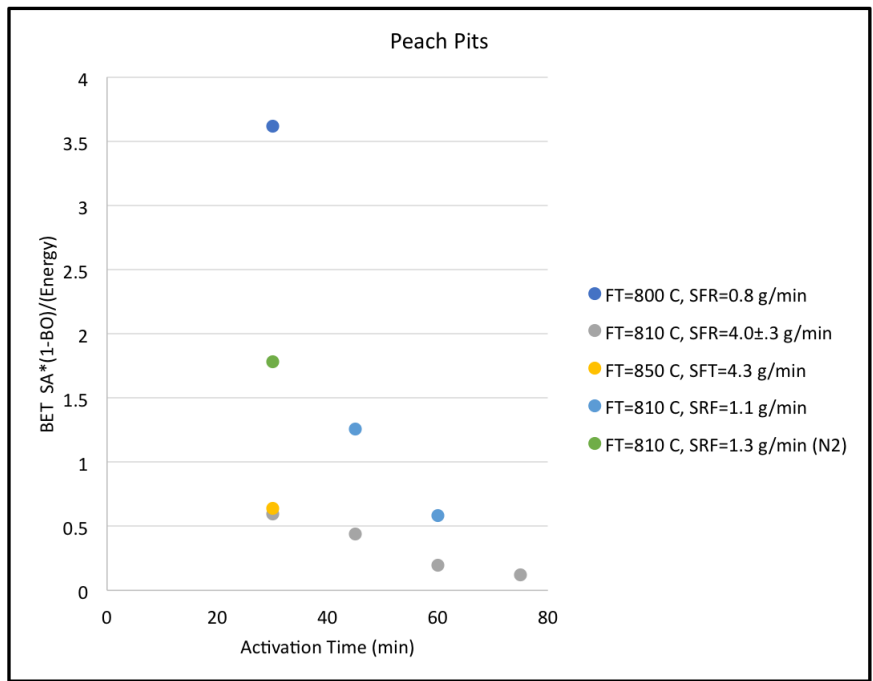
Figure 6.5: BET surface area per energy used in the process.
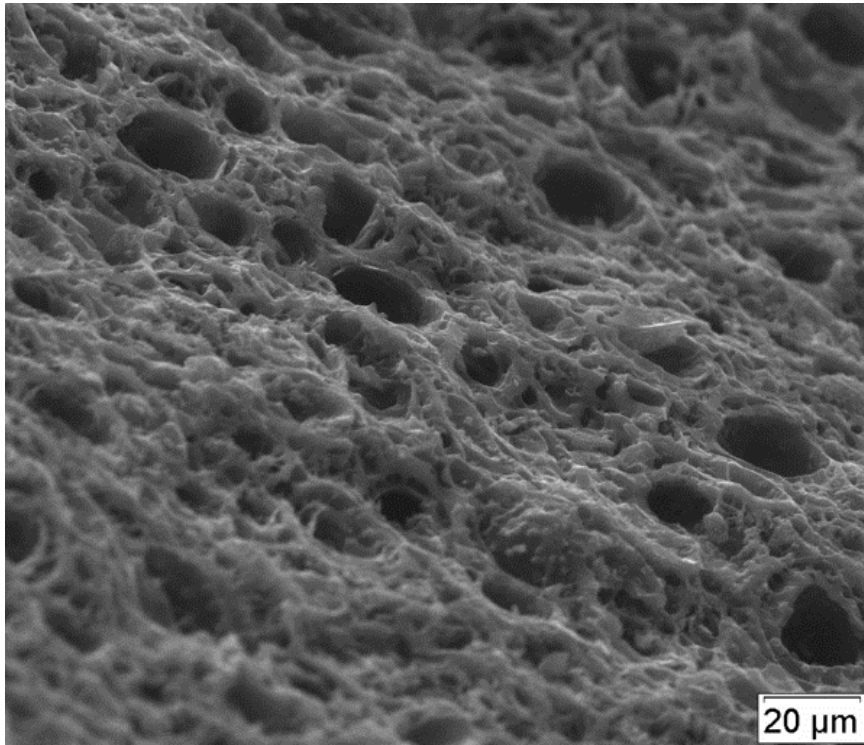
Figure 6.6: Scanning electron microscope image of activated biochar sample.

Chapter 7

CONCLUSIONS AND FUTURE WORK

The abundance of biomass in California has forced the search for new markets and more environmental friendly processes. The work on this dissertation aims to address both issues. Part of the work in this dissertation, using numerical simulations, explored Joule heating as a technique to induce thermal breakdown of carbonaceous materials and obtain high temperatures using low power. The simulations showed that thermal breakdown has the potential to be used to enhance biomass gasification. These results serve as motivation to further explore this concept experimentally. In addition, physical activation of biochar was achieved. Though the surface area values of preliminary samples were significantly lower than commercial activated carbons, the results are promising to continue analyzing more feedstock and to determine optimal activation parameters.

The concept of Joule heating-induced thermal breakdown was inspired because of its potential applicability in biomass gasification power plants. Nonetheless, the drift-diffusion and hydrodynamic models of Chapters 3 and 4, respectively, have been historically applied to inorganic semiconductor devices, though, more recently, they have been applied to organic semiconductors and graphene devices. The use of these models was motivated by the need to obtain a more in-depth fundamental understanding of charge carrier and Joule heat transport in solid materials. Due to the nature of these models, their use was restricted to graphite. In Chapter 3, the drift-diffusion model was successfully used to determine electron/hole densities and velocities, and the lattice temperature distribution – among other results – for different operating conditions. In Chapter 4, a more complete hydrodynamic model was developed, as well as, a numerical scheme to solve it. The work of Chapter 4 was inspired by the successful use of the drift-diffusion model to analyze graphite. The hydrodynamic model in Chapter 4 is less restrictive than the drift-diffusion model from Chapter 3; thus, it can be used to explore smaller devices, extend the operating conditions, and explore the effect of different properties and parameters. In addition,

this model could be used to analyze multilayer graphene devices – a field undergoing intense research.

Variations of the electric-thermal model in Chapter 5 were developed for the purpose of better understanding thermal runaway, which ultimately leads to thermal breakdown. Historically, this model has been mostly used to prevent thermal breakdown of insulating materials, such as polymers. In contrast, in this dissertation, this model was used to better understand thermal runaway conditions and exploit its aggressive nature to reach high temperatures in short amounts of time. While this model is simple, it is very versatile as it can be used to analyze any material regardless of structure; therefore, it was used to analyze three very different materials: graphite, biochar, and wood. The results from this model suggest that this method has the potential to be used in biomass gasification systems. Joule heating-induced thermal breakdown creates high temperatures which could be used to provide some of the heat that is needed during pyrolysis. Hence, it decreases the need to allow partial combustion, which reduces the heating value of the product gases. Nonetheless, experimental results should be performed to further explore this concept. Overall, the numerical results motivate future research in which the experiments are carried out.

In Chapter 6, the activation of post-gasification biochar was explored using physical activation with superheated steam. Both the experimental setup and procedure were developed as part of the work in this dissertation. Preliminary activated samples from peach pit biochar showed promising results. The BET surface area of the best samples reached values near 600 m^2/g. While this number is significantly lower than the surface area of commercial activated carbons, the surface area of other feedstock could be higher. In addition, larger surface areas could be obtained by optimizing the process for the best feedstock. As a result, more research is being performed using other biochar feedstock. Moreover, the activation process is being streamlined, and optimum activation conditions for different types of biochar are under investigation.

In addition, experiments are being performed to investigate the use of plasma discharges as a method to enhance biochar activation. The results are being analyzed and compared against the results with physical activation. Ponderosa pine biochar is being used for this purpose. These results will be published elsewhere.

Other ongoing and near-future research include the activation of other biochar feedstock. In addition, the activated biochar samples with the highest BET surface areas will be subjected to specific applications to assess their performance. For example, activated carbons with the capability to adsorb hydrogen sulfide is of great interest to the wastewater treatment community. Thus, determining if activated biochar is suitable for this application is of great interest.

BIBLIOGRAPHY

[1] F. Paschen, Ueber die zum funkenübergang in luft, wasserstoff und kohlensäure bei verschiedenen drucken erforderliche potentialdifferenz, Annalen der Physik 273 (5) (1889) 69–96.

[2] C. Zener, A theory of the electrical breakdown of solid dielectrics, Proceedings of the Royal Society of London. Series A, Containing Papers of a Mathematical and Physical Character 145 (855) (1934) 523–529.

[3] S. Whitehead, W. Nethercot, The breakdown of dielectrics under high voltage, with particular reference to thermal instability, Proceedings of the Physical Society 47 (5) (1935) 974.

[4] H. Fröhlich, Theory of electrical breakdown in ionic crystals, Proceedings of the Royal Society of London. Series A, Mathematical and Physical Sciences 160 (901) (1937) 230–241.

[5] A. Von Hippel, Ergeb. exakt naturwiss., 14, 118 (1935), Z. Phys 98 (1936) 580.

[6] A. Von Hippel, Electric breakdown of solid and liquid insulators, Journal of Applied Physics 8 (12) (1937) 815–832.

[7] A. Von Hippel, Electronic conduction in insulating crystals under very high field strength, Physical Review 54 (12) (1938) 1096.

[8] R. Buehl, A. Von Hippel, The electrical breakdown strength of ionic crystals as a function of temperature, Physical Review 56 (9) (1939) 941.

[9] A. Von Hippel, R. Maurer, Electric breakdown of glasses and crystals as a function of temperature, Physical Review 59 (10) (1941) 820.

[10] A. Von Hippel, G. Lee, Scattering, trapping, and release of electrons in nacl and in mixed crystals of nacl and agcl, Physical Review 59 (10) (1941) 824.

[11] A. Von Hippel, C. breakdown. electric breakdown of solid dielectrics, Transactions of the Faraday Society 42 (1946) A078–A087.

[12] H. Fröhlich, On the theory of dielectric breakdown in solids, Proceedings of the Royal Society A 188 (1015) (1947) 521–532.

[13] A. Von Hippel, R. Alger, Breakdown of ionic crystals by electron avalanches, Physical Review 76 (1) (1949) 127.

[14] S. Whitehead, Dielectric breakdown of solids, Clarendon Press, 1951.

[15] J. J. O'Dwyer, Dielectric breakdown in solids, Advances in Physics 7 (27) (1958) 349–394.

[16] J. J. O'Dwyer, Current-voltage characteristics of dielectric films, Journal of Applied Physics 37 (2) (1966) 599–601.

[17] S. M. Sze, Current transport and maximum dielectric strength of silicon nitride films, Journal of Applied Physics 38 (7) (1967) 2951–2956.

[18] J. J. O'dwyer, The theory of avalanche breakdown in solid dielectrics, Journal of Physics and Chemistry of Solids 28 (7) (1967) 1137–1144.

[19] J. J. O'Dwyer, Theory of dielectric breakdown in solids, Journal of The Electrochemical Society 116 (2) (1969) 239–242.

[20] N. Klein, Electrical breakdown in thin dielectric films, Journal of The Electrochemical Society 116 (7) (1969) 963–972.

[21] N. Klein, Electrical breakdown in solids, Advances in electronics and electron physics 26 (1969) 309–424.

[22] J. J. O'Dwyer, The theory of electrical conduction and breakdown in solid dielectrics, Clarendon Press Oxford, 1973.

[23] P. P. Budenstein, On the mechanism of dielectric breakdown of solids, IEEE Transactions on Electrical Insulation (3) (1980) 225–240.

[24] M. Hikita, M. Nagao, G. Sawa, M. Ieda, Dielectric breakdown and electrical conduction of poly (vinylidene-fluoride) in high temperature region, Journal of Physics D: Applied Physics 13 (4) (1980) 661.

[25] M. Hikita, M. Nagao, G. Sawa, M. Ieda, Thermal breakdown form and heat transfer coefficient in insulator, Electrical Engineering in Japan 101 (5) (1981) 20–23.

[26] M. Hikita, A. Matsuda, M. Nagao, G. Sawa, M. Ieda, Electrical breakdown of plasma-polymerized styrene thin films, Japanese Journal of Applied Physics 21 (3R) (1982) 475.

[27] M. Hikita, A. Matsuda, M. Nagao, G. Sawa, M. Ieda, A model for dielectric breakdown in plasma-polymerized styrene thin films, Japanese Journal of Applied Physics 21 (3R) (1982) 483.

106

[28] M. Hikita, M. Ieda, G. Sawa, Numerical analysis of steady-state thermal break-down, Journal of Applied Physics 54 (4) (1983) 2025–2029.

[29] M. Hikita, S. Tajima, I. Kanno, I. Ishino, G. Sawa, M. Ieda, High-field conduction and electrical breakdown of polyethylene at high temperatures, Japanese journal of applied physics 24 (8R) (1985) 988.

[30] M. Nagao, T. Kitamura, Y. Mizuno, M. Kosaki, M. Ieda, Localized heat generation before dielectric breakdown of polyethylene films, in: Conduction and Breakdown in Solid Dielectrics, 1989., Proceedings of the 3rd International Conference on, IEEE, 1989, pp. 77–81.

[31] T. Mizutani, M. Ieda, Electrical conduction in solid dielectrics, IEEE transactions on electrical insulation (6) (1986) 833–839.

[32] M. Noskov, A. Cheglokov, A. Shapovalov, Dynamics of the thermal instability evolution in dielectric breakdown, Russian Physics Journal 44 (1) (2001) 48–54.

[33] H. Neff, A. Lima, E. Melcher, C. Moreira, A. B. Neto, J. Precker, An electro-thermal approach to dielectric breakdown in solids: application to crystalline polymer insulators, IEEE Transactions on Dielectrics and Electrical Insulation 17 (3) (2010) 872–880.

[34] N. Jyothi, T. Ramu, M. Mandlik, Temperature distribution in resin impregnated paper insulation for transformer bushings, IEEE Transactions on Dielectrics and Electrical Insulation 17 (3).

[35] G. Brandao, L. De Almeida, G. Deep, A. Lima, H. Neff, Stability conditions, nonlinear dynamics, and thermal runaway in microbolometers, Journal of Applied Physics 90 (4) (2001) 1999–2008.

[36] Y. G. Yune, M. D. Bryant, Transient nonlinear thermal runaway effects in carbon graphite electrical brushes, IEEE Transactions on Components, Hybrids, and Manufacturing Technology 11 (1) (1988) 91–100.

[37] E. Pop, D. A. Mann, K. E. Goodson, H. Dai, Electrical and thermal transport in metallic single-wall carbon nanotubes on insulating substrates, Journal of Applied Physics 101 (9) (2007) 093710.

[38] C. Durkan, Z. Xiao, On the failure of graphene devices by joule heating under current stressing conditions, Applied Physics Letters 107 (24) (2015) 243505.

[39] M. A. Kuroda, A. Cangellaris, J.-P. Leburton, Nonlinear transport and heat dissipation in metallic carbon nanotubes, Physical review letters 95 (26) (2005) 266803.

[40] M.-H. Bae, Z.-Y. Ong, D. Estrada, E. Pop, Imaging, simulation, and electrostatic control of power dissipation in graphene devices, Nano letters 10 (12) (2010) 4787–4793.

[41] M. Freitag, H.-Y. Chiu, M. Steiner, V. Perebeinos, P. Avouris, Thermal infrared emission from biased graphene, Nature nanotechnology 5 (7) (2010) 497–501.

[42] M.-H. Bae, S. Islam, V. E. Dorgan, E. Pop, Scaling of high-field transport and localized heating in graphene transistors, ACS nano 5 (10) (2011) 7936–7944.

[43] E. Knapp, B. Ruhstaller, Analysis of negative capacitance and self-heating in organic semiconductor devices, Journal of Applied Physics 117 (13) (2015) 135501.

[44] R. Stratton, Diffusion of hot and cold electrons in semiconductor barriers, Physical Review 126 (6) (1962) 2002.

[45] S. M. Sze, K. K. Ng, Physics of semiconductor devices, John Wiley & Sons, 2006.

[46] M. Lundstrom, Fundamentals of carrier transport, Cambridge University Press, 2009.

[47] C. T. Wang, A new set of semiconductor equations for computer simulation of submicron devices, Solid-state electronics 28 (8) (1985) 783–788.

[48] J. W. ROBERTS, S. G. CHAMBERLAIN, Energy-momentum transport model suitable for small geometry silicon device simulation, COMPEL-The international journal for computation and mathematics in electrical and electronic engineering 9 (1) (1990) 1–22.

[49] A. Majumdar, K. Fushinobu, K. Hijikata, Heat generation and transport in submicron semiconductor devices, Journal of Heat transfer 117 (1995) 25–31.

[50] J. Lai, A. Majumdar, Concurrent thermal and electrical modeling of sub-micrometer silicon devices, Journal of Applied Physics 79 (9) (1996) 7353–7361.

[51] T. Grasser, T.-W. Tang, H. Kosina, S. Selberherr, A review of hydrodynamic and energy-transport models for semiconductor device simulation, Proceedings of the IEEE 91 (2) (2003) 251–274.

[52] R. O. Grondin, S. M. El-Ghazaly, S. Goodnick, A review of global modeling of charge transport in semiconductors and full-wave electromagnetics, IEEE transactions on microwave theory and techniques 47 (6) (1999) 817–829.

[53] Z. B. Van, Principles of semiconductor devices, Colorado University, 2011. URL http://ecee.colorado.edu/~bart/book/

[54] New semiconductors materials. characteristics and properties. (2001).
URL http://www.ioffe.ru/SVA/NSM/Semicond/

[55] K. Bløtekjær, Transport equations for electrons in two-valley semiconductors, IEEE Transactions on Electron Devices 17 (1) (1970) 38–47.

[56] A. W. Smith, K. F. Brennan, Hydrodynamic simulation of semiconductor devices, Progress in quantum electronics 21 (4) (1998) 293–360.

[57] K. Mohseni, A. Shakouri, R. J. Ram, M. C. Abraham, Electron vortices in semiconductors devices a, Physics of Fluids 17 (10) (2005) 100602.

[58] A. Jonscher, Transport of hot injected plasmas in semiconductors, Proceedings of the Physical Society 84 (5) (1964) 767.

[59] J. I. Osses-Márquez, W. R. Calderón-Muñoz, Thermal influence on charge carrier transport in solar cells based on gaas pn junctions, Journal of Applied Physics 116 (15) (2014) 154502.

[60] N. Aluru, A. Raefsky, P. Pinsky, K. Law, R. Goossens, R. Dutton, A finite element formulation for the hydrodynamic semiconductor device equations, Computer methods in applied mechanics and engineering 107 (1-2) (1993) 269–298.

[61] A. Majumdar, K. Fushinobu, K. Hijikata, Effect of gate voltage on hot-electron and hot phonon interaction and transport in a submicrometer transistor, Journal of Applied Physics 77 (12) (1995) 6686–6694.

[62] V. Romano, A. Rusakov, 2d numerical simulations of an electron–phonon hydrodynamical model based on the maximum entropy principle, Computer Methods in Applied Mechanics and Engineering 199 (41-44) (2010) 2741–2751.

[63] H. Marsh, F. R. Reinoso, Activated carbon, Elsevier, 2006.

[64] O. Ioannidou, A. Zabaniotou, Agricultural residues as precursors for activated carbon productiona review, Renewable and Sustainable Energy Reviews 11 (9) (2007) 1966–2005.

[65] A. Bhatnagar, W. Hogland, M. Marques, M. Sillanpää, An overview of the modification methods of activated carbon for its water treatment applications, Chemical Engineering Journal 219 (2013) 499–511.

[66] R. Azargohar, A. Dalai, Steam and koh activation of biochar: Experimental and modeling studies, Microporous and Mesoporous Materials 110 (2) (2008) 413–421.

[67] H. Demiral, İ. Demiral, B. Karabacakoğlu, F. Tümsek, Production of activated carbon from olive bagasse by physical activation, Chemical Engineering Research and Design 89 (2) (2011) 206–213.

[68] J. Alvarez, G. Lopez, M. Amutio, J. Bilbao, M. Olazar, Physical activation of rice husk pyrolysis char for the production of high surface area activated carbons, Industrial & Engineering Chemistry Research 54 (29) (2015) 7241–7250.

[69] Tree mortality task force monthly update june 30, 2017, Tech. rep., Tree Mortality Task Force (2017).
URL http://www.fire.ca.gov/treetaskforce/downloads/TMTFMaterials/June_2017_TMTF_Monthly_Update.pdf

[70] U. Lindefelt, Heat generation in semiconductor devices, Journal of Applied Physics 75 (2) (1994) 942–957.

[71] T. Nitschke, D. Graves, A comparison of particle in cell and fluid model simulations of low-pressure radio frequency discharges, Journal of applied physics 76 (10) (1994) 5646–5660.

[72] J. Shi, M. G. Kong, Cathode fall characteristics in a dc atmospheric pressure glow discharge, Journal of applied physics 94 (9) (2003) 5504–5513.

[73] A. Lebouvier, C. Delalondre, F. Fresnet, F. Cauneau, L. Fulcheri, 3d mhd modelling of low current–high voltage dc plasma torch under restrike mode, Journal of Physics D: Applied Physics 45 (2) (2011) 025204.

[74] W. R. Calderón-Muñoz, Linear stability of electron-flow hydrodynamics in ungated semiconductors, Ph.D. thesis, University of Notre Dame (2009).

[75] M. A. Lieberman, A. J. Lichtenberg, Principles of plasma discharges and materials processing, John Wiley & Sons, 2005.

[76] E. Azoff, Generalized energy-momentum conservation equations in the relaxation time approximation, Solid-state electronics 30 (9) (1987) 913–917.

[77] R. K. Cook, Numerical simulation of hot-carrier transport in silicon bipolar transistors, IEEE Transactions on Electron Devices 30 (9) (1983) 1103–1110.

[78] L. Ballestra, S. Micheletti, R. Sacco, Semiconductor device simulation using a viscous-hydrodynamic model, Computer methods in applied mechanics and engineering 191 (47-48) (2002) 5447–5466.

[79] C. A. Klein, Pyrolytic graphites: their description as semimetallic molecular solids, Journal of Applied Physics 33 (11) (1962) 3338–3357.

[80] C. A. Klein, Stb model and transport properties of pyrolytic graphites, Journal of Applied Physics 35 (10) (1964) 2947–2957.

[81] W. L. James, Dielectric properties of wood and hardboard: Variation with temperature, frequency, moisture content, and grain orientation., Tech. Rep. FPL-245, U.S. Department of Agriculture, Forest Service, Forest Products Laboratory, Madison, WI (1975).

[82] C. Skaar, Wood-water relations, Springer Verlag, 1988.

[83] M. A. Dietenberger, D. W. Green, D. E. Kretschmann, et al., Wood handbook-wood as an engineering material, Tech. Rep. FPL-GTR113, Madison, WI: U.S. Department of Agriculture, Forest Service, Forest Products Laboratory (March 1999).

[84] S. L. Zelinka, D. S. Stone, D. R. Rammer, Equivalent circuit modeling of wood at 12% moisture content, Wood and fiber science 39 (4) (2007) 556–565.

[85] L. Parfen'eva, T. Orlova, N. Kartenko, B. Smirnov, I. Smirnov, H. Misiorek, A. Jezowski, J. Muha, M. Vera, Structure, electrical resistivity, and thermal conductivity of beech wood biocarbon produced at carbonization temperatures below 1000 °C, Physics of the Solid State 53 (11) (2011) 2398–2407.

[86] J. H. Kwon, S. B. Park, N. Ayrilmis, S. W. Oh, N. H. Kim, Effect of carbonization temperature on electrical resistivity and physical properties of wood and wood-based composites, Composites Part B: Engineering 46 (2013) 102–107.

[87] M. Kumar, R. Gupta, Electrical resistivity of acacia and eucalyptus wood chars, Journal of materials science 28 (2) (1993) 440–444.

[88] Entegris, Properties and characteristics of graphite, Tech. rep., Entegris, Inc. (January 2015).
URL http://poco.com/Portals/0/Literature/Semiconductor/IND-109441-0115.pdf

[89] P. R. Wallace, The band theory of graphite, Physical Review 71 (9) (1947) 622.

[90] G. H. Kinchin, The electrical properties of graphite, Proceedings of the Royal Society of London. Series A. Mathematical and Physical Sciences 217 (1128) (1953) 9–26.

[91] J. McClure, Band structure of graphite and de haas-van alphen effect, Physical Review 108 (3) (1957) 612.

[92] J. McClure, Energy band structure of graphite, IBM Journal of Research and Development 8 (3) (1964) 255–261.

[93] J. McClure, Analysis of multicarrier galvanomagnetic data for graphite, Physical Review 112 (3) (1958) 715.

[94] D. Soule, Magnetic field dependence of the hall effect and magnetoresistance in graphite single crystals, Physical Review 112 (3) (1958) 698.

[95] D. Soule, Analysis of galvanomagnetic de haas-van alphen type oscillations in graphite, Physical Review 112 (3) (1958) 708.

[96] A. Muñoz-Hernández, G. Diaz, W. R. Calderón-Muñoz, E. Leal-Quiros, Thermal-electric modeling of graphite: Analysis of charge carrier densities and joule heating of intrinsic graphite rods, Journal of Applied Physics 122 (24) (2017) 245107.

[97] T. L. Bergman, F. P. Incropera, D. P. DeWitt, A. S. Lavine, Fundamentals of heat and mass transfer, John Wiley & Sons, 2011.

[98] M. Breusing, C. Ropers, T. Elsaesser, Ultrafast carrier dynamics in graphite, Physical review letters 102 (8) (2009) 086809.

[99] I. Volovichev, J. Velazquez-Perez, Y. G. Gurevich, Transport boundary conditions for solar cells, Solar Energy Materials and Solar Cells 93 (1) (2009) 6–10.

[100] C. Y. Ho, R. W. Powell, P. Liley, Thermal conductivity of the elements, Journal of Physical and Chemical Reference Data 1 (2) (1972) 279–421.

[101] G. Fugallo, A. Cepellotti, L. Paulatto, M. Lazzeri, N. Marzari, F. Mauri, Thermal conductivity of graphene and graphite: collective excitations and mean free paths, Nano letters 14 (11) (2014) 6109–6114.

[102] X. Hong, D. Chung, Exfoliated graphite with relative dielectric constant reaching 360, obtained by exfoliation of acid-intercalated graphite flakes without subsequent removal of the residual acidity, Carbon 91 (2015) 1–10.

[103] K. R. Chandran, Transient joule heating of graphene, nanowires and filaments: Analytical model for current-induced temperature evolution including substrate and end effects, International Journal of Heat and Mass Transfer 88 (2015) 14–19.

[104] M. Freitag, M. Steiner, Y. Martin, V. Perebeinos, Z. Chen, J. C. Tsang, P. Avouris, Energy dissipation in graphene field-effect transistors, Nano letters 9 (5) (2009) 1883–1888.

[105] W. R. Calderón-Muñoz, D. Jena, M. Sen, Temperature influence on hydrodynamic instabilities in a one-dimensional electron flow in semiconductors, Journal of applied physics 107 (7) (2010) 074504.

[106] M. Dyakonov, M. Shur, Shallow water analogy for a ballistic field effect transistor: New mechanism of plasma wave generation by dc current, Physical review letters 71 (15) (1993) 2465.

[107] A. Lutcov, V. Volga, B. Dymov, Thermal conductivity, electric resistivity and specific heat of dense graphites, Carbon 8 (6) (1970) 753–760.

[108] C. Kittel, et al., Introduction to solid state physics, Wiley New York, 1986.

[109] E. Hammond, K. Mahesh, P. Moin, A numerical method to simulate radio-frequency plasma discharges, Journal of Computational Physics 176 (2) (2002) 402–429.

[110] F. P. Heiman, G. Warfield, Space-charge capacitance of an intrinsic semiconductor film, Journal of Applied Physics 36 (10) (1965) 3206–3211.

[111] L. Burton, A. Madjid, Coulomb screening in intrinsic medium-gap semiconductors and the electrical conductivity of silicon at elevated temperatures, Physical Review 185 (3) (1969) 1127.

[112] T. Fang, A. Konar, H. Xing, D. Jena, Carrier statistics and quantum capacitance of graphene sheets and ribbons, Applied Physics Letters 91 (9) (2007) 092109.

[113] V. E. Dorgan, M.-H. Bae, E. Pop, Mobility and saturation velocity in graphene on sio 2, Applied Physics Letters 97 (8) (2010) 082112.

[114] A. Muñoz-Hernández, G. Diaz, Modeling of thermal runaway of carbonaceous materials: Graphite, biochar, and wood, AIP Advances 8 (9) (2018) 095312.

[115] C. Dupont, R. Chiriac, G. Gauthier, F. Toche, Heat capacity measurements of various biomass types and pyrolysis residues, Fuel 115 (2014) 644–651.

[116] K. Ragland, D. Aerts, A. Baker, Properties of wood for combustion analysis, Bioresource technology 37 (2) (1991) 161–168.

[117] H. Sugimoto, M. Norimoto, Dielectric relaxation due to interfacial polarization for heat-treated wood, Carbon 42 (1) (2004) 211–218.

[118] A. Muñoz Hernández, S. Dehghan, G. Diaz, Physical (steam) activation of post-gasification biochar derived from peach pits, in: ASME 2018 International Mechanical Engineering Congress and Exposition, American Society of Mechanical Engineers, 2018.

[119] A. B. García, A. Martínez-Alonso, C. A. L. y Leon, J. M. Tascón, Modification of the surface properties of an activated carbon by oxygen plasma treatment, Fuel 77 (6) (1998) 613–624.

[120] D. Lee, S. H. Hong, K.-H. Paek, W.-T. Ju, Adsorbability enhancement of activated carbon by dielectric barrier discharge plasma treatment, Surface and Coatings Technology 200 (7) (2005) 2277–2282.

[121] G.-Z. Qu, J. Li, Y. Wu, G.-F. Li, D. Li, Regeneration of acid orange 7-exhausted granular activated carbon with dielectric barrier discharge plasma, Chemical Engineering Journal 146 (2) (2009) 168–173.

[122] K. Yang, J. Peng, C. Srinivasakannan, L. Zhang, H. Xia, X. Duan, Preparation of high surface area activated carbon from coconut shells using microwave heating, Bioresource technology 101 (15) (2010) 6163–6169.

[123] B. Zhang, X. Zeng, P. Xu, J. Chen, Y. Xu, G. Luo, M. Xu, H. Yao, Using the novel method of nonthermal plasma to add cl active sites on activated carbon for removal of mercury from flue gas, Environmental science & technology 50 (21) (2016) 11837–11843.

[124] R. Arriagada, R. Garcia, M. Molina-Sabio, F. Rodriguez-Reinoso, Effect of steam activation on the porosity and chemical nature of activated carbons from eucalyptus globulus and peach stones, Microporous Materials 8 (3) (1997) 123–130.

[125] R. Azargohar, A. Dalai, Production of activated carbon from luscar char: experimental and modeling studies, Microporous and mesoporous materials 85 (3) (2005) 219–225.

[126] A. Aworn, P. Thiravetyan, W. Nakbanpote, Preparation and characteristics of agricultural waste activated carbon by physical activation having micro-and mesopores, Journal of Analytical and Applied Pyrolysis 82 (2) (2008) 279–285.

[127] W. Li, K. Yang, J. Peng, L. Zhang, S. Guo, H. Xia, Effects of carbonization temperatures on characteristics of porosity in coconut shell chars and activated carbons derived from carbonized coconut shell chars, Industrial Crops and Products 28 (2) (2008) 190–198.

[128] K. S. Novoselov, A. K. Geim, S. V. Morozov, D. Jiang, Y. Zhang, S. V. Dubonos, I. V. Grigorieva, A. A. Firsov, Electric field effect in atomically thin carbon films, science 306 (5696) (2004) 666–669.

[129] I. Meric, M. Y. Han, A. F. Young, B. Ozyilmaz, P. Kim, K. L. Shepard, Current saturation in zero-bandgap, top-gated graphene field-effect transistors, Nature nanotechnology 3 (11) (2008) 654.

[130] V. K. Arora, M. L. Tan, C. Gupta, High-field transport in a graphene nanolayer, Journal of Applied Physics 112 (11) (2012) 114330.

[131] A. C. Neto, F. Guinea, N. M. Peres, K. S. Novoselov, A. K. Geim, The electronic properties of graphene, Reviews of modern physics 81 (1) (2009) 109.

114

Appendix A

SIMPLIFICATION OF THE HYDRODYNAMIC MODEL

A.1 Introduction

In this chapter, the hydrodynamic model from Sec. 2.3 will be simplified to the form that is used in Chapter 4 and to the drift-diffusion model that is used in Chapter 3. The simplifications are achieved based on certain assumptions or criteria driven by the underlying physics of the problem.

A.2 Transient One-Dimensional Hydrodynamic Model

Semiconductor devices such as transistors are based in the manipulation of charge carrier (electron/hole) transport. Such semiconductor devices usually consist of a single charge carrier, typically electrons. As a consequence, the majority of the applications of hydrodynamic models are dedicated to analyze the flow of electrons [49, 52, 55, 57, 74]. Nonetheless, the flow of holes is also important in silicon and other semiconductor devices [47, 50, 56, 58, 60, 77, 78]. In modern times, in addition to conventional semiconductor devices, upon its discovery [128], graphene has caught the attention of many researchers because of its potential applications in electronic devices [40, 41, 113, 129–131]. In graphene devices, the flow of holes may be as important as the flow of electrons. Given our interest in applying the hydrodynamic model to graphite (stacked layers of graphene), and possibly extend it to bilayer and multilayer graphene, it is in our interest to have a general enough hydrodynamic model so that the flow of both electrons and holes is considered.

The one-dimensional (x-direction) transport of electrons and holes through a rod is driven by a voltage difference and diffusion processes between the two contacts at $x = 0, L$. The hydrodynamic equations for electron and hole flow include Gauss's law in Eq. (A.1a), charge conservation equations for electrons and holes in Eqs. (A.1b) and (A.1c), and momentum conservation equations for electrons and holes in Eqs. (A.1d) and (A.1e). The changes of kinetic energy of electrons and holes

due to their interactions with the lattice and the lattice thermal energy are described in Eqs. (A.1f), (A.1g), and (A.1h), repectively. The system of equations is

$$\frac{\partial^2 V}{\partial x^2} = -\frac{e}{\epsilon_r \epsilon_0}\left(n_h - n_e\right), \tag{A.1a}$$

$$\frac{\partial n_e}{\partial t} + \frac{\partial(u_e n_e)}{\partial x} = G_{e,net}, \tag{A.1b}$$

$$\frac{\partial n_h}{\partial t} + \frac{\partial(u_h n_h)}{\partial x} = G_{h,net}, \tag{A.1c}$$

$$\frac{\partial u_e}{\partial t} + u_e\frac{\partial u_e}{\partial x} = \frac{e}{m_e^\star}\frac{\partial V}{\partial x} - \frac{k_B}{m_e^\star n_e}\frac{\partial(n_e T_e)}{\partial x} - \frac{u_e}{\tau_{M,e}}, \tag{A.1d}$$

$$\frac{\partial u_h}{\partial t} + u_h\frac{\partial u_h}{\partial x} = -\frac{e}{m_h^\star}\frac{\partial V}{\partial x} - \frac{k_B}{m_h^\star n_h}\frac{\partial(n_h T_h)}{\partial x} - \frac{u_h}{\tau_{M,h}}, \tag{A.1e}$$

$$\frac{\partial T_e}{\partial t} + u_e\frac{\partial T_e}{\partial x} = -\frac{2}{3}T_e\frac{\partial u_e}{\partial x} + \frac{2}{3 n_e k_B}\frac{\partial}{\partial x}\left(k_e\frac{\partial T_e}{\partial x}\right) - \frac{T_e - T_L}{\tau_{E,e}}$$
$$+ \frac{2 m_e^\star u_e^2}{3 k_B \tau_{M,e}}\left(1 - \frac{\tau_{M,e}}{2\tau_{E,e}}\right), \tag{A.1f}$$

$$\frac{\partial T_h}{\partial t} + u_h\frac{\partial T_h}{\partial x} = -\frac{2}{3}T_h\frac{\partial u_h}{\partial x} + \frac{2}{3 n_h k_B}\frac{\partial}{\partial x}\left(k_h\frac{\partial T_h}{\partial x}\right) - \frac{T_h - T_L}{\tau_{E,h}}$$
$$+ \frac{2 m_h^\star u_h^2}{3 k_B \tau_{M,h}}\left(1 - \frac{\tau_{M,h}}{2\tau_{E,h}}\right), \tag{A.1g}$$

$$C_{L,v}\frac{\partial T_L}{\partial t} = \frac{\partial}{\partial x}\left(k_L\frac{\partial T_L}{\partial x}\right) + \frac{3 n_e k_B}{2}\left(\frac{T_e - T_L}{\tau_{E,e}}\right)$$
$$+ \frac{3 n_h k_B}{2}\left(\frac{T_h - T_L}{\tau_{E,h}}\right) + q_l^{*\prime\prime\prime}, \tag{A.1h}$$

where $V(x,t)$ is the electrostatic potential, t is the time, $n_e(x,t)$ is the electron density, $n_h(x,t)$ is the hole density, $u_e(x,t)$ is the electron velocity, $u_h(x,t)$ is the hole velocity, $T_e(x,t)$ is the electron temperature, $T_h(x,t)$ is the hole temperature, $T_L(x,t)$ is the lattice temperature, $q_l(x,t)$ represents the heat losses, $G_{e,net}(x,t) = G_e(x,t) - R_e(x,t)$ is the net generation rate of electrons which is equal to the generation rate $G_e(x,t)$ minus the recombination rate $R_e(x,t)$, and $G_{h,net}(x,t) = G_h(x,t) - R_h(x,t)$ is the net generation rates of holes, which is equal to the generation rate $G_h(x,t)$ minus the recombination rate $R_h(x,t)$.

The physical parameters are the elementary charge, e, the relative permittivity of the material, ϵ_r, the permittivity of free space, ϵ_0, the effective electron mass, $m_e^\star$, the effective hole mass, $m_h^\star$, Boltzmann's constant, k_B, the momentum relaxation time for electrons, $\tau_{M,e}$, the momentum relaxation time for holes, $\tau_{M,h}$, the energy relaxation time for electrons, $\tau_{E,e}$, the energy relaxation time for holes, $\tau_{E,h}$, the thermal conductivity of electrons, k_e, the thermal conductivity of holes, k_h, the thermal conductivity of the lattice, k_L, and the volumetric heat capacity of the lattice $C_{L,v}$.

A.3 Charge Carriers In Thermal Equilibrium With Constant, Uniform Temperature

Consider the case where electrons and holes are in thermal equilibrium, i.e., $T_e = T_h = T_c$, and their temperature is uniform in space and constant in time. Thermal equilibrium is relevant for devices where the densities of electrons and holes are similar in magnitude and when their mobilities are also similar in magnitude. The former criterion is true for intrinsic materials, for materials whose donor and acceptor doping levels are similar (not very common), and for transistor devices where the gate voltage would give rise to similar levels of 'instantaneous doping,' such as in graphene devices [40–42]. Meeting both criteria would mean that both of the carriers' speeds/kinetic energies are approximately the same. This is the case of intrinsic graphite, for which the ratio of the electron to the hole mobility is close to one [80] and for graphene transistors [40–42]. While thermal equilibrium is more physically feasible, keeping a constant and uniform carrier temperature may be a more crude approximation. It would mean that the external forces (e.g., electric field) are not large enough to change the carrier energy significantly in space or time.

Discarding the terms which involve a space or time derivative, and substituting the remaining terms from Eqs. (A.1f) and (A.1g) into the lattice energy equation, Eq. (A.1h), it becomes

$$
C_{L,v}\frac{\partial T_L}{\partial t} = \frac{\partial}{\partial x}\left(k_L\frac{\partial T_L}{\partial x}\right) - n_e k_B T_c \frac{\partial u_e}{\partial x} + \frac{n_e m_e^\star u_e^{2}}{\tau_{M,e}}\left(1 - \frac{\tau_{M,e}}{2\tau_{E,e}}\right)
$$
$$
- n_h k_B T_c \frac{\partial u_h}{\partial x} + \frac{n_h m_h^\star u_h^{2}}{\tau_{M,h}}\left(1 - \frac{\tau_{M,h}}{2\tau_{E,h}}\right) + q_l^{*\prime\prime\prime}. \quad \text{(A.2)}
$$

A.4 Nondimensional Equations

Nondimensionalization of equations is a well-known technique for simplifying complex equations. Upon its discovery and development, this technique has been utilized historically and has proven fruitful in the development of science. This technique will be exploited here to significantly reduce the complexity of the hydrodynamic model.

Equations (A.1) along with Eq. (A.2) are nondimensionalized using the following parameter definitions: $x^* = x/L$, $V^* = V/V_0$, $n_e^* = n_e/N_0$, $n_h^* = n_h/N_0$, $u_e^* = u_e/U$, $u_h^* = u_h/U$, $T_L^* = T_L/T_0$, $T_c^* = T_c/T_0$, and $t^* = tU/L$, with V_0 a reference voltage, N_0 a reference density, and T_0 a reference temperature. The following relationship will be used in this step. The mobility is related to the momentum relaxation time as follows: $\mu_e = e\tau_{M,e}/m_e^\star$; this is the simplest relationship between

these parameters. The nondimensional version of the equations becomes

$$\frac{\partial^2 V^*}{\partial x^{*2}} = -\zeta \left(n_h^* - n_e^* \right), \tag{A.3a}$$

$$\frac{\partial n_e^*}{\partial t^*} + \frac{\partial (u_e^* n_e^*)}{\partial x^*} = G_{e,net}^*, \tag{A.3b}$$

$$\frac{\partial n_h^*}{\partial t^*} + \frac{\partial (u_h^* n_h^*)}{\partial x^*} = G_{h,net}^*, \tag{A.3c}$$

$$\mathrm{Re}\frac{\tau_{M,e}}{\tau_{M,e,ref}} \left[\frac{\partial u_e^*}{\partial t^*} + u_e^* \frac{\partial u_e^*}{\partial x^*} \right] = \frac{\mu_e}{\mu_{e,ref}} \left[\frac{\partial V^*}{\partial x^*} - \beta \frac{1}{n_e^*} \frac{\partial n_e^*}{\partial x^*} \right] - u_e^*, \tag{A.3d}$$

$$\mathrm{Re}\frac{\tau_{M,e}}{\tau_{M,e,ref}} \left[\frac{\partial u_h^*}{\partial t^*} + u_h^* \frac{\partial u_h^*}{\partial x^*} \right] = -\frac{\mu_e}{\mu_{e,ref}} m_r \left[\frac{\partial V^*}{\partial x^*} + \beta \frac{1}{n_h^*} \frac{\partial n_h^*}{\partial x^*} \right] - \gamma u_h^*, \tag{A.3e}$$

$$\psi_0 \frac{C_{L,v}}{C_{L,v,ref}} \frac{\partial T_L^*}{\partial t^*} = \psi_1 \frac{\partial}{\partial x^*} \left(\frac{k_L}{k_{L,ref}} \frac{\partial T_L^*}{\partial x^*} \right) - \beta \left(n_e^* \frac{\partial u_e^*}{\partial x^*} + m_r n_h^* \frac{\partial u_h^*}{\partial x^*} \right)$$
$$+ \left(1 - \frac{1}{2}\nu \right) \left[\frac{\tau_{M,e,ref}}{\tau_{M,e}} n_e^* u_e^{*2} + \frac{\tau_{M,e,ref}}{\tau_{M,h}} n_h^* u_h^{*2} \right] + q_l^{*\prime\prime\prime}, \tag{A.3f}$$

where $\zeta = eL^2 N_0/\epsilon_r \epsilon_0 V_0$, $\beta = k_B T_c/eV_0$, $\gamma = \tau_{M,e}/\tau_{M,h}$, $m_r = m_e^\star/m_h^\star$, $\nu = \tau_{M,e}/\tau_{E,e} = \tau_{M,h}/\tau_{E,h}$, $\psi_0 = \tau_{M,e,ref}C_{L,v,ref}T_0/m_e^\star N_0 UL$, $\psi_1 = \tau_{M,e,ref}k_{L,ref}T_0/m_e^\star N_0 U^2 L^2$, $G_{e,net}^* = G_{e,net}L/N_0 U$, $G_{h,net}^* = G_{h,net}L/N_0 U$, $q_l^{*\prime\prime\prime} = q_l^{\prime\prime\prime}\tau_{M,e}/N_0 m_e^\star U^2$, and $U = eV_0\tau_{M,e,ref}/m_e^\star L = \mu_{e,ref}V_0/L$ is the maximum average electron velocity. $\mathrm{Re} = U\tau_{M,e,ref}/L$, which is the Reynolds number for the electron cloud [50,57,59,106]. The Reynolds number here is analogous to that used in fluid dynamics; a small value means that the inertia forces in the momentum equations can be neglected [50, 57, 59, 106]. Note that in the definition of ν it was assumed that the ratio of momentum relaxation time to energy relaxation time was equal for both electrons and holes. More details about this assumption in Sec. A.7.

A.5   Simplified Nondimensional Equations

Electrons and holes are expected to have significant scattering events when they are traveling through the rod; as a consequence the Reynolds number becomes very small. Based on our nondimensionalized equations, the Reynolds number multiplies the transient and inertia forces in the momentum equations for electrons (A.3d) and holes (A.3e), which means that these terms can be safely discarded [50, 57, 59]. Because the hydrodynamic model is composed of highly-coupled nonlinear partial differential equations, such simplifications prove crucial in reducing its complexity.

Discarding the transient and inertia terms, the system of nondimensional equations (A.3) becomes

$$\frac{\partial^2 V^*}{\partial x^{*2}} = -\zeta \left(n_h^* - n_e^* \right), \tag{A.4a}$$

$$\frac{\partial n_e^*}{\partial t^*} + \frac{\partial (u_e^* n_e^*)}{\partial x^*} = G_{e,net}^*, \tag{A.4b}$$

$$\frac{\partial n_h^*}{\partial t^*} + \frac{\partial (u_h^* n_h^*)}{\partial x^*} = G_{h,net}^*, \tag{A.4c}$$

$$u_e^* = \frac{\mu_e}{\mu_{e,ref}} \left[\frac{\partial V^*}{\partial x^*} - \beta \frac{1}{n_e^*} \frac{\partial n_e^*}{\partial x^*} \right], \tag{A.4d}$$

$$u_h^* = -\frac{\mu_h}{\mu_{e,ref}} \left[\frac{\partial V^*}{\partial x^*} + \beta \frac{1}{n_h^*} \frac{\partial n_h^*}{\partial x^*} \right], \tag{A.4e}$$

$$\psi_0 \frac{C_{L,v}}{C_{L,v,ref}} \frac{\partial T_L^*}{\partial t^*} = \psi_1 \frac{\partial}{\partial x^*} \left(\frac{k_L}{k_{L,ref}} \frac{\partial T_L^*}{\partial x^*} \right) - \beta \left(n_e^* \frac{\partial u_e^*}{\partial x^*} + m_r n_h^* \frac{\partial u_h^*}{\partial x^*} \right)$$
$$+ \left(1 - \frac{1}{2}\nu \right) \left[\frac{\tau_{M,e,ref}}{\tau_{M,e}} n_e^* u_e^{*2} + \frac{\tau_{M,e,ref}}{\tau_{M,h}} n_h^* u_h^{*2} \right] + q_l^{*\prime\prime\prime}. \tag{A.4f}$$

This version of the hydrodynamic model is taken as the starting model in Chapter 4.

A.6   Steady-State Equations

In this step the transient terms are discarded to obtain the steady-state equations as follows:

$$\frac{\partial^2 V^*}{\partial x^{*2}} = -\zeta \left(n_h^* - n_e^* \right), \tag{A.5a}$$

$$\frac{\partial (u_e^* n_e^*)}{\partial x^*} = G_{e,net}^*, \tag{A.5b}$$

$$\frac{\partial (u_h^* n_h^*)}{\partial x^*} = G_{h,net}^*, \tag{A.5c}$$

$$u_e^* = \frac{\mu_e}{\mu_{e,ref}} \left[\frac{\partial V^*}{\partial x^*} - \beta \frac{1}{n_e^*} \frac{\partial n_e^*}{\partial x^*} \right], \tag{A.5d}$$

$$u_h^* = -\frac{\mu_h}{\mu_{e,ref}} \left[\frac{\partial V^*}{\partial x^*} + \beta \frac{1}{n_h^*} \frac{\partial n_h^*}{\partial x^*} \right], \tag{A.5e}$$

$$0 = \psi_1 \frac{\partial}{\partial x^*} \left(\frac{k_L}{k_{L,ref}} \frac{\partial T_L^*}{\partial x^*} \right) - \beta \left(n_e^* \frac{\partial u_e^*}{\partial x^*} + m_r n_h^* \frac{\partial u_h^*}{\partial x^*} \right)$$
$$+ \left(1 - \frac{1}{2}\nu \right) \left[\frac{\tau_{M,e,ref}}{\tau_{M,e}} n_e^* u_e^{*2} + \frac{\tau_{M,e,ref}}{\tau_{M,h}} n_h^* u_h^{*2} \right] + q_l^{*\prime\prime\prime}. \tag{A.5f}$$

A.7   Drift-Diffusion Model

In this step the nondimensional version of the drift-diffusion model utilized in Chapter 3 will be obtained. It is noted that in this particular instance the diffusion terms will be discarded based on certain criteria as explained below. Nonetheless,

the model will still be called drift-diffusion because it is similar to drift-diffusion models.

In this model, it is assumed that the carrier diffusion terms are small compared to the rest of the terms in Eqs. (A.5); the diffusion terms are those containing the coefficient β. This assumption is more appropriate for longer rods; as the length of the rod decreases, the importance (magnitude) of the diffusion terms needs to be assessed. Such an assessment will be shown in Chapter 4 under different operating conditions. Discarding the diffusion terms yields the following equations:

$$\frac{\partial^2 V^*}{\partial x^{*2}} = -\zeta \left(n_h^* - n_e^* \right), \tag{A.6a}$$

$$\frac{\partial (u_e^* n_e^*)}{\partial x^*} = G_{e,net}^*, \tag{A.6b}$$

$$\frac{\partial (u_h^* n_h^*)}{\partial x^*} = G_{h,net}^*, \tag{A.6c}$$

$$u_e^* = \frac{\mu_e}{\mu_{e,ref}} \frac{\partial V^*}{\partial x^*}, \tag{A.6d}$$

$$u_h^* = -\frac{\mu_h}{\mu_{e,ref}} \frac{\partial V^*}{\partial x^*}, \tag{A.6e}$$

$$0 = \psi_1 \frac{\partial}{\partial x^*} \left(\frac{k_L}{k_{L,ref}} \frac{\partial T_L^*}{\partial x^*} \right) + \left(1 - \frac{1}{2}\nu \right) \left[\frac{\tau_{M,e,ref}}{\tau_{M,e}} n_e^* u_e^{*2} + \frac{\tau_{M,e,ref}}{\tau_{M,h}} n_h^* u_h^{*2} \right]$$
$$+ q_l^{*'''}. \tag{A.6f}$$

The momentum and energy relaxation times depend on the energy of the carriers and the lattice [46, 47, 55, 58, 59, 61]. In our definition of ν it has been assumed that $\nu = \nu_e = \nu_h$ to simplify the energy equation (A.6f). This definition is less restrictive than it appears to be. The only restriction is that each ν, or ratio of relaxation times, be equal. Yet, note that (1) the momentum relaxation times for electrons and holes may have different values, and (2) they may even have different energy dependencies.

It is known that the ratio of the electron to hole mobility in graphite is about 1.1 for low and near room temperatures [80], while in studies of graphene devices, the same value for both the electron and hole mobility has been used [40, 104, 129]. The momentum relaxation time can be readily calculated from the mobility using the relationship given in Sec. A.4. Though, values for the energy relaxation times have not been found in the literature. As a consequence, the effect of the energy relaxation time will be analyzed by changing the magnitude of ν.

Let us have a short discussion about the implications of the relaxation times. The relaxation time is defined as the amount of time it takes a system to return to its equilibrium mode after it has been perturbed. The relaxation time is also the inverse of the frequency of collisions. In general, the momentum relaxation time is smaller than the energy relaxation time because if a carrier collision occurs a change in momentum (magnitude or direction) is more likely to occur than a change in

energy (magnitude only). Upon collision of a charge carrier with the lattice, the extent of energy transferred is determined by the energy relaxation time. A larger energy relaxation time means a lower amount of energy is exchanged between the charge carrier and the lattice. This can be easily seen through the third term on the right-hand-side of Eqs. (A.1f) and (A.1g). However, as the energy relaxation time τ_E increases, the coefficient $(1 - \tau_M/\tau_E)$ of the fourth term in Eqs. (A.1f) and (A.1g) increases, and this term is really important because it represents Joule (self) heating [55]. This coefficient is carried on from Sec. A.6 through Sec. A.6 and is now represented by $(1 - \nu/2)$ in Eq. (A.6f), where ν acts as a modulator of the Joule heating power. This coefficient ranges from a minimum of 0.5 (50%) Joule heating power when $\nu = 1$ to approximately (100%) Joule heating power when $(\nu \ll 1)$. For instance, if $\tau_E = 50\tau_M$, $\nu = 0.02$, and the coefficient $(1 - \nu/2) = 0.99$.

If we let the energy relaxation time τ_E be much greater than the momentum relaxation time τ_M, i.e., $(\nu \lesssim 0.02)$, the coefficient multiplying the bracketed term on Eq. (A.6f) becomes nearly equal to one. In addition, by substituting the velocity for both electrons and holes, Eqs. (A.6d) and (A.6e), once into the energy equation (A.6f), it can now be re-written as follows:

$$0 = \psi_1 \frac{\partial}{\partial x^*} \left(\frac{k_L}{k_{L,ref}} \frac{\partial T_L^*}{\partial x^*} \right) + (n_e^* u_e^* - m_r n_h^* u_h^*) \frac{\partial V^*}{\partial x^*} + q_l^{*'''}. \tag{A.7}$$

Appendix B

REPLICATION OF PUBLISHED RESULTS

B.1 Introduction

In this chapter, a set of results that was obtained by applying our numerical scheme to the hydrodynamic model by Osses-Márquez and Calderón-Muñoz [59] will be compared to their original results. The first objective for doing this comparison is to show a hydrodynamic model, its application, and a set of solutions that can be obtained with it. The second objective is to show that our numerical scheme, different from the one used in Ref. [59], is able to replicate the original set of results. Since we will apply this numerical scheme to our hydrodynamic model, which is similar to the one in Ref. [59], this step is crucial to make sure our numerical algorithm is well-defined and that our code is free of syntax errors. This is especially important because hydrodynamic models form a set of highly-coupled non-linear partial differential equations whose numerical schemes are very unstable. In addition, we are applying this hydrodynamic model to graphite – something that has not been done in the literature – under very different operating conditions and with very different properties than those of semiconductors. Thus, it is ideal to have an error-free code before further development of the numerical scheme.

B.2 Replication Of Results

Osses-Márquez and Calderón-Muñoz published a paper where they have studied the "Thermal influence on charge carrier transport in solar cells based on GaAs PN junctions" [59]. In their paper, the model equations have been simplified, nondimensionalized, and only the steady-state version of the equations has been solved using perturbation methods. Because the hydrodynamic model used in Chapter 4 is similar to the hydrodynamic model from Ref. [59], this model and its results were used to aid us in the development of the numerical solvers used in our simulations applied to graphite.

Since we are interested in using our version of the hydrodynamic model to analyze the transient behavior of our problem, their hydrodynamic model [59] was
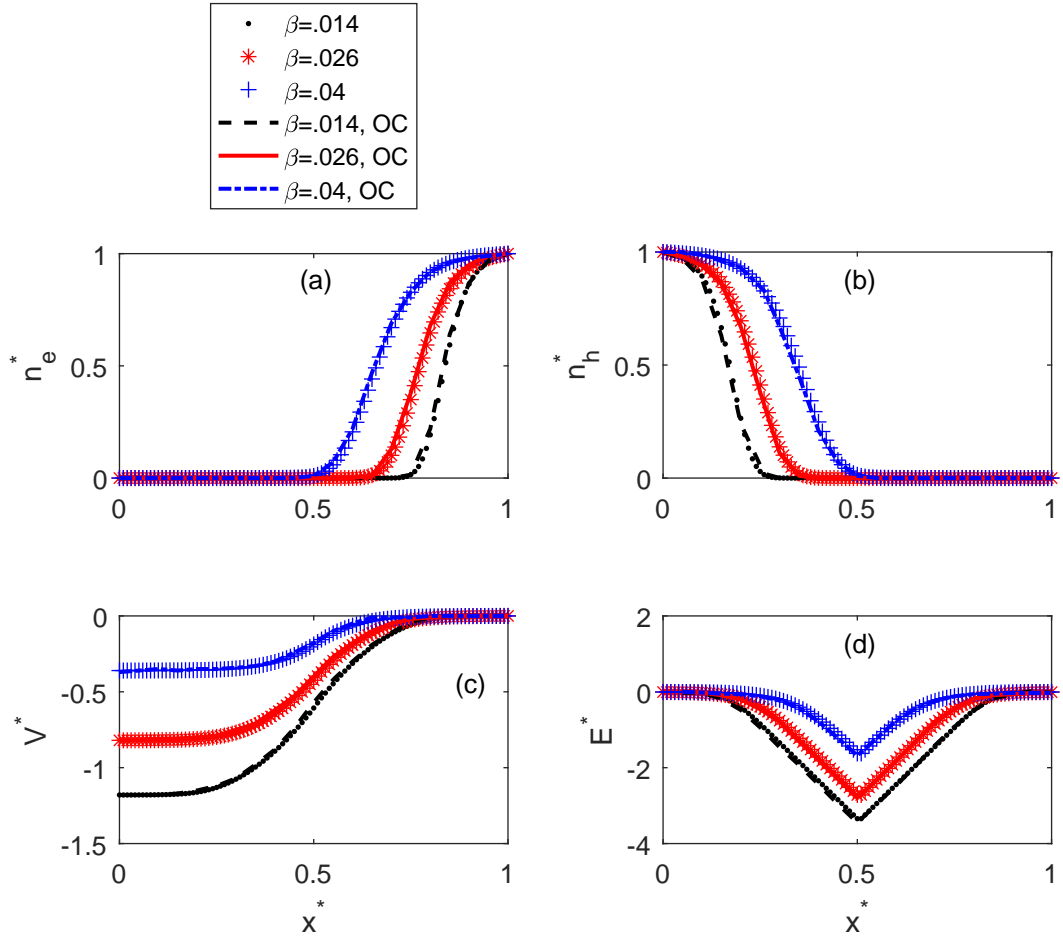
Figure B.1: Replication of Fig. 2 from Ref. [59]. The symbols represent the results obtained with our code. The lines represent the results from Ref. [59], where 'OC' on the legend stands for each of the author's last name.

solved including the transient terms. The transient hydrodynamic model was discretized using second order finite differences and integrated using an explicit fourth order Runge-Kutta method.

The results from Fig. 2 from Ref. [59] were reproduced using our transient model, and the comparison is made in Fig. B.1. All variables are nondimensional. The symbols represent the results obtained with our numerical scheme, while the lines represent the results from the cited reference. It can be seen that the results agree very well. The operating conditions are the following: $L = 840 \ \mu$m and $V_{app} = 0$ V; though, there is a built-in voltage due to the PN junction, thus, $V^*(x^* = 0) = V_{app} - V_{bi}$. The algorithm used 101 grid points and a time step $\Delta t = 8.82 \times 10^{-12}$ seconds. The solution is shown at a time equal to $t = 8.82 \times 10^{-7}$ seconds.